UNIVERSITY OF CALIFORNIA SAN DIEGO

Large-scale identification and functional analysis of the m^{6}A reader YTHDF2 as a therapeutic target for triple negative breast cancer

A dissertation submitted in partial satisfaction of the
requirements for the degree
Doctor of Philosophy

in

Bioengineering

by

Jaclyn Michelle Einstein

Committee in charge:

Professor Gene Yeo, Chair
Professor Shankar Subramaniam, Co-Chair
Professor Stephanie Fraley
Professor Olivier Harismendy
Professor Jean Wang

2020

The dissertation of Jaclyn Michelle Einstein is approved, and it is acceptable in quality and form for publication on microfilm and electronically:

_____

_____

_____

_____
Co-Chair

_____
Chair

University of California San Diego

2020

DEDICATION

Dedicated to the memory of my aunt, Iris Duze.

Thank you for supporting me through every milestone it took to get here.

TABLE OF CONTENTS

LIST OF FIGURES

LIST OF TABLES

ACKNOWLEDGEMENTS

This dissertation is the culmination of my efforts to become a well-rounded bioengineer, specificially by combining RNA biology and informatics to develop new approaches for identifying promising drug targets for cancer therapy. I am extremely grateful for the mentorship and training from my thesis advisor, Gene Yeo, who has provided me with limitless opportunities, helped me expand my network, supported my sometimes outlandish ideas, allowed me to make mistakes and continues to instill confidence in me. I would not be where I am today without his guidance. I would also like to thank all of the members of the Yeo Lab, past and present, who have significantly contributed to my training. In particular, I would like to thank Eric Van Nostrand, who took me in as a rotation student and allowed me to drive this project to completion, Mark Perelis, who is always willing to engage in my scientific thought process, has helped me develop my ideas and has taught me how to effectively communicate my science, and Julia Nussbacher, who fostered my interest in m^6A biology and paved the way for me in the lab as a strong woman in science. Thank you to everyone who has contributed to my learning of programming and analysis of high-throughput sequencing data and who taught me new molecular biology skills along the way. I am also tremendously grateful for my collaboration with Trey Westbrook at Baylor College of Medicine. Completion of this story would not have been possible without his mentorship and guidance from his team.

Completion of my dissertation would not have been possible without the unwavering love and support from my family. Thank you Mom and Dad for sending me to college and for always supporting my ambitions, even when they took me 2,500 miles away. Thank you for allowing me to develop into my own person while always leaving the light on at home. There aren't words to describe how undoubtedly your love and support has impacted me on this journey. Thank

you to my sister, Becca for always being the first to celebrate my successes and for being my constant shoulder to lean on and open ear. Lastly, thank you Glenn, for being the most loyal partner, for believing in me always, for empowering me to shoot for the stars in my career and for bringing me flowers and chocolate to console every paper rejection I received. Thank you, truly, to everyone who has been a part of this journey.

Chapter 2, in part, is a reprint of material as it appears in: Wheeler EC.*, Vu AQ*, **Einstein JM**, DiSalvo M, Ahmed N, Van Nostrand EL, Shishkin AA, Jin W, Allbritton NA, Yeo GW. Pooled CRISPR screens with imaging on microraft arrays reveals stress granule regulatory factors. Nat Methods, doi:10.1038/s41592-020-0826-8 (2020). The dissertation author was the second author of this paper.

Chapters 2, 3 and 4, in full, are a reprint of material as it will appear in: **Einstein JM**, Perelis M, Chaim IA, Meena JK, Nussbacher JK, Tankka AT, Yee BA, Li H, Madrigal AA, Neill NJ, Shankar A, Tyagi S, Westbrook TF, Yeo GW. Inhibition of YTHDF2 triggers proteotoxic cell death in MYC-dependent cancer. *In preparation*. The dissertation author is the primary author of this paper.

VITA

2014	Bachelor of Science in Biological Systems Engineering, Virginia Polytechnic Institute and State University
2020	Doctor of Philosophy in Bioengineering, University of California San Diego

PUBLICATIONS

Einstein JM, Yeo, GW. Making the cut in the dark genome. Science, doi: 10.1126/science.aak9849 (2016)

Lorenz DA, Sathe S, **Einstein JM**, Yeo GW. Direct RNA sequencing enables m6A detection in enodogenous transcript isoforms at base specific resolution. RNA, doi:10.1261/rna.072785.119 (2019)

Wheeler EC*, Vu AQ*, **Einstein JM**, DiSalvo M, Ahmed N, Van Nostrand EL, Shishkin AA, Jin W, Allbritton NA, Yeo GW. Pooled CRISPR screens with imaging on microraft arrays reveals stress granule regulatory factors. Nat Methods, doi:10.1038/s41592-020-0826-8 (2020)

Davis A, **Einstein JM**, Wang R, Zheng D, Jayne N, Tian B, Yeo GW, Zhang D. A CRISPR RNA-binding protein screen reveals novel regulators of RUNX1 isoform generation. *In preparation.*

Einstein JM, Perelis M, Chaim IA, Meena JK, Nussbacher JK, Tankka AT, Yee BA, Li H, Madrigal AA, Neill NJ, Shankar A, Tyagi S, Westbrook TF, Yeo GW. Inhibition of YTHDF2 triggers proteotoxic cell death in MYC-dependent cancer. *In preparation*.

ABSTRACT OF THE DISSERTATION

Large-scale identification and functional analysis of the m^{6}A reader YTHDF2 as a therapeutic target for triple negative breast cancer

by

Jaclyn Michelle Einstein

Doctor of Philosophy in Bioengineering

University of California San Diego, 2020

Professor Gene Yeo, Chair
Professor Shankar Subramaniam, Co-Chair

RNA-binding proteins (RBPs) are critical regulators of post-transcriptional gene expression and aberrant RBP-RNA interactions can cause cancer. However, RBPs are often overlooked as therapeutically relevant targets because unlike transcription factors, altered RBP activity is more frequently caused by changes in the expression levels of RBPs and their underlying targets, as opposed to somatic mutations. It has therefore been challenging to systematically evaluate the function of RBPs in disease. We addressed the lack of characterization of RBPs in cancer by developing an approach to interrogate the function of RBPs using pooled CRISPR-

Cas9 screening. We identified 57 putative RBPs with distinct roles in supporting MYC-driven oncogenic pathways and we found that disrupting YTHDF2-dependent degradation of its target transcripts triggers apoptosis of MYC-dependent cancer cells and tumors. Next, we profiled YTHDF2 function using enhanced CLIP (eCLIP) and m^6A-seq analysis, which revealed extensive interactions with mRNAs encoding MAPK pathway genes. We found that mRNA stabilization of upstream MAPK pathway genes drives epithelial-to-mesenchymal transition in MYC-dependent cells and is accompanied by profound oxidative cellular stress due to increased protein synthesis. We next explored the cellular stress response elicited by YTHDF2 depletion by surveying the activation of the intrinsic and extrinsic apoptotic pathways. Loss of YTHDF2 caused activation of the unfolded protein response and subsequent mitochondrial dysfunction in MYC-dependent cells, which are especially sensitive to increases in oxidative stress. Finally, we determined that *PRSS23* mRNA stabilization is necessary for driving apoptosis by promoting TCF12-mediated transcription of cancer lineage-specific transcripts and translation factors. Thus, this dissertation highlights the therapeutic relevance of RBPs by uncovering the critical role of YTHDF2 in counteracting the global increase of mRNA synthesis in MYC-driven cancers.

Chapter 1

Introduction

1.1 MYC amplification in TNBC

Breast cancer is the second most deadly type of cancer in women and nearly two million women worldwide are diagnosed with breast cancer each year (The Breast Cancer Research Foundation, www.bcrf.org). Dating back to the 1970s, the antiestrogen tamoxifen was the first and most widely used therapy for women with metastatic breast cancer (M. P. Cole et al., 1971). However, it was later identified that such hormonal therapies only benefitted patients expressing hormone receptors. Currently, four breast cancer subtypes have been identified and are distinguished between estrogen receptor (ER)-positive breast cancers (i.e. luminal A and luminal B) and ER-negative breast cancers (i.e. basal-like and human epidermal growth factor receptor 2 (HER2)) (Dent et al., 2007). The majority of basal-like tumors lack hormone receptors, termed triple negative breast cancer (TNBC), and as a result lack biomarkers for targeted therapies which leads to shorter patient survival rates and high mortality rates (Rakha et al., 2008). In addition, patients with TNBC are more likely to develop locoregional and distant metastases

with propensity for visceral over bone and liver metastases compared with other breast cancer subtypes (Rakha et al., 2008). For these reasons, TNBC has the worst prognosis of all breast cancer subtypes and identification of novel targeted therapies are of increasing interest to treat TNBC since chemotherapy is often the only available treatment option.

In an effort to identify biomarkers for the development of new targeted therapeutic strategies, researchers have attempted to better define the biology underlying TNBC. 92% of triple-negative tumors had a high or intermediate *MYC* gene signature in the I-SPY TRIAL which correlated with poor prognosis and MYC signaling was elevated in patients with poor response to neoadjuvant therapy (Horiuchi et al., 2012). Therefore, not only does MYC serve as a prognostic biomarker for the treatment of TNBC, but also indcates that patients with high MYC expressing tumors may be at a higher risk for developing chemotherapy resistance.

1.2 MYC: a prominent oncogene and difficult drug target

C-MYC (MYC) was among the earliest described human oncogenes identified, and is now recognized as the primary driver in oncogenic transformation and maintenance of cancer gene expression programs in a broad spectrum of cancer types where cells become “addicted” to and dependent on MYC for survival (Zuber et al., 2011). Although this unique property makes MYC an attractive drug target in cancers, strategies to directly inhibit this protein with small molecules have been hindered by the lack of any known enzymatic activity that can be modulated (Brown et al., 2011; Ou et al., 2007). Elevated levels of MYC in cancer are caused by a variety of mutagenic mechanisms, including amplification of the MYC locus, its translocation to genomic sites that place it in proximity to enhancers or by mutations that increase the stability of the MYC transcript or protein (Beroukhim et al., 2010; Dang, 2012; Tu et al., 2015). In

its canonical role as a transcription factor, MYC regulates numerous coding and non-coding genes controlling proliferation, metabolism, differentiation and apoptosis (**Figure 1.1**) (Nilsson & Cleveland, 2003). Unsurprisingly, its levels in non-cancerous cells are tightly regulated, as MYC over-abundance generally leads to a selective increase in the transcription of these target genes, precipitating profound dysregulation of gene expression programs (Vogelstein et al., 2013).

1.3 A role for MYC in the regulation of RNA processing

MYC regulates the transcription of several genes that control key steps in RNA processing, including RNA-binding proteins (RBPs). RBPs determine the fate of transcribed RNAs by regulating their splicing, turnover, polyadenylation, translation and subcellular localization (Hentze et al., 2018). To illustrate, BUD31 depletion lead to widespread and lethal splicing defects in MYC-induced human mammary epithelial cells expressing an inducible MYC-estrogen receptor fusion transgene (MYC-ER HMECs) (Hsu et al., 2015). BUD31 is upregulated during MYC amplification and is associated with several splicing factors and ribosomal proteins in humans (Masciadri et al., 2004), thus suggesting an increased demand for the spliceosome (and likely other pre-mRNA processing machinery) in MYC hyperactive cells (**Figure 1.2**).

Independently from its DNA-binding function, MYC regulates post-transcriptional gene expression via recruitment of transcription factor TFIIH kinase, phosphorylation of RNA pol II and methylation of the mRNA 5' cap (M. D. Cole & Cowling, 2008). MYC also enhances translation by increasing transcription of ribosomal RNAs (rRNAs), ribosomal proteins (RPs), and transfer RNAs (tRNAs) (Kress et al., 2015; van Riggelen et al., 2010). Conversely, *MYC* transcript stability is coordinately regulated by RBPs that can modulate its stability, including HuR (ELAVL1), AUF1, TIAR and tristetraprolin (TTP) (Lafon et al., 1998; Liao et al., 2007;

Marderosian et al., 2006). Thus, MYC regulates cellular function and survival in part by modulating RNA metabolism and is itself post-transcriptionally regulated by RBPs.

1.4 The role of m^{6}A RNA methylation in cancer

The *MYC* transcript contains N6-methyladenosine (m^{6}A) modifications throughout its coding and 5' and 3' untranslated regions (UTRs), which are greatly enriched in cancer (Vu et al., 2017). RBPs deposit ("writers": METTL3, METT14, WTAP), bind ("readers": YT521-B homology (YTH) domain proteins), and remove ("erasers": FTO and ALKBH5) m^{6}A modifications to regulate RNA stability, including that of the *MYC* mRNA (Huang et al., 2018; Su et al., 2018; Weng et al., 2018). m^{6}A modification of an RNA can be induced by several cellular stressors that accompany cancer cell transformation and growth, promoting the translation of a distinct subset of mRNA targets (Lin et al., 2016). As a result, cancer cells contain an $\sim$8-fold increase in m^{6}A-methyltransferase activity compared to non-transformed cells, which directly contributes to elevated expression of oncoproteins (Tuck et al., 1996). Furthermore, several RBPs that are known to interact with m^{6}A-modified RNA become upregulated in cancer and are required for the growth, survival and invasion of cancer cells (Deng et al., 2018; Lin et al., 2016).

1.5 m^{6}A effector proteins and identifying their mRNA targets

The existence of m^{6}A was first identified in the early 1970s and is now recognized as the most abundant internal mRNA modification in humans (Perry & Kelley, 1974). The dynamic nature of m^{6}A methylation wasn't revealed until decades later with the discovery that fat mass and obesity-associated protein (FTO) has the ability to demethylate m^{6}A-containing transcripts

(Jia et al., 2011). This discovery highlights the ability of cells to modulate levels of m^6A according to their physiological state, thus terming the dynamic "epitranscriptome". It was later found that m^6A is deposited on RNAs to specifically regulate mRNA splicing and stability. Cytoplasmic regulation of m^6A-containing mRNA is mediated by YTH-domain containing proteins (YTHDF1, YTHDF2, and YTHDF3), which bind m^6A modifications via the carboxy-terminal domain to promote either degradation of the mRNA by localizing the complex to cellular mRNA decay sites or stabilization of the mRNA by recruiting translation initiation factors (H. Shi et al., 2017; X. Wang et al., 2014; X. Wang et al., 2015) (**Figure 1.3**). Although the mechanistic basis for why an m^6A modified transcript might be bound by one YTH-domain containing protein over another remains unclear, recent studies have indicated that distinctive YTH-domain containing proteins are vital for neural development and female fertility, limit stem cell expansion and support cancer progression (M. Chen et al., 2018; Ivanova et al., 2017; Z. Li et al., 2018; Paris et al., 2019). Thus, there appears to be a role for m^6A in the balance of normal and malignant differentiation.

In an effort to clarify which transcripts are uniquely regulated by m^6A in different cell types, several different technologies have emerged for m^6A profiling. Second generation methods employ isolation of m^6A-modified transcripts by immunocapture followed by massively parallel sequencing, originally termed m^6A-seq (Dominissini et al., 2013). This method proved to be highly specific and identified a nonrandom distribution of m^6A sites clustered around stop codons and within long internal exons (Dominissini et al., 2013). Newer technologies have improved the resolution of detection for m^6A peaks by harnessing UV-crosslinking to create a mutational signature at the precise location of antibody binding, which is detected by reverse transcription (Linder et al., 2015). Additionally, the binding profiles of m^6A-binding proteins can be analyzed using Enhanced Crosslinking and Immunoprecipitation followed by sequenc-

ing (eCLIP-seq) by generating sequencing libraries from mRNAs that immunoprecipitate with an RBP-specific antibody (Van Nostrand et al., 2016). Analysis of mRNA enrichment compared to size-matched inputs (SMInput) reveal specific RBP-mRNA interactions. eCLIP is an improvement on previous methods such as iCLIP and PAR-CLIP by maintaining single nucleotide resolution while omitting RNA radiolabeling and autoradiographic visualization and reducing PCR biases (Van Nostrand et al., 2016). Overlap of m^6A profiling methods with eCLIP of m^6A-binding proteins has enabled robust, large-scale generation of epitranscriptome-wide binding maps for RBPs while illuminating specific RBP-m^6A-mRNA interactions that contribute to tumorigenesis. Thus, the emergence of these technologies has permitted the identification of new prognostic biomarkers for human cancers and has directed the development of unique strategies for therapeutic targeting of RBP-mRNA interactions.

1.6 RNA-binding proteins as therapeutic targets for cancer

Changes in cellular growth rate and identity that occur during cancer progression are driven by specific gene expression signatures programmed by the activity of DNA-binding transcription factors (TFs) and RBPs. To support oncogenic growth rates, cancer cells generally require increased levels of transcription and global pre-RNA synthesis supported by TFs, consequently increasing the cell's dependence on post-transcriptional regulation by RBPs. While TF mutations, which encompass approximately 20% of all oncogenes, have been studied for decades and their interactions are now fairly well understood, RBPs have been overlooked as drivers of disease and therapeutically relevant targets. Somatic mutations, epigenetic changes, and post translational modifications can cause aberrant RBP expression and activity, which in turn contribute to cancer progression by promoting cell proliferation, evasion of apoptosis and

host immune surveillance, and induction of angiogenesis and cancer cell invasion (Pereira et al., 2017). Furthermore, several RBPs are known to regulate the stability of mRNAs encoding oncogenes and tumor suppressors (Pereira et al., 2017). Recently, therapeutic targeting of RBPs has become attainable, aided by drug discovery efforts directed at identifying small molecules and designing antisense oligonucleotides to modulate RBPs in disease (Fang et al., 2019; Smith et al., 2006). However, in cancer, RBP regulatory mechanisms and their RNA targets remain largely unexplored mainly because the systematic evaluation of RBPs has been limited by a lack of sensitive and efficient assays for phenotypic interrogation of individual RBPs (Pereira et al., 2017).

1.7 Outline of the dissertation

Since strategies to directly inhibit MYC have been pharmacologically challenging, I pursued an alternative approach aimed at functionally identifying RBPs that are selectively required for sustaining MYC's oncogenic gene regulatory program through phenotypic interrogation. I begin this thesis by describing the pooled CRISPR-Cas9 screening platform I developed to systematically identify RBPs that are vital for MYC-dependent cancer cell survival. This approach revealed 57 promising candidate RBPs that are linked to distinct RNA metabolic pathways. Our initial analyses focus on YTH m^6A RNA Binding Protein 2 (*YTHDF2*) given its important role in m^6A regulation and recent implications in cancer. We validated that YTHDF2 depletion induced apoptosis in relevant human cancer cell lines and impeded growth of tumor xenografts *in vivo* (Chapter 2). Next, we performed integrated analysis of eCLIP-seq, m^6A-seq and RNA sequencing (RNA-seq) to identify the RNAs that are physically and endogenously bound by YTHDF2. After identifying several YTHDF2 targets belonging to the MAPK/ERK cascade, we

performed pathway analyses to understand how YTHDF2-mediated changes in growth factor signaling modulate observed increases in protein synthesis and subsequent apoptosis (Chapter 3). Finally, through probing of both intrinsic and extrinsic apoptotic pathways, we found that depletion of YTHDF2 activates uncontrollable translation, induces the endoplasmic reticulum (ER)-overload response and causes selective cell death in MYC-dependent breast cancer cells. The convergence of these studies describes a new YTHDF2 binding interaction with the mRNA that encodes Serine Protease 23 (*PRSS23*), a gene that activates the TCF12 transcription factor, inducing transcription of cancer lineage-specific genes that contribute to epithelial-to-mesenchymal transition (EMT), translation initiation and ultimately, apoptosis (Chapter 4).

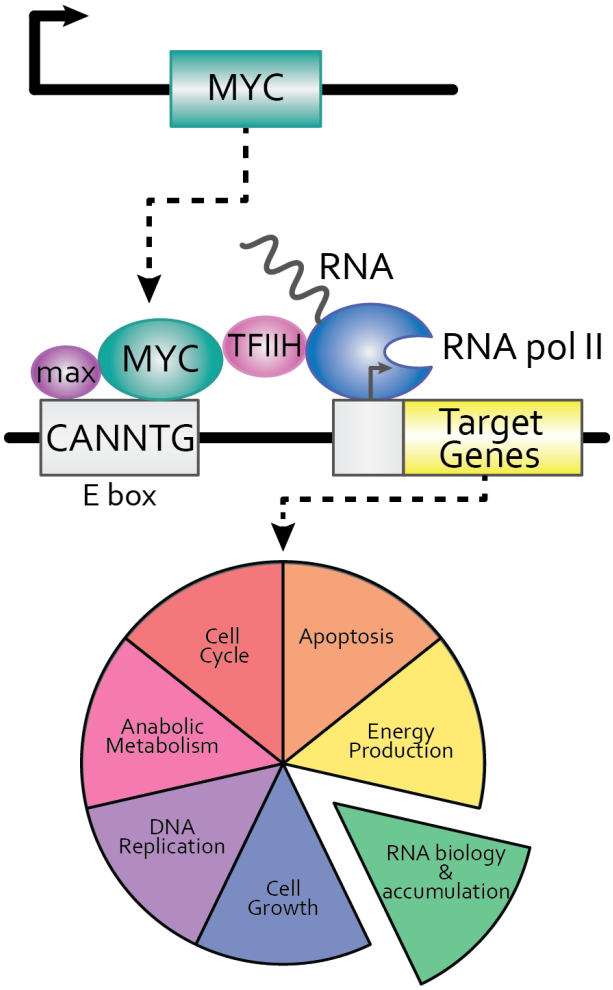

Figure 1.1: **MYC regulates cell proliferation.** MYC regulates transcription as a hetero-dimer with MAX by binding the E-box sequence (CANNTG) in the promoter region of its targets. Target genes of MYC include several genes involved in cell growth, apoptosis, RNA biology and accumulation, etc. that are necessary for both healthy proliferating cells and cancer cell transformation.

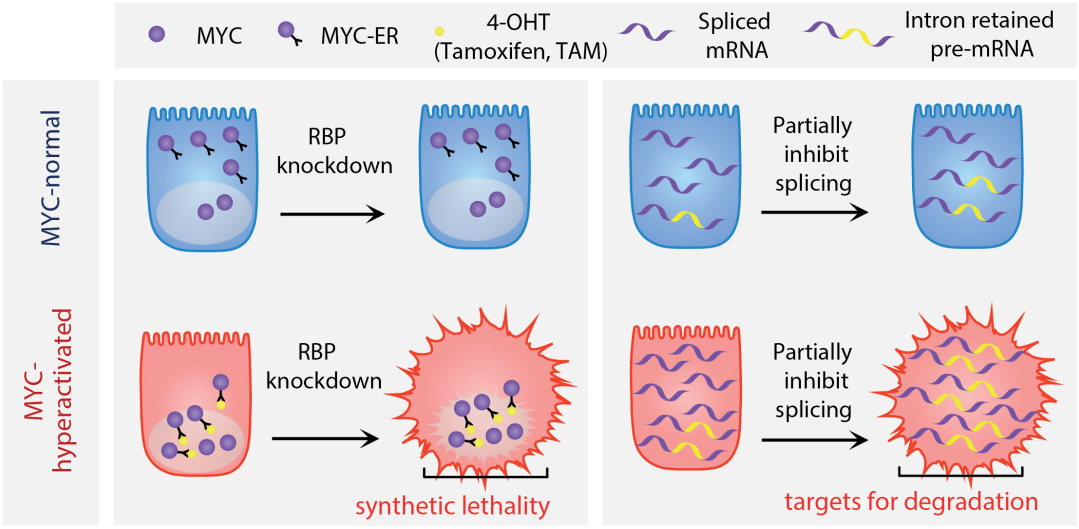

Modified from Hsu et al. *Nature* (2015)

Figure 1.2: **MYC-ER fusion cell model enabled the finding that core spliceosomal proteins are essential for MYC-dependent cell growth.**
Schematic of MYC-ER fusion system (left). MYC-ER fusion is retained in the cytoplasm until exposure of tamoxifen (TAM) ligand. Ligand-bound fusion protein is translocated to the nucleus for transcriptional activation of MYC's target genes. RBPs were screened for knockdowns that caused lethality of MYC-hyperactive cells (left). Hsu et al. identified that inhibiting RBP splicing factors caused widespread intron retention leading to selective cell death in MYC-hyperactive cells.

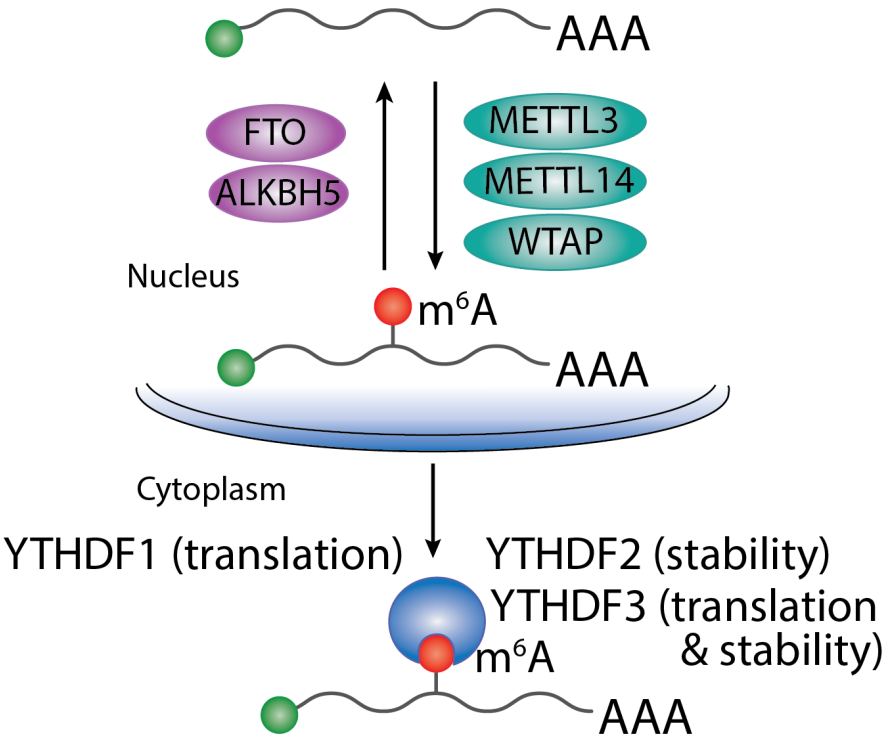

Figure 1.3: **m^{6}A reader proteins determine the fate of m^{6}A-containing mRNAs.** Deposition of m^{6}A-modifications on an mRNA is dynamic and reversible. m^{6}A is "written" by a catalytic core complex comprising Methyltransferase-like protein 3 (METTL3) and Methyltransferase-like protein 14 (METTL14) together with a regulatory protein complex including Wilms tumor 1-associated protein (WTAP). m^{6}A is "erased" by fat mass and obesity-associated protein (FTO) or α-ketoglutarate-dependent dioxygenase alk B homolog 5 (ALKBH5). m^{6}A-containing mRNAs are transported to the cytoplasm where their fates are determined by YTH-domain containing proteins including mRNA stabilization for translation or active recruitment of mRNA to degradation machinery.

Chapter 2

Pooled CRISPR-Cas9 screening identifies YTHDF2 as a putative therapeutic target for TNBC

2.1 Introduction

In the past, gene knockdown using RNA interference (RNAi) has been the gold standard for systematic evaluation of normal gene function. Due to the scalable nature of RNAi, it has been adapted for use in large-scale functional genomic studies. However, lately the clustered regularly interspaced short palindromic repeats (CRISPR)-Cas9 system has overcome many limitations of RNAi, including incomplete protein depletion and off-target effects (Jackson et al., 2003; Morgens et al., 2016). The CRISPR-Cas9 system provides an effective method for inducing double stranded breaks at specific genomic loci, guided by single guide (sg) RNAs that are

designed to be homologous to genomic regions upstream of an NGG sequence (protospacer adjacent motif; PAM) in human cells (Cho et al., 2013; Mali et al., 2013; Sternberg et al., 2014). Use of CRISPR-Cas9 gene editing produces one of three genotypes, true knockouts, heterozygotes, and wild-type cells, which in pooled scenarios is an advance over shRNA-mediated knockdown which suffers from knockdown variability depending on the site of transgene integration (Morgens et al., 2016; Seibler et al., 2005). In addition, sgRNAs can target both protein-coding sequences and regulatory elements including promoters, enhancers, micro (mi)RNAs and long noncoding RNAs (Peng et al., 2015). As a result, the CRISPR-Cas9 system has become the superior method for large-scale pooled screening systems.

Large-scale CRISPR-Cas9 pooled screens offer a system for the unbiased knockout of a gene set using a pool of CRISPR-Cas9 lentiviral ('lentiCRISPR') vectors that individually target different genomic loci. This system was originally used to develop a genome-wide lentiCRISPR knockout library, which was first applied to successfully conduct both positive and negative selection screens to identify key resistance and essential genes in various cell models (Shalem et al., 2014; T. Wang et al., 2014). The high success and sensitivity of these studies have made it possible to efficiently identify a set of genes underlying specific cellular interactions in an unbiased manner. Current libraries target over 18,000 genes across the genome (genome-scale) but are limited to 3-4 sgRNAs per gene (Shalem et al., 2014; T. Wang et al., 2014). This introduces a high probability for false positive and negative hits and low reproducibility, as many studies have shown that sgRNA efficiencies are highly dependent on specific sequence features, rendering some sgRNAs less active than others (Doench et al., 2014; H. Xu et al., 2015).

Here, we present a pooled CRISPR-Cas9 library targeting approximately 1,000 human RBPs, designed using prediction tools that identify efficient sgRNAs based on sequence fea-

tures including preference for guanines and disfavor of thymines proximal to the PAM sequence and specificity of nucleotides downstream of the guide sequence (H. Xu et al., 2015). The library contains 10 sgRNAs per gene, including a subset of nontargeting sgRNAs, sgRNAs that target essential genes and sgRNAs that target fluorescent proteins. The smaller library size enables a specific focus on RBPs and also minimizes cell numbers needed to maintain complexity, extending the screen's potential application to slow growing, hard-to-culture cells, and *in vivo* screens. We increased the number of sgRNAs targeting each gene to limit the prevalence of false positive and negative hits and improve reproducibility to address the limitations of genome-scale libraries. This RBP-focused CRISPR knockout library, created by careful curation of known and predicted RBPs (Gerstberger et al., 2014), is a unique reagent resource that can be readily applied to investigate the function of RBPs in any biological context with cell reporters that support pooled screening readouts. In this chapter, we apply this focused CRISPR knockout library to screen for RBPs that are synthetic lethal with amplified MYC expression and we uncover several RBPs that are involved in splicing, mRNA turnover and translation that uniquely contribute to MYC-dependent cancer cell growth and survival.

2.2 Results

2.2.1 Construction of the RBP-specific CRISPR-Cas9 library

To phenotypically screen for RBP dependencies in cancer, we designed and developed a CRISPR-Cas9 library targeting RBPs. We designed (Cao et al., 2017) 10 single-guide (sg)RNAs for each of 1,078 RBPs (Gerstberger et al., 2014) and included sgRNAs targeting 628 essential genes positive controls, 1,058 non-targeting sgRNAs as negative controls and 12 sgRNAs

targeting fluorescent proteins as controls for potential fluorescent reporters (Addgene #141438) (Wheeler et al., 2020). We included 10 sgRNAs per gene to limit false hits and as an improvement, our library requires a lower minimum cell number than genome-scale libraries do to maintain library complexity (**Figure 2.1A**). Lentiviral vectors were assembled by cloning an equimolar pool of sgRNA oligonucleotides (oligos), synthesized from an oligo array into a lentiviral backbone with active Cas9 expression (**Figure 2.1A**). High-throughput sequencing confirmed that the plasmid library maintained sgRNA coverage and aliquots were tightly correlated (less than 0.065% of sgRNAs received low normalized read counts; **Figure 2.1B**).

2.2.2 Identification of critical RBPs in MYC-dependent cancer

In cancer, tumor cells respond to intrinsic and extrinsic signals by assuming control of post-transcriptional mechanisms to modulate protein expression levels in order to facilitate adaptation to the tumor microenvironment (Pereira et al., 2017). While RBPs are dysregulated in several cancer types, a relatively low percentage of RBPs harbor somatic mutations (Sebestyen et al., 2016). Therefore, it is challenging to formally identify RBPs as drivers or passengers without systematic functional studies.

To identify RBPs that are selectively required to sustain MYC's oncogenic gene regulatory program, we employed a MYC-ER HMEC synthetic lethality model based upon the hypothesis that the mutation of two genes (MYC and an RBP candidate) leads to cell death, while the mutation of either gene individually is tolerated (Kessler et al., 2012). In biological duplicate, we transduced human mammary epithelial cells engineered with an inducible MYC-estrogen receptor fusion transgene (MYC-ER HMECs) with the lentiCRISPR RBP library by spinfection, selected for transduced cells with puromycin, treated half of the cells with tamoxifen (TAM) to

induce MYC activity and isolated genomic DNA (gDNA) 8 and 16 days after puromycin removal (**Figure 2.2A**). The representation of randomly integrated sgRNAs was tightly correlated with their frequencies in the original plasmid library and replicate libraries were highly correlated (**Figure 2.2B-2.2C**). We observed a significant reduction in sgRNA diversity in surviving cells on days 8 and 16 compared with day 0 in both MYC-induced (MYC) and uninduced control, indicating dropout of cells transduced with sgRNAs targeted to essential genes (positive controls; **Figure 2.2D-2.2F**). Approximately 5% more genes were depleted on day 16 than day 8, therefore, day 16 sequencing data was used for further analysis since CRISPR editing was more complete.

Using the MaGeCK software package (v0.5.4) (W. Li et al., 2015), we identified depleted sgRNAs and calculated p-values and β scores using maximum likelihood estimation where β scores reflect the "extent of selection" in the MYC-induced population compared with control. Our analysis presented several RBPs that have been implicated in MYC-mediated control of gene expression, including PTBP1 (Cobbold et al., 2010; He et al., 2014), PCBP2 (Wan et al., 2016), ELAVL1 (Lafon et al., 1998) and TRA2β (Park et al., 2019) and identified $\sim$40 RBPs with no known roles in this context. A total of 57 RBP candidates ($p < 0.05$) were depleted in MYC-induced cell populations compared to control. We observed enrichment for genes involved in the negative regulation of macromolecule metabolic processes, including several genes that repress exon inclusion (*HNRNPA2B1*, *PTBP1*, *SRSF9*), genes that repress transcription (*ZGPAT*, *SLTM*), genes that regulate mRNA turnover (*YTHDF2*, *UPF3B*, *UPF3A*, *XRN1*, *DCP2*, *AGO2*) and genes that inhibit translation initiation (*EIF4ENIF1*, *EIF4E2*) (**Figure 2.2G**). This suggests a MYC-dependent vulnerability by RBPs that reduce the stability of mRNAs for translation, or RBPs that reduce the translation and production rate of encoded proteins.

2.2.3 Expression analysis of RBP candidates in patient data

We next cross referenced public data from The Cancer Genome Atlas (TCGA) pan-cancer clinical data resource (Liu et al., 2018) and found that 67% of our RBP candidates are highly expressed in basal-like (triple-negative) tumors, which are typically MYC-dependent, while expression was significantly lower in luminal A/luminal B (estrogen receptor/ progesterone receptor/ human epidermal growth factor receptor 2 [ER/PR/HER2] positive) tumors, which are typically MYC-independent (Green et al., 2016) (**Figure 2.3A**). Together, our results indicate that several RBPs controlling different stages of the RNA life cycle become aberrantly expressed in TNBC and further functional analysis may provide new therapeutic avenues for treating MYC-driven cancers.

In addition to several studies implicating aberrant mRNA methylation (Lan et al., 2019) and expression of m^6A methyltransferases, demethylases, and m^6A-binding proteins in various cancers (Huang et al., 2018; Su et al., 2018; Weng et al., 2018), we identified that the m^6A reader protein YTH domain family 2 (YTHDF2) is significantly upregulated in TNBC compared to receptor positive breast cancers (**Figure 2.3B**) and therefore, we chose to further validate the synthetic lethality of YTHDF2 depletion with MYC-induction from this dataset.

2.2.4 Validation of YTHDF2 synthetic lethality *in vitro*

We first verified that loss of *YTHDF2* protein expression causes MYC-dependent cancer cell death by orthogonal validation using two independent short hairpin (sh)RNA-mediated knockdowns of YTHDF2 (shYTHDF2-1 and shYTHDF2-2) (**Figure 2.4A**). We observed a significant increase in apoptotic, Annexin V-positive cells and early cell death in MYC-induced HMECs compared to controls by fluorescence-activated cell sorting (FACS) ($p \leq 0.05$) (**Figure**

2.4B-2.4D). We also confirmed a functional, epistatic association between YTHDF2 with m^6A-modified RNA targets using shRNA mediated knockdown of m^6A writer, METTL3 (shMETTL3), which similarly triggered apoptotic cell death (**Figure 2.4A-2.4D**). After several days, there was significantly more MYC-induced, YTHDF2-depleted HMECs containing 2N DNA content, suggesting accumulation of dead cells at the G1 checkpoint of the cell cycle (**Figure 2.4E-2.4F**). We then compared the proliferation rate among MYC-dependent, triple negative MDA-MB-231 breast tumor-derived cells and secondary lung metastatic MDA-MB-231-LM2 cells to MYC-independent, hormone receptor-positive MCF-7 and SKBR3 breast tumor-derived cells following YTHDF2 depletion by time lapse microscopy. This analysis revealed significantly reduced proliferation rates in MYC-dependent, YTHDF2-depleted cell lines but not in MYC-independent YTHDF2-depleted cell lines compared with non-targeting controls (NTC). (**Figure 2.4G-2.4H**).

2.2.5 Validation of YTHDF2 synthetic lethality *in vivo*

In parallel, to determine the importance of genes encoding regulators of mRNA turnover on MYC-dependent tumor growth *in vivo* we generated a pool of MDA-MB-231-LM2 cells transduced with various doxycycline (DOX) inducible shRNAs targeting several proteins mediating RNA stability, three of which target YTHDF2, and assessed dropout of shRNAs both *in vitro* cultured cells and *in vivo* by subcutaneous mouse xenografts (**Figure 2.5A**, **Table 2.1-2.2**). Cells expressing YTHDF2-targeting hairpins were significantly depleted in resected tumors, in parallel with in vitro cultured cells ($p \leq 0.001$), indicating a growth disadvantage in breast tumor cells upon silencing of YTHDF2 (**Figure 2.5B-2.5D**). To confirm that depletion of YTHDF2 negatively affects tumor growth *in vivo* we generated an MDA-MB-231-LM2 cell line transduced with the individual DOX inducible shRNA that was depleted in the tumor cell pool (**Figure 2.5E**). After

initial tumor engraftment, we found that the growth rate of tumors containing cells expressing the YTHDF2-targeting shRNA was reduced compared with uninduced tumors (**Figure 2.5F**). Consistently, after 35 days, the final volumes of tumors from DOX treated mice (+DOX) were significantly smaller than tumors from vehicle treated mice (-DOX) (**Figure 2.5G-2.5H**). In addition to fewer proliferating cells, we observed increased Caspase-3 cleavage and a reduction in host angiogenic vascular endothelial cells in tumors from +DOX mice (**Figure 2.5I-2.5K**).

2.2.6 Evaluation of the safety and efficacy of targeting YTHDF2 as therapy in patients

To verify conservation of this phenotype in human cancer patients, we cross-referenced RNA-seq data from the TCGA pan-cancer clinical data resource (Liu et al., 2018). Indeed, patients with triple negative tumors exhibiting high MYC expression were more likely to survive if their tumors presented below average levels of *YTHDF2* mRNA based on Kaplan-Meier probability ($p \leq 0.005$) (**Figure 2.6A**). Next, we aimed to evaluate the efficacy and safety of targeting YTHDF2 as a treatment for patients with MYC-dependent cancer. We generated *CAG-CreERT ;Ythdf2*$^{fl/fl}$ mice by crossing CAG-CreERT mice with previously generated Ythdf2$^{fl/fl}$ mice (Z. Li et al., 2018) to expose any effects on the viability of healthy cells in other organs. Systemic genetic depletion of *Ythdf2* resulted in no gross physiological abnormalities or changes in body weight for at least four weeks following TAM administration, suggesting that inhibition of *Ythdf2* in an intact organism has no adverse effects in non-cancerous somatic tissues (**Figure 2.6B**). Thus, cells appear to only be affected by changes in YTHDF2-mediated regulation if the cells in the tissue are predisposed to MYC addiction.

2.3 Discussion

The RBP CRISPR-Cas9 library we designed and constructed enables the systematic evaluation of RBP function and aids in the identification of targetable RBP-mRNA interactions in various isogenic disease models or physiologic systems. We have greatly improved upon previous genome-scale unbiased detection methods by reducing the library size to specifically focus on RBPs with a targeting depth of 10 sgRNAs per RBP, which promises the identification of high-confidence hits. We demonstrated high reproducibility between replicates, significant dropout of essential genes over several days, and identification of several synthetic lethal candidates in similar functional families.

Our RBP-focused CRISPR-Cas9 knockout library has enabled the discovery of several new classes of RBPs that are essential for MYC-dependent cancer cell viability including RBPs that regulate transcription, mRNA stability, ribosome recruitment and translation. This greatly expands on previous reports that only highlight dysregulation of spliceosomal proteins as a MYC-dependent vulnerability, causing global intron retention and mis-regulation of essential cellular processes (Hsu et al., 2015). Here, we illuminated multiple aspects of RNA processing as vulnerabilities in MYC-driven cancers, however, we specifically focus on the process of mRNA turnover and how it is fundamental for MYC-driven cancers to maintain oncogenic growth by balancing mRNA homeostasis and protein synthesis rates.

Among the RBPs we identified that regulate cytoplasmic mRNA turnover, we decided to further investigate the role of m^6A reader, YTHDF2. We demonstrate that depletion of YTHDF2 triggers apoptosis in MYC-dependent cancer cells using *in vitro* cell culture models and *in vivo* tumor xenografts while sparing MYC-independent cancer cells. Notably, we observed that depletion of YTHDF2 reduced tumorigenic potential in solid tumors, exhibiting lower levels of prolif-

eration, higher levels of apoptotic cells and impaired angiogenesis. While previous studies have also suggested that YTHDF2 may protect cancer cells from apoptosis (M. Chen et al., 2018; Paris et al., 2019), this is the first report connecting the function of YTHDF2 to MYC activity, providing an explanation for contradictory evidence presented in other cancer cell types (Zhong et al., 2019).

Importantly, we found that expression of YTHDF2 is critical for the survival of MYC-dependent breast cancer cells, while it is dispensable for MYC-independent cancer cells likely due to the constitutively elevated levels of transcription and translation in cells with aberrantly high MYC activity. Our model is supported by gene expression analyses of TNBC tumors that associate low YTHDF2 abundance with longer patient survival rates and we demonstrate the efficacy and feasibility of depleting YTHDF2 as a potential therapeutic strategy in cancer by procuring viable systemic *Ythdf2* knockout mice. In addition, there is recent evidence that YTH-paralogs may play compensatory roles for one another, which provides anticipation for minimal adverse side effects (Zaccara & Jaffrey, 2020). All together, we demonstrate that since healthy tissues often remain unaffected by RNA expression level changes that drastically affect a cancer cell, targeting disease-maintaining RBP-RNA interactions shows great promise for a minimally toxic and highly specific treatment option.

2.4 Materials and Methods

2.4.1 Cell Culture

Immortalized human cell lines were used in this study. HEK293xT, MDA-MB-231, MDA-MB-231-LM2, and MCF-7 cells were cultured in DMEM supplemented with 10% fetal bovine serum. SKBR3 cells were cultured in McCoy's 5A Medium supplemented with 10% fetal bovine serum. Cells were passaged every 3 or 4 days with TrypLE EXPRESS (Life Technologies) using standard methods. MYC-ER HMECs were cultured in Medium 171 supplemented with MEGS (Life Technologies). Cells were passaged every 3 or 4 days with TrypLE EXPRESS and Defined Trypsin inhibitor. Cells were maintained in a humidified incubator at 37°C with 5% CO_2.

2.4.2 Animal Studies

Animal protocols were approved by the Institutional Animal Care and Use Committee at Baylor College of Medicine and at University of California San Diego. Athymic Nude-Foxn1nu were purchased from Envigo International Holdings, Inc. *CAG-CreERT* mice (Jackson labs, stock number 004682) were mated with *Ythdf2*$^{fl/fl}$ mice (generous gift from Dr. Chuan He, University of Chicago) to produce *CAG-CreERT;Ythdf2*$^{fl/fl}$ mice. To induce recombination at 8 weeks of age both *CAG-CreERT;Ythdf2*$^{fl/fl}$ and *Ythdf2*$^{fl/fl}$ littermates were injected with 75 mg/kg body weight.

2.4.3 CRISPR plasmid library cloning

A comprehensive list of sgRNA sequences projected to efficiently direct Cas9 cleavage at their target sites was generated using the sequence model, CRISPR-FOCUS (Cao et al.,

2017) and ordered as a pool of equal molar oligos. The lentiCRISPR RBP plasmid library was cloned using previously reported methods (Shalem et al., 2014). Briefly, the lentiCRISPR v2 backbone was digested using BsmBI restriction sites and sgRNA oligonucleotide inserts were PCR amplified and Gibson-assembled using 36 parallel electroporations to maintain a 300X library complexity. Transformations were spread on fourteen 24.5 x 24.5 cm carbenicillin selection agar plates. Colonies were grown for 16-18 hours at 32°C. The next day, colonies were scraped off the plates and the cell pellet was maxiprepped ($\sim$0.9 g cells/column). Plasmid library was stored at -20°C. The plasmid library is available on Addgene (#141438).

2.4.4 Lentivirus production and purification

HEK293xT cells were seeded on twelve 15 cm plates cells at 40% confluency the day before transfection. One hour prior to transfection the media was removed and replaced with 8 mL of pre-warmed OptiMEM. Transfections were performed using 62.5 μL Lipofectamine 2000, 125 μL Plus reagent, 12.5 μg lentiCRISPR plasmid library, 6.25 μg of pMD.2g, and 9.375 μg psPAX2. Media was changed 6 hours after transfection to DMEM + 10% FBS. After 48 hours, the supernatant was filtered through a 0.45 μm low protein binding membrane. The virus was then ultracentrifuged at 24,000 rpm for 2 hours at 4°C and resuspended overnight at 4°C in PBS. Virus aliquots were stored at -80°C.

2.4.5 Multiplicity of infection

For each new cell type, the volume of virus to achieve an MOI of 0.3 was determined by titrating virus in each well (between 5 and 50 μL). 1.5x10^6 cells per well of a 24-well plate were spinfected in medium supplemented with 8 μg/mL polybrene at 2,000 rpm for 2 hours at 37°C.

Media (without polybrene) was replaced after the spin and incubated overnight. Cells were split the next morning and half the cells from each condition were treated with puromycin (Thermofisher Scientific; A1113803). Cells were counted after 3-4 days and MOI was determined by the volume of virus that allowed 30% of the cells to survive.

2.4.6 MYC-ER HMEC RBP CRISPR screen

For each replicate, 3x10^6 cells were spinfected in 5 wells of a 12-well plate in medium supplemented with 8 μg/mL polybrene (Millipore Sigma; TR-1003-G) and spun at 2,000 rpm for 2 hours at 37°C. 2X the amount of virus determined by MOI was added per well. After spinfection, media was replaced (without polybrene) and incubated overnight. The next morning, 5 wells from each replicate were pooled and split onto two 10 cm plates per replicate. Media was replaced containing 2 μg/mL puromycin (Thermofisher Scientific; A1113803) after 6 hours. Media was changed every 2 days and puromycin was removed after 4 days. 4x10^6 cells were collected and snap frozen in an ethanol, dry-ice bath from each replicate as the day 0 timepoint. 4x10^6 cells were plated per 15 cm plate for a total of 2 plates per replicate. One plate from each replicate was treated with 15nM 4-Hydroxytamoxifen (4-OHT) (Millipore Sigma; H7904). Cells were cultured for an additional 16 days, changing media and 4-OHT every 2 days, and splitting cells every 4 days, always at a minimum of 4x10^6 cells per 15 cm plate. 4x10^6 cells were harvested on day 8 and day 16 per condition for each replicate and snap frozen.

2.4.7 Bulk CRISPR gRNA library preparation

DNA Preparation

DNA libraries were prepared using a targeted-enrichment approach. gDNA was extracted from pellets of 4 million cells using DNeasy Blood and Tissue kit (Qiagen; 69504) eluted in 130 μL, with typical yields of 150 ng/μL. gDNA samples were sonicated to 1000 bp by Bioruptor. Average fragment size was determined with genomic DNA ScreenTapes on the Agilent Tapestation (Agilent; 5067-5365).

Probe Generation

To selectively enrich sgRNA-containing regions in the genomic DNA, we generated two antisense probes by PCR amplification of a 500 nt constant region flanking the sgRNA sequence. Corresponding 592 nt and 574 nt biotinylated RNA probes were generated using HiScribe T7 High Yield RNA Synthesis Kit (NEB; E2040S) with bio-CTP (Thermo; 19519016), and bio-UTP (Sigma/Roche; 11388908910) nucleotides.

PCR Primer set 1:

Fwd: GGGATATTCACCATTATCGTTTCAGACC

Rev: GGATTCTAATACGACTCACTATAGGGTGTTTCGTCCTTTCCACAAGA

PCR Primer set 2:

Fwd: GGTGTATCTTCTTCTGGCGGTTC

Rev: GGATTCTAATACGACTCACTATAGGGCAAGTTAAAATAAGGCTAGTCCGTTATCA

Probe Capture

1% of 1 M DTT was added to genomic DNA for a final concentration of 10 mM. Concentration of probes was determined for each sample as 10% of the total DNA yield (in micrograms), diluted in water to a final volume of 10 μL. Samples were placed in a pre-heated thermomixer set at 95°C with interval mixing (1200 rpm, 30 second on/1 min off). Immediately after adding the samples, the temperature was changed to 65°C to begin cooling. When cooled to 65°C, 10 μL of probes were added, followed by 73.5 μL of 3X Hybridization buffer (75 mM Tris, 15 mM EDTA, 1.2 M LiCl, 3 M Urea, 0.3% NP-40, 0.3% SDS, 0.3% DOC). Incubation was performed with interval mixing as follows: 65μC 5 min, 64μC 5 min, 63μC 5 min, 62μC 5 min, 61μC 150 min.

Streptavidin Capture

30 μL of streptavidin beads (Invitrogen; 11205D) per 1 μg of probes were used for each sample, washed with 500 μL of 1X Hybridization buffer and resuspended in 20 μL of 1X Hybridization buffer. Following probe capture, 14 μL of beads (75%) were added to each sample and incubated for 15 mins at 62°C with interval mixing. Supernatant was removed and transferred back into the tube with the remaining 25% of the beads for a second round of hybridization (62°C with interval mixing for 15 mins). Meanwhile, the collected 75% of the beads (on magnet) were resuspended in 200 μL pre-warmed 1X Hybridization buffer and incubated for 5 mins at 37°C. Supernatant was discarded and tubes were kept on ice. Following the second 15 min incubation, supernatant was discarded from the tube containing the remaining 25% of the beads and beads were resuspended in 200 μL pre-warmed 1X Hybridization buffer for 5 mins at 37°C. Samples were combined by resuspending all beads in 54 μL of LoTE (100 mM NaCl, 0.25%

NP-40) + 6 μL of RNase Cocktail (Thermo; AM2286) and incubated at 37°C for 10 mins. 6 μL of 1M NaOH was added followed by incubation at 70°C for 10 minutes. Supernatant was transferred to a fresh tube and a second elution was performed by resuspending beads in 30 μL of 100 mM NaOH and incubated at 70°C for 2 mins with shaking. Supernatant was combined with first transfer. 9 μL of 1 M HCl was added to the final sample and DNA cleanup was performed with Zymo DNA concentrator-5 kit (Zymo; D4014) following manufacturer's instructions, eluted in 40 μL of pre-warmed water.

PCR amplification

First PCR. 100 μL per sample and split into 2x 50 μL samples in strip tubes: 40 μL DNA, 50 μL 2X Q5 PCR mix (NEB; M0492L), 5 μL of each primer at a concentration of 20 μM. PCR program: 98°C 30 sec, 98°C 15 sec, 68°C 1 min, 72°C 1 min, GOTO step2 9 times, 72°C 2 min, HOLD 4°C.

Primers:

Fwd: CCTACACGACGCTCTTCCGATCTTGTGGAAAGGACGAAACACCG

Rev: GTTCAGACGTGTGCTCTTCCGATCTCCACTTTTTCAAGTTGATAACGGACTAGCC

Cleanup was performed with 1.8X AmpureXP beads (Beckman Coulter; A63881) according to manufacturer's instructions, eluted in 40 μL water for second PCR input. Second PCR. 100 μL per sample was split into 2x 50 μL reactions in strip tubes: 40 μL DNA elution from 1st bead cleanup, 50 μL 2X Q5 mix, 5 μL each of 20 μM Illumina sequencing primers. PCR program: 98°C 30 sec, 98°C 15 sec, 68°C 1 min, 72°C 1 min, GOTO step2 6 times, 72°C 2 min, HOLD 4°C. Performed bead cleanup with 1.4X AmpureXP beads according to manufacturer's instructions. Elution was performed in 20 μL water. Library size (260 bp) and concentration

were calculated using D1000 Tapestation (Agilent; 5067-5582) and sequenced to 2M reads per library on the Hi-Seq4000 in single-end 75 bp mode.

2.4.8 Annexin-V/ PI apoptosis assay

MYC-ER HMECs were transduced with non-targeting control (NTC; Millipore Sigma; SHC002), TRC lentiviral shRNA vector YTHDF2 (shYTHDF2-1; Millipore Sigma; TRCN0000168751), TRC lentiviral vector YTHDF2 (shYTHDF2-2; Millipore Sigma; TRCN0000167813) or TRC lentiviral shRNA vector METTL3 (shMETTL3; Millipore Sigma; TRCN0000034717) lentivirus at MOI $>$ 1 and selected for 2-3 days with 2μg/mL puromycin (Thermofisher Scientific; A1113803). MYC expression was induced with 15nM 4-OHT for 24 hours. The Annexin-V apoptosis assay was performed using the AnnexinV-FITC kit (BD Biosciences; BDB556547) according to manufacturer's instructions. Cells were analyzed by flow cytometry using the BDSLRFortessa under the FITC (Annexin V) and PerCP-Cy5 (Propidium Iodide) channels with compensation. Analysis and gating were performed in FlowJo.

2.4.9 Time Lapse Microscopy

Cells were seeded at 5K cells in Incucyte ImageLock plates (Essen BioSciences; 4379). The next day, plates were loaded into the Incucyte and imaged at 10X magnification for 84 hours every 12 hours. Phase images were analyzed using the Incucyte ZOOM Basic Analyzer to measure confluence.

2.4.10 Pooled *in vivo* shRNA screen and analysis

MDA-MB-231-LM2 breast cancer cells were individually transduced at MOI of 1.2-1.5 with doxycycline-inducible shRNAs (shRNA targeting RNA metabolism genes were cloned from GIPZ plasmid to pINDUCER11 backbone): GIPZ lentiviral shRNA vector YTHDF2 (Dharmacon; V2LHS_115143), (Dharmacon; V2LHS_115142), (Dharmacon; V3LHS_381614) All cell lines were sequentially pooled in equal ratios. The obtained pool was subcutaneously transplanted (3 X 10^6 cells per mice) into athymic nude mice (female mice, 4-6 weeks old). Mice were randomized onto and maintained on 5% sucrose water (-Dox) or 5% sucrose water with 2 mg/mL dox (Sigma Aldrich; D9891) (+Dox) 3d post-transplantation. Tumors were measured using calipers and harvested when they reached 1000 mm3, approximately 2-3 weeks after engraftment and cells cultured *in vitro* were carried out for 12 population doublings. Genomic DNA from dissected tumors was isolated using the QIAamp DNA mini kit (Qiagen), and shRNA library was amplified using the following primers (5'-3'):

forward: TCGTCGGCAGCGTCAGATGTGTATAAGAGACAGTAGTGAAGCCACAGAGT;

reverse: GTCTCGTGGGCTCGGAGATGTGTATAAGAGACAGGGCGCGGAGGCCAGATCTT;

The library was indexed using Nextera Index Kit (96 indices) (Illumina; KAPA#KK4824) and purified using PippinHT. The library was quantified using KAPA Library Quantification Kit (Illumina; FC-131-1096) and sequenced at Illumina HIseq platform ($\sim$10x10^6 reads per tumor with a read coverage of $>$10000 reads per shRNA per tumor). Reads were processed to remove adapter sequences using Cutadapt (Martin, 2011) and then aligned to the reference library using Bowtie 2 (Langmead & Salzberg, 2012) in end-to-end mode allowing up to a maximum of 3 mismatches/indels compared to the reference sequence. The raw number of reads mapping to each shRNA in each sample was then extracted from the SAM files and DESeq2-v.1.14.0

(Love et al., 2014) and was used to determine the normalized abundance of each shRNA in the vehicle and dox-treated tumors.

2.4.11 *In vivo* tumorgenicity assays

MDA-MB-231-LM2 breast cancer cells were transduced with validated YTHDF2-targeting pINDUCER11 shRNA 1 (Dharmacon; V2LHS_115143) and sorted for the top 10% of EGFP expressing cells on a BD Influx Cell Sorter. Cells were expanded and then subcutaneously transplanted (3 X 10^6 cells per mice) into athymic nude mice (female mice, 3-4 weeks old). Mice were randomized onto and maintained on 5% sucrose water (-Dox) or 5% sucrose water with 2 mg/mL dox (Sigma Aldrich; D9891) (+Dox) 14d post-transplantation. Tumors were measured twice, weekly using calipers and harvested when they reached 1000 mm^3 on average and tumors were sectioned and either fixed in 4% paraformaldehyde for IHC analysis or snap frozen and cryopulvierized for RNA and protein extraction.

2.4.12 Immunohistochemistry

Tumor samples were fixed in 4% paraformaldehyde and then paraffin-embedded. Microtome sectioning and hematoxylin/eosin staining were performed by the Moores Cancer Center Histology Core. 5 μm thick sections were deparaffinized in Citrisol and rehydrated with graded alcohols. Epitope retrieval was performed by boiling slides for 10 min in sodium citrate buffer (10mM Sodium citrate, 0.05% Tween 20, pH 6.0). DAB staining was performed using Rabbit Specific HRP/DAB (ABC) Detection IHC Kit (Abcam; ab64261) according to manufacturer's instructions. The following antibodies were incubated overnight in 5% goat serum in wash buffer containing 0.025% Triton X-100 in PBS: Rabbit pAb anti-Ki67 (Abcam; ab15580), Rabbit mAb

anti-CD31 (Cell Signaling; 77699). Hematoxylin (Vector Laboratories; H-3502) was used as a counter stain according to manufacturer's instructions and slides were dehydrated before cover-slipping.

2.4.13 Western Blot

Cells were lysed with cold RIPA buffer (Thermofisher) with 200X Protease inhibitor and 100X phosphatase inhibitor. Protein was quantified using Peirce BCA Protein Assay Kit. Total protein extracts were run on 4%-12% NuPAGE Bis-Tris gels in NuPAGE MOPs running buffer (Thermofisher) and transferred to PVDF membranes. Membranes were blocked in 5% nonfat milk in TBST for 1 hour, incubated overnight at 4°C with the following primary antibodies: Rabbit pAb anti-YTHDF2 (Proteintech; 24744-1-AP), Rabbit pAb anti-METTL3 (Proteintech; 15073-1-AP), Mouse mAb anti-GAPDH (Abcam; ab8245), Rabbit mAb anti-Cleaved Caspase-3 (Cell Signaling; 9664), Rabbit pAb anti-RFP (Thermo Fisher; R10367), Rabbit pAb anti-GFP (Abcam; ab290), washed 3X for 5 minutes with TBST, incubated for 1 hour at RT in 5% nonfat milk in TBST with secondary HRP-conjugated antibody: Goat anti-Mouse IgG Secondary Antibody, HRP (Invitrogen; 31430), Goat anti-Rabbit IgG Secondary Antibody, HRP (Invitrogen; 31460) at 1:5000 dilution, and washed 3X for 5 minutes with TBST. Membranes were developed using Thermo Pierce ECL detection reagents.

2.4.14 RT-qPCR Analysis

RNA was extracted with Direct-zol RNA Miniprep kit by Zymo Research for three biological replicates and cDNA was synthesized from total RNA using High-Capacity cDNA Reverse Transcription kit (Applied Biosystems; 4368814) according to manufacturer's instructions. Real-

time PCR was performed using Power SYBR Green PCR Master Mix (Applied Biosystems). Values of gene expression were normalized to GAPDH expression and are shown as relative expression. Primers are as follows:

Mouse (5'-3'):

Gapdh_F GGGTCCCAGCTTAGGTTCAT;

Gapdh_R CCCAATACGGCCAAATCCGT;

Pecam1_F GACTCACGCTGGTGCTCTATGC;

Pecam1_R TCAGTTGCTGCCCATTCATCA;

Vegfr1_F CCACAATCACTCCAAAGAAAGGTATG;

Vegfr1_R TCAATTCTGTTTCCTAAGTTGCTGCT;

Human (5'-3'):

GAPDH_F GAAGGTGAAGGTCGGAGTC;

GAPDH_R GAAGATGGTGATGGGATTTC;

PECAM1_F CTGCTGACCCTTCTGCTCTGTTC;

PECAM1_R GGCAGGCTCTTCATGTCAACACT;

VEGFR1_F ATCATTCCGAAGCAAGGTGTGAC;

VEGFR1_R TCCTTCTATTATTGCCATGCGCT;

2.4.15 Statistical Analysis

Investigators responsible for monitoring and measuring the xenografts of individual tumors were not blinded. Simple randomization was used to allocate animals to experimental groups. All animal studies were performed per institutional and national animal regulations. Power analysis was used to determine the appropriate sample size to detect significant changes

in animal survival, which were based on previous survival analyses in our laboratory. All healthy animals with successfully xenografted tumors were included in analyses.

For hypothesis testing, variance was assumed normal for Student's t-test.

2.5 Acknowledgements

We would like to thank the Sanford Consortium Human Embryonic Stem Cell Core for allowing use of their instruments (BD Influx Cell Sorter, X-20 Fortessa, BioRad CFX 384, Incucyte (1S10OD025060), and Zeiss AxioImager). We would also like to thank the Tissue Technology Shared Resource at Moores' Cancer for histology processing. J.M.E is supported by the Ruth. L. Kirschstein F31 National Research Service Award (F31 CA217173) and Cancer Systems Biology Training Program (P50 GM085764 and U54 CA209891). The results published here are in part based upon data generated by the TCGA Research Network: https://www.cancer.gov/tcga.

Chapter 2, in part, is a reprint of material as it appears in: Wheeler EC.*, Vu AQ*, **Einstein JM**, DiSalvo M, Ahmed N, Van Nostrand EL, Shishkin AA, Jin W, Allbritton NA, Yeo GW. Pooled CRISPR screens with imaging on microraft arrays reveals stress granule regulatory factors. Nat Methods, doi:10.1038/s41592-020-0826-8 (2020). The dissertation author was the second author of this paper.

Chapter 2, in full is a reprint of material as it will appear in: **Einstein JM**, Perelis M, Chaim IA, Meena JK, Nussbacher JK, Tankka AT, Yee BA, Li H, Madrigal AA, Neill NJ, Shankar A, Tyagi S, Westbrook TF, Yeo GW. Inhibition of YTHDF2 triggers proteotoxic cell death in MYC-dependent cancer. *In preparation*. The dissertation author is the primary author of this paper.

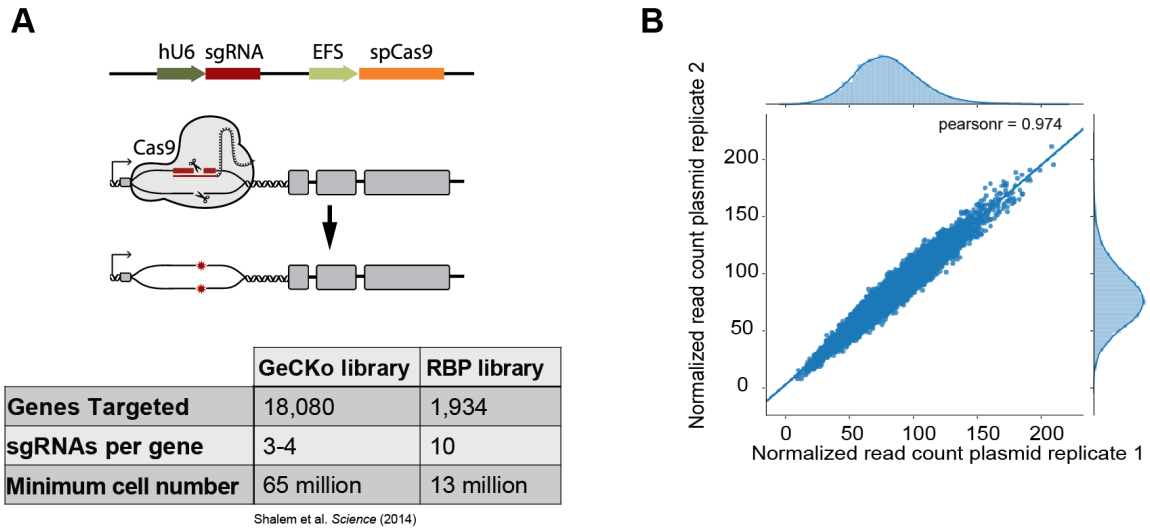

	GeCKo library	RBP library
Genes Targeted	18,080	1,934
sgRNAs per gene	3-4	10
Minimum cell number	65 million	13 million

Shalem et al. *Science* (2014)

Figure 2.1: **Construction of pooled RBP-targeting lentiCRISPR library.**
(A) CRISPR/Cas9 vector backbone exhibiting constitutive Cas9 expression for pooled library cloning. Mutations are generated by double-stranded breaks causing gene knockout. Table describes the differences in library construction between the RBP-targeted library compared to genome-scale libraries.
(B) Correlation of normalized read count between two replicates of plasmid library. R calculated by Pearson's coefficient.

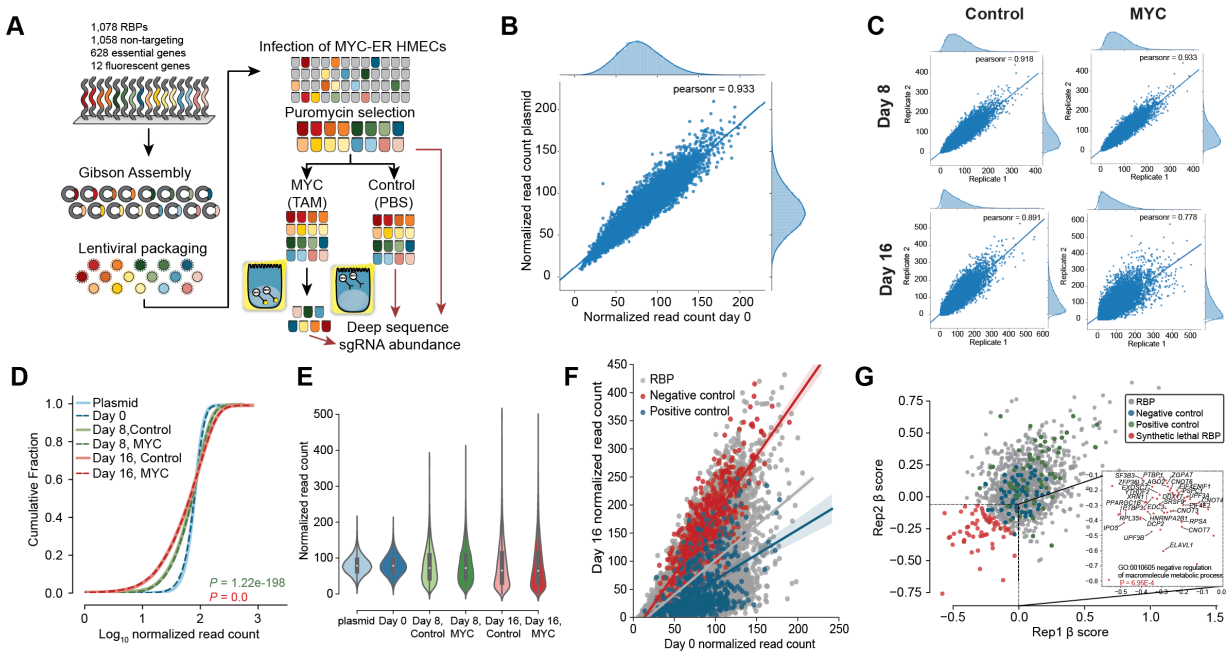

Figure 2.2: **Identification of critical RBPs in MYC-dependent cancer.**
(A) Schematic depicting the generation and implementation of the RBP-targeted CRISPR screen in MYC-ER HMECs.
(B) Correlation of normalized read count between plasmid library and cells infected with virus at day 0. Each condition is representative of two replicates. R calculated by Pearson's coefficient.
(C) Normalized read count comparing replicate samples on day 8 and 16 in both MYC-induced and control conditions. R calculated by Pearson's coefficient.
(D) Cumulative distribution of normalized read count of sgRNAs in each sample. Each condition is representative of 2 biological replicates. P-values were calculated compared to Day 0, control samples using two-sample Kolmogorov-Smirnov tests for continuous, one-dimensional probability distributions.
(E) Violin plot comparing normalized read count distributions in the plasmid library with infected cells on day 0, day 8, and day 16 in MYC-induced and control conditions. Each condition is representative of two replicates.
(F) Normalized read count of infected cells on day 16 compared with day 0. Genes are categorized by negative control (non-targeting), positive control (essential), and RBP. Each condition is representative of two replicates.
(G) Comparison of β scores for Day 16 replicates analyzed by MaGeCK (W. Li et al., 2015). β scores were calculated based off of the representation of sgRNAs in MYC-induced samples compared with their uninduced control. Representative of 2 biological replicates. Inset shows β score distribution of synthetic lethal candidate RBPs. RBP candidates enriched for the GO term "negative regulation of macromolecule metabolic process" are labeled.

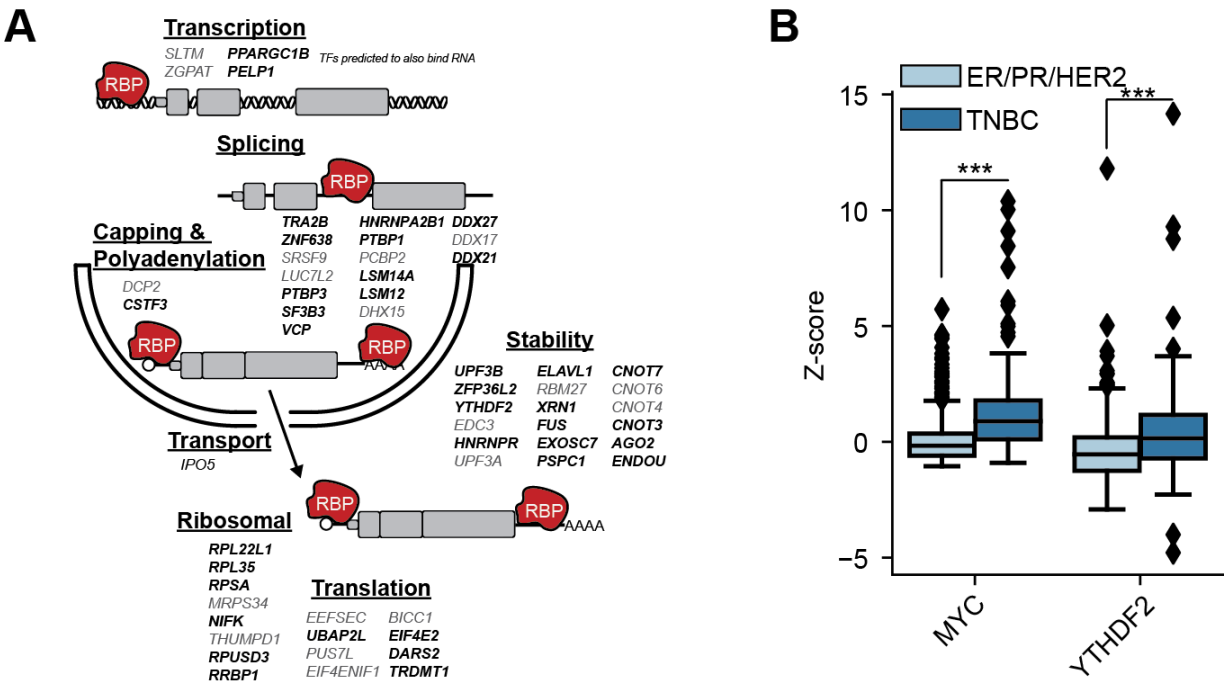

Figure 2.3: **Synthetic lethal RBP candidates are upregulated in TNBC.**
(A) Cartoon schematic indicating the function of RBP candidates identified from RBP CRISPR screen in MYC-ER HMECs. Bolded RBPs are significantly upregulated in basal-like (triple negative) tumors compared with ER/PR/HER2 positive tumors based on RNA-seq data downloaded from the TGCA Data Portal (Liu et al., 2018), p*$<$0.05. P-values were calculated by two-tailed Student's T-test.
(B) Box plot comparing mRNA expression levels for MYC and YTHDF2 between triple negative and ER/PR/HER2 positive tumors downloaded from the TCGA data portal (Liu et al., 2018). TNBC; n =171 independent samples, ER/PR/HER2; n = 732 independent samples. P-values calculated by Student's T-test.

Figure 2.4: **Depletion of YTHDF2 reduces proliferation in MYC-dependent cell lines.**
(A) Western blot confirming shRNA-mediated knockdown of YTHDF2 (shYTHDF2) and METTL3 (shMETTL3).
(B) Annexin-V/ Propidium iodide (PI) staining and FACS analysis representing a single replicate of YTHDF2 and METTL3 knockdown with (blue) and without (red) 24 hours of MYC-induction.
(C) Quantification of apoptosis by Annexin-V staining in shYTHDF2 HMECs with (blue) and without (red) 24 hours of MYC-induction. p*$<$0.05, p***$<$0.001, Bars are mean $\pm$ SD, n = 3 biological replicates, two-tailed Student's t-test.
(D) Quantification of necrotic cells by PI staining in shYTHDF2 HMECs with (blue) and without (red) MYC-induction. p*$<$0.05, p***$<$0.001. Bars are mean $\pm$ SD, n = 3 biological replicates, two-tailed Student's t-test.
(E) Annexin-V/ Propidium iodide staining and FACS analysis of shYTHDF2 HMECs with (blue) and without (red) 4 days of MYC-induction.
(F) Histograms of PI staining with (blue) and without (red) 4 days of MYC-induction. Gaussian curves represent cell cycle phase with quantification of cells in G1.
(G) Time-lapse microscopy 10X phase image well confluency acquired and analyzed by IncuCyte in shYTHDF2 cells compared with NTC in MDA-MB-231-LM2, MDA-MB-231, MCF-7 and SKBR3 cells. *p$<$0.05, **p$<$0.01, ***p$<$0.001, ****p$<$0.0001, two-way ANOVA test with Dunnett's post-hoc test for multiple comparisons. Values normalized to initial average confluence compared to NTC. Bars are mean $\pm$ SD, n = 6 independent replicates.
(H) Representative 10X phase images taken by IncuCyte for each condition in (G). Scale bar = 200 μm.

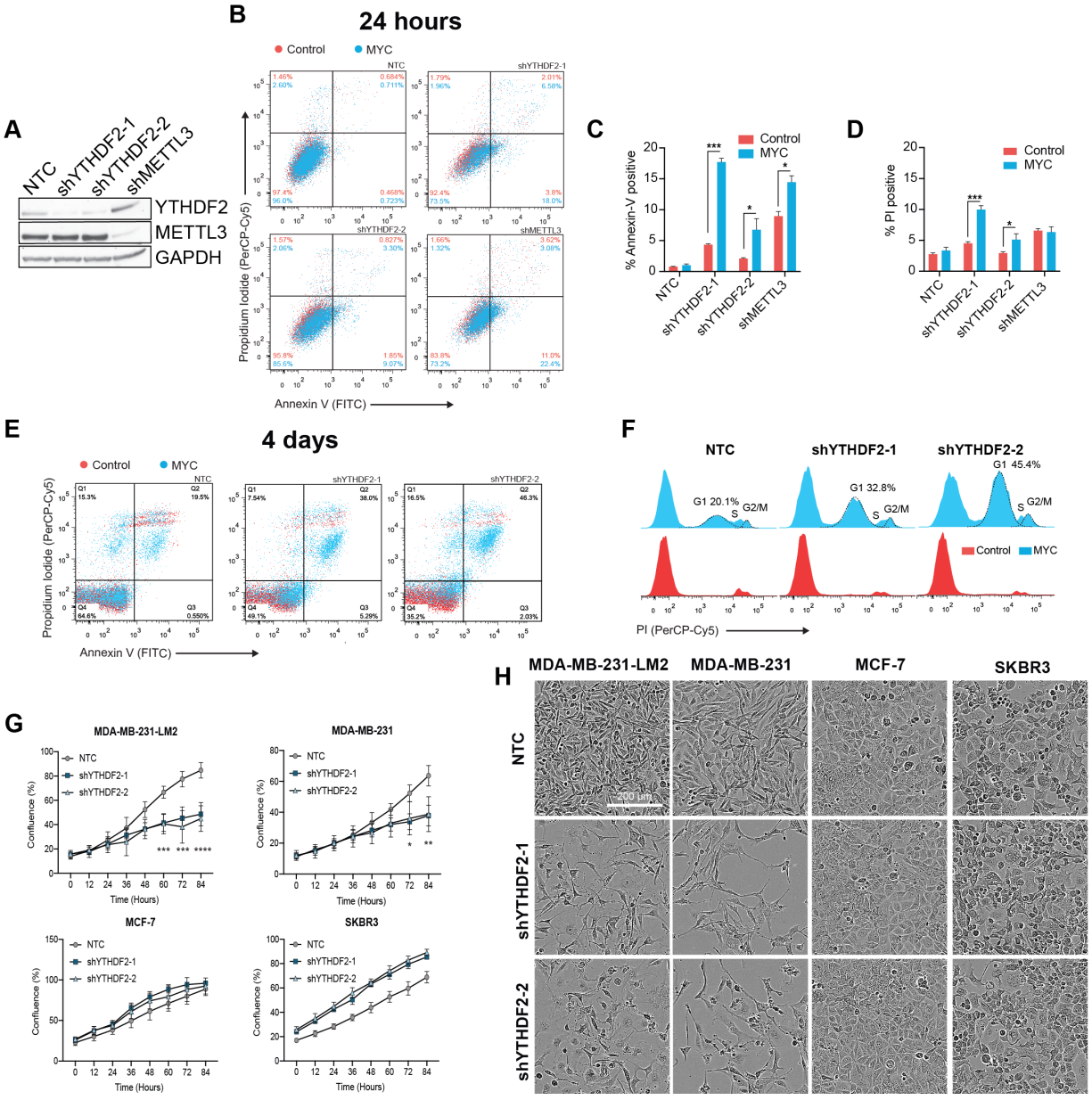
A
NTC
shYTHDF2-1
shYTHDF2-2
shMETTL3
YTHDF2
METTL3
GAPDH
B
24 hours
Control
MYC
NTC
shYTHDF2-1
shYTHDF2-2
shMETTL3
Propidium Iodide (PerCP-Cy5)
Annexin V (FITC)
C
% Annexin-V positive
Control
MYC
D
% PI positive
E
4 days
F
G1 20.1%
S
G2/M
G1 32.8%
G1 45.4%
PI (PerCP-Cy5)
G
MDA-MB-231-LM2
MDA-MB-231
MCF-7
SKBR3
Confluence (%)
Time (Hours)
H
200 μm

Figure 2.5: **Depletion of YTHDF2 in MYC-dependent cancer cells suppresses tumor growth *in vivo***.
(A) Schematic of pooled shRNA screen conducted in MDA-MB-231-LM2 cells *in vitro* and *in vivo*.
(B-D) Dot plots showing the normalized abundance of shRNA as quantified by NGS and analyzed by DESeq2 (Love et al., 2014) (median $\pm$ quartile) after doxycycline-inducible shRNA knockdown of MDA-MB-231-LM2 cells (B) in vitro (n = 4 biological replicates) and (C,D) *in vivo*. Each dot represents a tumor sample. T0 condition refers to initial time point of +DOX mice. -DOX=16 mice, +DOX=10 mice.
(E) Western blot analysis of cell lysates from cells cultured *in vitro* prior to xenograft injection. Cells were transduced with doxycycline (DOX)-inducible YTHDF2-targeting shRNA were treated with (+DOX) and without (-DOX) doxycycline for 7 days before analysis.
(F) Average tumor volume over time of xenografted mice expressing doxycycline inducible YTHDF2-targeting shRNA versus vehicle controls. p***$<$0.001, p****$<$0.0001, Bars are mean $\pm$ SEM, Two-way ANOVA. -DOX = 9 mice, +DOX = 6 mice.
(G) Images of subcutaneous xenografted nude mice 35 days after doxycycline induction (+DOX) of MDA-MB-231-LM2 cells expressing YTHDF2-targeting shRNA alongside vehicle control (-DOX). Scale bars = 1 cm.
(H) Tumor volume of xenografted mice 35 days after induction of MDA-MB-231-LM2 cells expressing doxycycline inducible YTHDF2-targeting shRNA versus vehicle controls. -DOX= 9 mice, +DOX = 6 mice. P-values were calculated by two-tailed Student's t-test.
(I) Immunohistochemical (IHC) analysis of doxycycline treated (+DOX) and untreated (-DOX) tumor sections after 35 days of treatment. Tumor sections were stained for hematoxylin and eosin (H/E) or hematoxylin and DAB for Ki67 proliferation marker and CD31 vascular endothelial cell marker. Sections are presented at 20x magnification. Scale bars = 100 μm.
(J) Western blot analysis of cell lysates from final tumors, 35 days after treatment for expression of cell death.
(K) RT-qPCR analysis of mRNA extracted from final tumors, 35 days after treatment for expression of human (tumor) and mouse (host) angiogenic markers relative to Gapdh. **p$<$0.01, n.s. = not significant, two-tailed Student's T-test. Bars are mean $\pm$ SEM, n = 9 vehicle mice, 6 DOX mice.

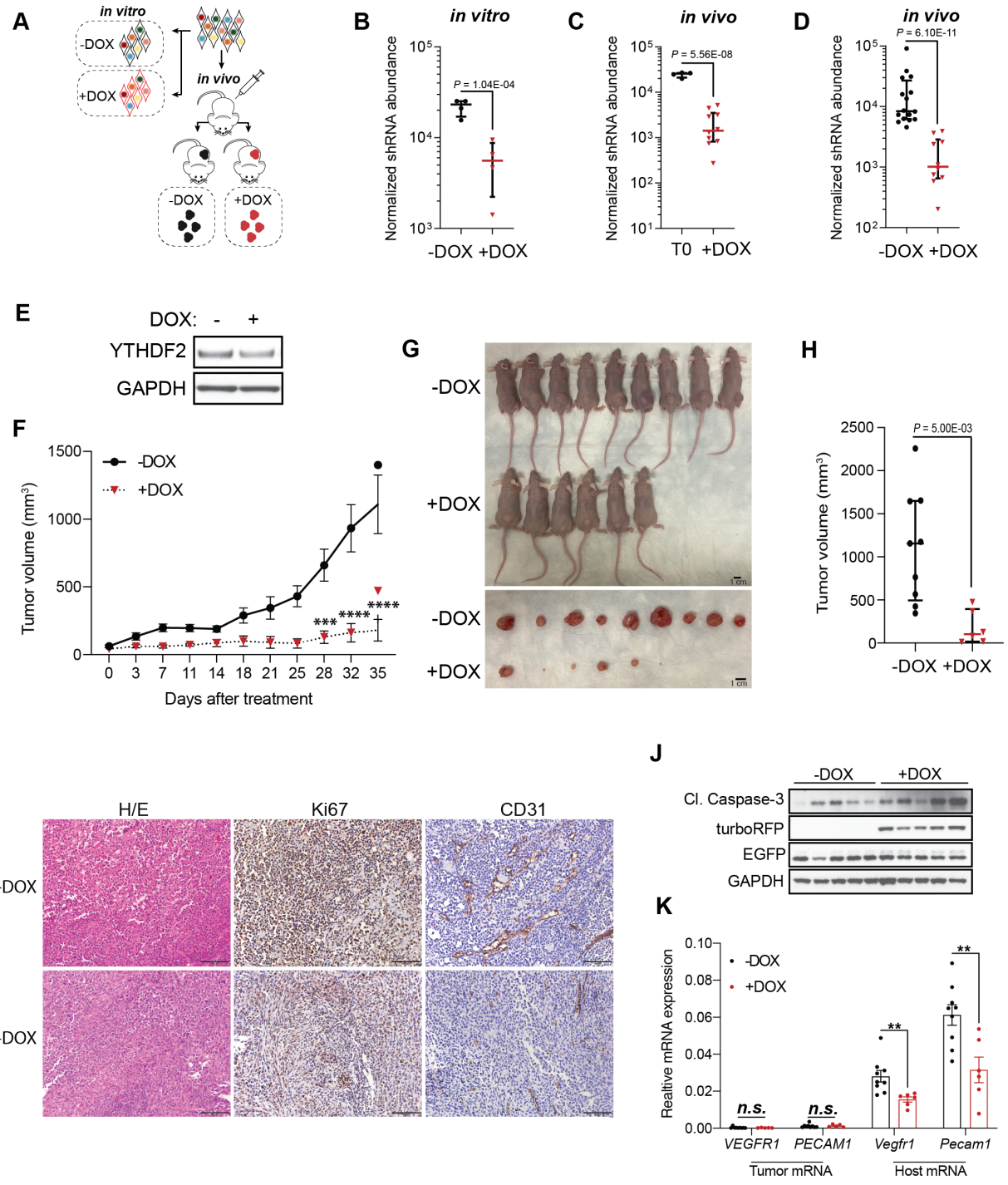
A
in vitro
-DOX
+DOX
in vivo
-DOX
+DOX
B
in vitro
Normalized shRNA abundance
P = 1.04E-04
-DOX +DOX
C
in vivo
Normalized shRNA abundance
P = 5.56E-08
T0 +DOX
D
in vivo
Normalized shRNA abundance
P = 6.10E-11
-DOX +DOX
E
DOX: - +
YTHDF2
GAPDH
F
Tumor volume (mm3)
-DOX
+DOX
***
****
****
Days after treatment
G
-DOX
+DOX
-DOX
+DOX
H
Tumor volume (mm3)
P = 5.00E-03
-DOX +DOX
I
H/E
Ki67
CD31
-DOX
+DOX
J
-DOX
+DOX
Cl. Caspase-3
turboRFP
EGFP
GAPDH
K
Realtive mRNA expression
-DOX
+DOX
n.s.
n.s.
**
**
VEGFR1
PECAM1
Vegfr1
Pecam1
Tumor mRNA
Host mRNA

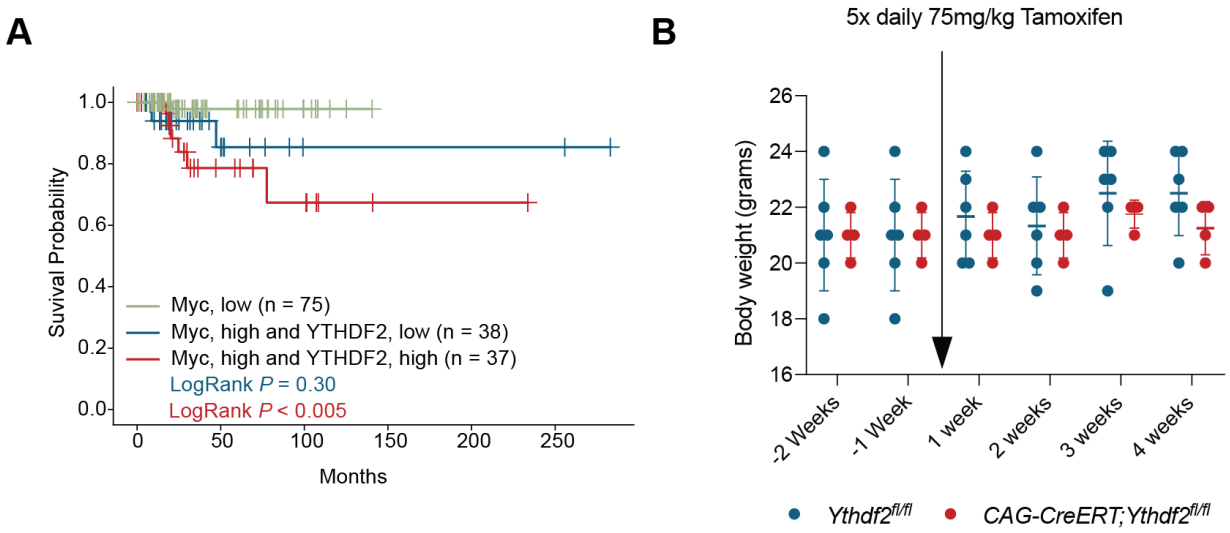

Figure 2.6: **Evaluation of the therapeutic potential for targeting YTHDF2 as therapy in patients with TNBC.**
(A) Kaplan-Meier survival analysis of basal-like tumors downloaded from the TCGA Data Portal (Liu et al., 2018). Curves represent survival probability of tumors with low *MYC* mRNA expression (green, n = 75), high *MYC* mRNA expression and low *YTHDF2* mRNA expression (blue, n = 38), and high *MYC* mRNA expression and high *YTHDF2* mRNA expression (red, n = 37). P-values calculated by LogRank significance compared to tumors with low *MYC* mRNA expression (green).
(B) Body weights of 4 male *CAG-CreERT;Ythdf2*$^{fl/fl}$ and 6 *Ythdf2*$^{fl/fl}$ littermates measured at 6 and 7 weeks and once weekly at weeks 9-12 following tamoxifen administration on week 8.

Table 2.1: Normalized abundance of YTHDF2 hairpins *in vitro* from pooled shRNA screen.

shRNA	V2LHS_115143	V2LHS_115142	V3LHS_381614
gene	YTHDF2	YTHDF2	YTHDF2
TB7053_01_vitro_unt_initial	15617	13054	15649
TB7053_02_vitro_unt_initial	21154	13778	10087
TB7053_03_vitro_unt_initial	25204	41190	14611
TB7053_04_vitro_unt_initial	25264	19629	6292
TB7053_05_vitro_dox_final	6516	16092	12132
TB7053_06_vitro_dox_final	9487	10024	12528
TB7053_07_vitro_dox_final	4666	15834	27222
TB7053_08_vitro_dox_final	1421	8590	17336
padj_dox_unt_vitro	0.000104	0.0683	0.184

Table 2.2: Normalized abundance of YTHDF2 hairpins *in vivo* from pooled shRNA xenograft screen.

shRNA	V2LHS_115143	V2LHS_115142	V3LHS_381614
gene	YTHDF2	YTHDF2	YTHDF2
TB7053_17_vivo_veh_final	13572	5902	10568
TB7053_18_vivo_veh_final	17153	4147	5684
TB7053_20_vivo_veh_final	91367	2032	7790
TB7053_26_vivo_veh_final	7395	16617	15461
TB7053_27_vivo_veh_final	8560	257138	2475
TB7053_28_vivo_veh_final	30076	6321	27500
TB7053_31_vivo_veh_final	8277	3029	1262
TB7053_32_vivo_veh_final	7342	2171	1402
TB7053_35_vivo_veh_final	4567	9422	16455
TB7053_38_vivo_veh_final	31304	6782	1274
TB7053_39_vivo_veh_final	6170	9501	1965
TB7053_40_vivo_veh_final	5976	1546	1839
TB7053_41_vivo_veh_final	6303	3327	1121
TB7053_43_vivo_veh_final	15960	10043	3953
TB7053_44_vivo_veh_final	38814	366906	5114
TB7053_46_vivo_veh_final	5551	4221	4399
TB7053_13_vivo_DOX_final	752	1087	4592
TB7053_14_vivo_DOX_final	931	2136	3731
TB7053_15_vivo_DOX_final	673	1917	5099
TB7053_16_vivo_DOX_final	2390	7645	2766
TB7053_21_vivo_DOX_final	3926	3163	2927
TB7053_22_vivo_DOX_final	3666	10135	6466
TB7053_23_vivo_DOX_final	2606	417	6619
TB7053_24_vivo_DOX_final	203	12851	4323
TB7053_45_vivo_DOX_final	586	9662	10822
TB7053_47_vivo_DOX_final	1097	3838	8864
padj_DOX_veh_vivo	6.1E-11	0.0000986	0.598

Chapter 3

Defining the RNA-binding function of YTHDF2 and the role of m^6A regulation in TNBC

3.1 Introduction

While it has been known for years that mRNAs undergo chemical modifications, the field of epitranscriptomics has exploded with discoveries over the past decade. Early advances included the discovery of the YTH domain-containing family proteins through the identification of 14 invariant and 19 other highly conserved residues that make up the unique, single-stranded RNA-binding YTH domain (Z. Zhang et al., 2010). This family of proteins is ubiquitously expressed and is well-conserved across eukaryotic species, however, of the three DF proteins, YTHDF2 has the highest binding affinity for m^6A-methylated RNAs (X. Wang et al., 2014; Z.

Zhang et al., 2010). m^6A deposition is known to naturally occur in both long-internal exons and the 3' untranslated region (UTR), recruiting YTHDF2 to the terminal end of the transcript. This suggests a role for m^6A in accelerating deadenylation in cells since polyadenylation (poly(A)) tail shortening is the first step in mRNA decay (Du et al., 2016). Moreover, YTHDF2 was identified to mediate mRNA turnover by recruiting the CCR4-NOT deadenylase complex to initiate deadenylation and decay of m^6A-containing transcripts (Du et al., 2016; X. Wang et al., 2014). It was later confirmed that YTHDF2 localizes with its bound targets to processing (P) bodies for committed degradation (Ries et al., 2019; X. Wang et al., 2014).

Several early clinical studies reported that cancer patients often experience elevated levels of modified nucleoside in their urine, indicating increased cellular RNA turnover in tumor cell populations (Marvel et al., 1994). In addition to a profound increase in total transcript abundance from amplified MYC activity, many RNAs in cancer cells often undergo 3'UTR shortening through alternative polyadenylation which prevents miRNA-mediated repression of the transcript (Mayr & Bartel, 2009). As a result, the shorter transcripts have greater stability and produce substantially more protein, causing cancer cells to rely more heavily on RNA decay pathways to maintain endoplasmic reticulum (ER) homeostasis in proliferating cells (Mayr & Bartel, 2009). In MYC-dependent cancer cells these mechanisms can be synergistic. For example, the short isoform of IMP1 greatly promotes cancer cell transformation by stabilizing the *MYC* transcript (Mayr et al., 2009). Therefore, identification of YTHDF2 target transcripts that are subject to m^6A-mediated mRNA degradation in MYC-dependent cancer is critical for expanding the understanding of genes and signaling pathways underlying oncogenic support processes. While several studies have attempted to describe the role of YTHDF2-mediated turnover of m^6A-RNA in cancer, it remains unclear due to conflicting findings regarding its function (Paris et al., 2019;

Zhong et al., 2019).

Here, we employ eCLIP-seq, m^{6}A-seq, and RNA-seq to identify direct endogenous YTHDF2 mRNA targets in several MYC-dependent and MYC-independent cancer cell lines. While YTHDF2 targets have been identified before using similar methods, targets have not yet been identified with endogenous antibodies. As with all RBPs, there is a lingering concern that overexpression does not accurately recapitulate endogenous binding. Further, it has recently been shown that heterologous expression of YTHDF2 causes spontaneous aggregation in cells which may indicate non-specific binding (Zaccara et al., 2020). In this chapter, we define the direct and functionally relevant YTHDF2 target RNAs in human breast cancer and specifically identify a subset of targets that are differentially bound in MYC-dependent cancer, defining the pathway that is actively downregulated by YTHDF2 to maintain cellular homeostasis.

3.2 Results

3.2.1 Identification of YTHDF2 binding sites

To identify the transcript-specific function of YTHDF2 targets in MYC-dependent cancer, we performed enhanced crosslinking and immunoprecipitation followed by deep sequencing (eCLIP-seq) (Van Nostrand et al., 2017) in induced and control MYC-ER HMECs, MDA-MB-231-LM2 cells, MDA-MB-231 cells, MCF-7 cells and SKBR3 cells in biological duplicate. YTHDF2-RNA complexes were immunoprecipitated (**Figure 3.1A**) and size-selected on nitrocellulose membranes before preparing libraries from the protected RNA fragments alongside size-matched inputs (SMInput). Libraries were sequenced to $\sim$20 million reads, of which on average $\sim$63% uniquely mapped to the genome, and on average $\sim$87% of the uniquely mapped

reads were usable after removing PCR duplicates (**Table A.1**) (Van Nostrand et al., 2017). Reproducible peaks with significant enrichment over SMInput were identified using irreproducible discovery rate (IDR) and peaks were annotated by gene and region.

To confirm overlap of YTHDF2 binding sites with m^{6}A modified sites, we performed m^{6}A sequencing (m^{6}A-seq) on the same cell lines in biological duplicates (Dominissini et al., 2013). Briefly, we extracted RNA from wild-type cell lines, sheared the RNA, immunoprecipitated RNA fragments with m^{6}A modifications and prepared libraries for sequencing. We sequenced the libraries to $\sim$20 million reads, of which on average $\sim$50% uniquely mapped to the genome, and on average $\sim$89% of uniquely mapped reads were usable (**Table A.2**). We called peaks using MACS2 (v2.1.2) (Y. Zhang et al., 2008). In agreement with previous YTHDF2 CLIP and RIP-seq experiments, we found that a majority of YTHDF2 and m^{6}A peaks occur in the coding sequence (CDS) and 3'UTR (**Figure 3.1B**) and contain the DRACH (D=A, G or U; R=A or G; H=A, C, or U) sequence motif (**Figure 3.1C**). To confirm that YTHDF2 generally binds m^{6}A modified sites, we overlapped metagene profiles and verified recruitment of YTHDF2 to m^{6}A sites at the 3' end of the transcript near stop codons where m^{6}A modifications are typically enriched (Meyer et al., 2012) (**Figure 3.2A-3.2B)**. In addition, we found that YTHDF2 eCLIP libraries were enriched over SMinput controls at the center of m^{6}A sites and vice versa, further confirming association of YTHDF2 with m^{6}A modified transcripts (**Figure 3.2C**). To determine if MYC activity influences the m^{6}A landscape in cancer we compared m^{6}A modified transcripts by overlapping peaks and genes among MYC-induced and uninduced HMECs (**Figure 3.2D, left**) and we found that fewer than 3% of m^{6}A peaks coincide with YTHDF2 peaks, many YTHDF2 binding sites were shared among MYC-induced and control HMECs and there were not obvious increases in total m^{6}A levels with MYC-induction (**Figure 3.2D, center, right**). Collectively,

our epitranscriptomic analyses confirm considerable overlap of YTHDF2 binding sites with m^{6}A modified sites in sequences containing similar consensus RNA motifs.

3.2.2 Overall m^{6}A levels are associated with metastatic potential

Interestingly, we found that the secondary lung metastatic MDA-MB-231-LM2 tumor cells appeared to acquire new m^{6}A modifications since 72% of m^{6}A sites were unique from the parental MDA-MB-231 tumor cell line from which they originated (**Figure 3.3**). This suggests that the m^{6}A landscape of tumor cells is modified during tumor evolution and metastasis, and is consistent with previous studies indicating that cancer cells become increasingly reliant on m^{6}A-dependent RNA regulation as they become more invasive (Lin et al., 2016). However, MYC-independent tumor cell lines did not display robust differences in m^{6}A modified sites compared to MDA-MB-231 cells other than what might be attributed to target expression level variances, further supporting our observation that MYC activity does not determine the m^{6}A landscape in mammary tumors (**Figure 3.3**).

3.2.3 YTHDF2 regulates ERK/MAPK signaling pathway targets in MYC-dependent cancer

Since RBP binding affinity is driven largely by RNA secondary structure and consensus binding motifs, which are conserved across cell types and states (Lambert et al., 2014), we expect that differences in YTHDF2 binding targets among cancer cell lines are a result of differences in target RNA expression level and alterations in m^{6}A status. Therefore, we analyzed RNA expression data in cancer cell lines for YTHDF2 targets that were prominent in eCLIP binding data in both MYC-dependent cell lines (**Figure 3.4A**). Using hierarchical clustering of

z-scores, we identified two clusters (red and blue) where YTHDF2 targets are highly expressed in MYC-dependent cells compared to MYC-independent cells (**Figure 3.4B**). These clusters are highly enriched for genes that regulate wound healing, cell adhesion, ERK1/2 signaling, and epithelial-to-mesenchymal transition (EMT), while clusters including genes that are also highly expressed in MCF-7 cells (yellow and green) generally lack enrichment for these ontologies (**Figure 3.4C**).

3.2.4 Depletion of YTHDF2 upregulates EMT signaling in MYC-dependent cell lines

EMT is a key step in cancer cell metastasis where cells go through morphological changes to escape the basement membrane and invade blood vessels before they recolonize in a secondary organ (R. Y. Huang et al., 2012). Since YTHDF2 targets that were exclusively expressed in MYC-dependent cancer cells were involved in growth signaling and EMT pathways, we next verified that MYC-dependent cells underwent expression changes resembling EMT when YTHDF2 is depleted. To do so, we depleted YTHDF2 in MYC-induced HMECs and performed RNA sequencing (RNA-seq) in biological duplicate, to confirm upregulation of transcripts that contain coinciding YTHDF2 and m^6A peaks compared to transcripts lacking binding sites (**Figure 3.5A**). However, inspection of the individual upregulated mRNAs revealed that $>$50% of upregulated transcripts were not direct YTHDF2 targets. These include *CPA4*, *HMOX1*, and *MMP3*, which are known to contribute to or are transcribed in response to cell migration, wound healing, and metastatic phenotypes (Handa et al., 2019; X. Zhu et al., 2017; Y. Zhu et al., 2019) (**Figure 3.5B**). These genes exhibited very low or undetectable RNA expression (transcripts per million (TPM) $\leq$ 1) in NTC cells yet were dramatically increased ($\sim$30-85 TPM) in shYTHDF2

cells. We next interrogated the pathways represented among the upregulated mRNAs in MYC induced HMECs using gene ontology (GO) enrichment analysis of shYTHDF2 cells compared to NTC (Bonferroni adjusted p-value (padj) ≤ 0.001, $\log_2$FoldChange ≥ 1) (**Figure 3.5C**). 4.8% of expressed genes were differentially upregulated in shYTHDF2 cells compared to NTC and were enriched for ontologies associated with apoptosis, including inflammatory response and negative regulation of proliferation. In addition, transcripts upregulated in shYTHDF2 cells were enriched for ontologies associated with mesenchymal cell transition (i.e. tissue morphogenesis, TGF-β receptor signaling and signaling responses to growth factor stimuli) while downregulated transcripts were enriched for pathways associated with epithelial cell processes (i.e. adhesion and junction organization, keratinization, and epidermis development) (**Figure 3.5C**). We also identified 1.2% (padj ≤ 0.001, $\log_2$FoldChange ≥ 1) of expressed genes were differentially upregulated in YTHDF2 depleted, MYC induced cells compared to YTHDF2 depleted, uninduced HMECs, revealing that activation of MYC selectively upregulates inflammatory response and stress induced genes (**Figure 3.5D**). This analysis confirms our hypothesis that YTHDF2 depletion encourages EMT signaling in MYC-dependent cancer cells.

3.2.5 Molecular validation of EMT signaling in YTHDF2 depleted cells

EMT is executed by several TFs including SNAIL and is known to induce expression of MAPK/ERK in response to TGF-β, Notch, and BMP signaling (I. H. Chen et al., 2013; Vincent et al., 2009; Xie et al., 2004). Several upstream regulators of these pathways are YTHDF2 targets (**Figure 3.6A**) and YTHDF2 depletion resulted in upregulation of *SNAIL* protein synthesis (**Figure 3.6B**). Since EMT entails profound phenotypic changes in cells, specifically promoting the spindle-shape of mesenchymal cells while discouraging cellular polarization (R. Y. Huang

et al., 2012), we confirmed activation of EMT signaling by studying cell morphologies following YTHDF2 depletion. We observed branched cell morphology with high levels of Vimentin localized to cell projections in YTHDF2-depleted cells (**Figure 3.6C**). Since overexpression of MYC has been shown to drive EMT (Yin et al., 2017), we overlapped our eCLIP-seq and RNA-seq data with publicly available MYC chromatin immunoprecipitation sequencing (ChIP-seq) data (ENCODE; ENCSR000DOS) to identify if YTHDF2 functionally regulates MYC's target transcripts. Although MYC targets are significantly upregulated in YTHDF2 depleted MYC-induced HMECs (**Figure 3.6D**), very few significantly upregulated MYC targets were bound by YTHDF2, suggesting that YTHDF2 regulates pathways upstream of MYC (**Figure 3.6E**). Congruently, we detected upregulated ERK1/2 expression and increased expression of cap-dependent translation initiation factors prompting increased MYC protein synthesis in YTHDF2 depleted, MYC-dependent cells compared with NTC (**Figure 3.6F**). Thus, we conclude that YTHDF2 limits the activation of signaling pathways operating upstream of MYC by facilitating the degradation of growth factor and receptor mRNAs that aggressively upregulate MAPK/ERK signaling, cap-dependent translation and transcription of EMT genes.

3.3 Discussion

Recent studies have identified roles for m^6A methylation as an important regulatory mechanism to modulate the expression of gene networks that preserve cellular homeostasis during several types of stress responses. m^6A effectors play important roles in controlling stem cell fate regulation, suggesting that alterations in m^6A levels affect the activation of differentiation pathways downstream of growth factors and morphogens and may also play related roles in cancer (Geula et al., 2015; M. Li et al., 2018; Z. Li et al., 2018). In our studies, we found

an increase in m^{6}A modified sites throughout the transcriptome in secondary, metastatic cancer cells compared to cells derived from the primary tumor, which independently supports the finding that deposition of m^{6}A on RNA by METTL3 promotes cancer cell growth, survival and invasion (Lin et al., 2016). In particular, YTHDF2 has been shown to play a key role in regulating cellular homeostasis by facilitating m^{6}A-mRNA localization to specific subcellular compartments (Ries et al., 2019) and translational control (J. Zhou et al., 2015) in response to various cellular stressors. Cancer cell transformation requires adaptation to chronic stress conditions such as hypoxia, inflammation, nutrient and oxidative stress; therefore, our observation that invasive tumor cells acquire new m^{6}A modifications raises the possibility that m^{6}A-binding proteins such as YTHDF2 enable survival during such conditions.

YTHDF2 has been shown to orchestrate the “migration-proliferation dichotomy” by promoting proliferation while inhibiting migration and invasion in response to growth factor signaling (J. Chen et al., 2017; Giese et al., 1996). To clarify this role, we profiled the binding of YTHDF2 across m^{6}A modified sites and identified specific, endogenous target RNAs in MYC-dependent and MYC-independent cancer cell lines by eCLIP-seq and m^{6}A-seq to distinguish the direct pathways that are activated during YTHDF2 depletion. Our analyses selectively pointed to targets regulating MAPK/ERK signaling, encompassing several mRNAs encoding upstream activating growth factor and receptor families including TGFβ, BMP, EGF, and TNF. Stabilization of these target mRNAs lead to global upregulation of cellular protein markers of SNAIL signaling, branching morphogenesis, and cap-dependent translation in YTHDF2 depleted cells and were accompanied by a marked reduction in proliferation. Our data supports a role for YTHDF2 in maintaining the “migration-proliferation dichotomy”, whereby depletion of YTHDF2 induces active migration while suppressing cell proliferation, but additionally provides new mechanistic

insight by identifying the stabilized transcripts driving this phenotype.

3.4 Materials and Methods

3.4.1 Cell Culture

Immortalized human cell lines were used in this study. HEK293xT, MDA-MB-231, MDA-MB-231-LM2, and MCF-7 cells were cultured in DMEM supplemented with 10% fetal bovine serum. SKBR3 cells were cultured in McCoy's 5A Medium supplemented with 10% fetal bovine serum. Cells were passaged every 3 or 4 days with TrypLE EXPRESS (Life Technologies) using standard methods. MYC-ER HMECs were cultured in Medium 171 supplemented with MEGS (Life Technologies). Cells were passaged every 3 or 4 days with TrypLE EXPRESS and Defined Trypsin inhibitor. Cells were maintained in a humidified incubator at 37°C with 5% CO_2.

3.4.2 Knockdown experiments

Cells were transduced with TRC lentiviral shRNA vector non-targeting control (NTC; Millipore Sigma; SHC002), and TRC lentiviral shRNA vector YTHDF2 (shYTHDF2-1; Millipore Sigma; TRCN0000168751), (shYTHDF2-2; Millipore Sigma; TRCN0000167813) for 24 hours before treatment with Puromycin (2 mg/mL). Cells were analyzed 6 days after the addition of lentivirus for all assays.

3.4.3 Immunofluorescence

Cells were seeded on poly-D-lysine hydrobromide (PDL) (Millipore Sigma; P6407) coated 8-well chamber slides (Millipore Sigma). Cells were fixed in 4% paraformaldehyde in PBS, permeabilized and blocked 5% normal goat serum, 0.1% Triton-X in PBS for 1 hour at RT. Primary antibody: Rabbit mAb anti-Vimentin (Cell Signaling; 5741) was diluted in blocking

buffer and incubated overnight at 4°C. Cells were washed 3 times in 0.1% Triton-X in PBS and incubated with secondary antibody: Goat anti-Rabbit IgG Alexa Fluor 488 (Invitrogen; A32731) for 1 hour at RT, followed by 3 washes and coverslip mounting with Prolong Diamond Antifade Mountant with DAPI (Thermofisher). Slides were imaged on a ZEISS Axio Vert.A1 inverted microscope.

3.4.4 eCLIP-seq library preparation and analysis

Experiments were performed as previously described in Van Nostrand et al., 2017 in biological duplicates. Briefly, 20M cells were UV-crosslinked at 400 mJ/cm^2 constant energy, lysed in eCLIP lysis buffer on ice, and sonicated by BioRuptor. Lysates were treated with RNase I to fragment RNA, then protein-RNA complexes were immunoprecipitated (Sheep anti-rabbit Dynabeads) with a YTHDF2 antibody: Rabbit pAb anti-YTHDF2 (Aviva; ARP67917_P050). Inputs (2% of lysate) were saved and run alongside IP samples. IP samples were stringently washed, and for all samples the RNA was dephosphorylated with FastAP (NEB) and T4 PNK (NEB), followed by on-bead ligation of barcoded RNA adapters to the 3' end (T4 RNA Ligase, NEB). RNA-protein complexes were run on standard protein gels and transferred to nitrocellulose membranes where the RNA in the region 65 kDa – 140kDa was excised off the membrane and proteinase K (NEB) treated. RNA was then reverse transcribed with Superscript III (Thermofisher) followed by treatment with ExoSAP-IT (Affymetrix) to remove excess oligonucleotides. Samples were cleaned up with Dynabeads MyOne Silane (Thermofisher) and subject to qPCR to determine the appropriate number of PCR cycles. Libraries were amplified with Q5 PCR mix (NEB), QCed using an Agilent D1000 Screen Tape (Agilent Technologies) and sequenced to 20M reads on the HiSeq4000 in single-end 75 bp mode.

Fastq files were run through eCLIP-v0.4.0 pipeline as previously described in Van Nostrand et al., 2017. Briefly, adapters and adapter-dimers were trimmed with cutadapt-v1.14.0, reads were mapped to repeat elements and filtered with STAR-v2.4.0, PCR duplicates were removed with umi_tools-v0.5.5, and enriched peak regions were called with CLIPPER-v1.2.2v. Peaks were input normalized, reproducible peaks were determined by irreproducible discovery rate (IDR) (`https://github.com/YeoLab/merge_peaks`), and peaks were filtered by $\log_2$(fold change) ≥ 3 and -$\log_{10}$(p-value) ≥ 3 using merge_peaks-v0.0.5. Peaks were annotated by gene and region. Motifs were analyzed using HOMER-v.4.9.1 (Heinz et al., 2010). Metagene plots were generated using MetaPlotR-v2.1.2 (Olarerin-George & Jaffrey, 2017).

3.4.5 m^{6}A-seq library preparation and analysis

Experiments were performed as previously described in Dominissini et al., 2013 in biological duplicates. Briefly, 250 μg RNA was extracted using Trizol Reagent (Invitrogen) according to manufacturer's instructions, rRNA depleted (RiboZero), and fragmented to $\sim$100 nt. 1 μg fragmented RNA was saved as input and the rest was immunoprecipitated (Protein G sheep anti-mouse Dynabeads) with an m^{6}A antibody: Mouse mAb anti-m^{6}A (Synaptic Systems; 202 011). RNA was precipitated and libraries were prepared with TruSeq Stranded Total RNA Preparation Kit according to manufacturer's instructions. Libraries were QCed using an Agilent D1000 Screen Tape (Agilent Technologies). Libraries were sequenced to $\sim$20M reads on the HiSeq4000 on single-end 75 bp mode. Reads were subjected to cutadapt (Martin, 2011) to remove polyA tracts and adapter sequences, followed by removal of duplicates and alignment to the human genome build hg19 using the STAR-v2.4.0 (Dobin et al., 2013). Uniquely mapped reads were subjected to peak-calling analysis using MACS2-v2.1.2 software (Y. Zhang et al.,

2008) with the following parameters:

macs2 callpeak -t IP.sam -c Input.sam -f SAM –gsize='3137161264' –tsize=50 –nomodel –extsize=50 -q 0.1 –down-sample

Peaks were filtered based by -$\log_{10}$(q-value)$\geq$3 and motifs were analyzed using HOMER-v.4.9.1 (Heinz et al., 2010). Metagene plots were generated using MetaPlotR-v2.1.2 (Olarerin-George & Jaffrey, 2017).

3.4.6 RNA-seq library preparation and analysis

RNA was extracted with Direct-zol RNA Miniprep kit (Zymo Research; R2071) for two independent non-targeting control biological replicates and two independent shYTHDF2 biological replicates in MYC-ER HMECs induced with 15 nM 4-OHT for 48 hours. 1 μg total RNA was rRNA depleted (RiboZero) and processed using the TruSeq Stranded Total RNA Preparation Kit (Illumina; RS-122-2201) according to manufacturer's instructions. Libraries were QCed using an Agilent D1000 Screen Tape (Agilent Technologies). Libraries sequenced to $\sim$20M reads on the HiSeq4000 in single-end 75 bp mode.

Adapters were trimmed and reads were mapped to the human genome build hg19 using STAR-v2.4.0. Differential expression was analyzed using DEseq2-v1.22.1 (with significance cutoffs of p $\leq$ 0.001 and $\log_2$(fold change) $\geq$ 1, with a minimum TPM of 1 in any sample).

3.4.7 Western Blot

Cells were lysed with cold RIPA buffer (Thermofisher) with 200X Protease inhibitor and 100X phosphatase inhibitor. Protein was quantified using Peirce BCA Protein Assay Kit. Total protein extracts were run on 4%-12% NuPAGE Bis-Tris gels in NuPAGE MOPs running

buffer (Thermofisher) and transferred to PVDF membranes. Membranes were blocked in 5% nonfat milk in TBST for 1 hour, incubated overnight at 4°C with the following primary antibodies (5% BSA for phospho-antibodies): Rabbit pAb anti-YTHDF2 (Proteintech; 24744-1-AP), Rabbit pAb anti-Phopho-p44/42 MAPK (Erk1/2) (Cell Signaling; 4370), Rabbit pAb anti-p44/42 MAPK (Erk1/2) (Cell Signaling; 4695), Rabbit mAb anti-eif4e (Cell Signaling; 9742), Rabbit pAb anti-eif2α (Cell Signaling; 9722), Rabbit mAb anti-c-Myc (Cell Signaling; 13987), Mouse mAb anti-GAPDH (Abcam; ab8245), Rabbit mAb anti-BiP (Cell Signaling; 3177), Rabbit mAb anti-Phospho-p38 MAPK (Cell Signaling; 4511), Rabbit mAb anti-p38 MAPK (Cell Signaling; 8690), Rabbit mAb anti-Cleaved Caspase-3 (Cell Signaling; 9664), Rabbit mAb anti-Phospho-SAPK/JNK (Cell Signaling; 4668), Rabbit pAb anti-SAPK/JNK (Cell Signaling; 9252), Rabbit pAb anti-IRE1α (Novus Biologicals; NB100-2324), Rabbit pAb anti-Phospho-IRE1α (Novus Biologicals; NB100-2323), Rabbit mAb anti-Snail (Cell Signaling; 3879), washed 3X for 5 minutes with TBST, incubated for 1 hour at RT in 5% nonfat milk in TBST with secondary HRP-conjugated antibody: Goat anti-Mouse IgG Secondary Antibody, HRP (Invitrogen; 31430), Goat anti-Rabbit IgG Secondary Antibody, HRP (Invitrogen; 31460) at 1:5000 dilution, and washed 3X for 5 minutes with TBST. Membranes were developed using Thermo Pierce ECL detection reagents.

3.4.8 Gene Ontology (GO) Analysis

GO analyses were conducted using the GOrilla tool (Eden et al., 2009). Expressed gene sets with TPM $>$ 1 for each respective cell lines were used as background lists. GO terms were ranked by Bonferroni-corrected hypergeometric p-values.

3.5 Acknowledgements

We would like to thank the Sanford Consortium Human Embryonic Stem Cell Core for allowing use of their instruments (BD Influx Cell Sorter, X-20 Fortessa, BioRad CFX 384, Incucyte (1S10OD025060), and Zeiss AxioImager). J.M.E is supported by the Ruth. L. Kirschstein F31 National Research Service Award (F31 CA217173) and Cancer Systems Biology Training Program (P50 GM085764 and U54 CA209891). Data used in this publication were generated by the Clinical Proteomic Tumor Analysis Consortium (NCI/NIH).

Chapter 3, in full, is a reprint of material as it will appear in: **Einstein JM**, Perelis M, Chaim IA, Meena JK, Nussbacher JK, Tankka AT, Yee BA, Li H, Madrigal AA, Neill NJ, Shankar A, Tyagi S, Westbrook TF, Yeo GW. Inhibition of YTHDF2 triggers proteotoxic cell death in MYC-dependent cancer. *In preparation*. The dissertation author is the primary author of this paper.

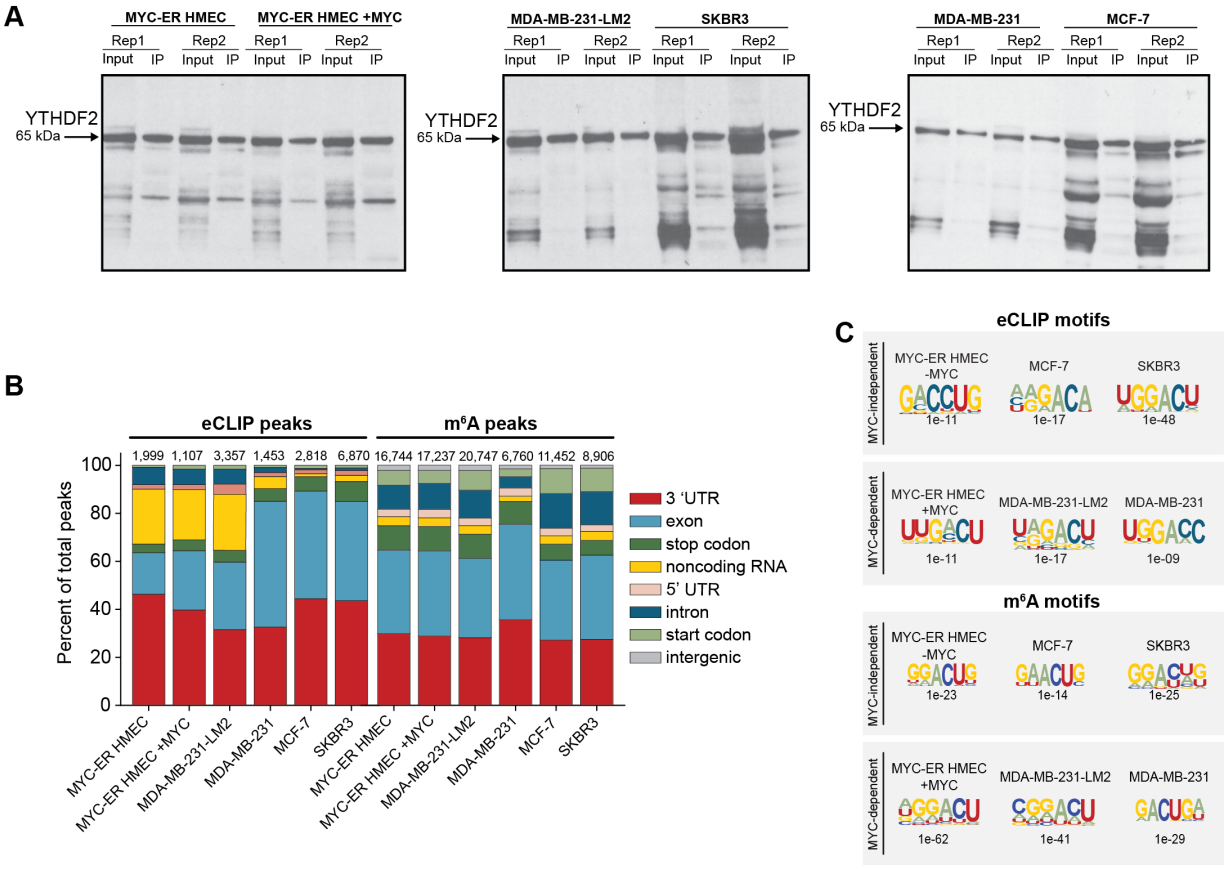

Figure 3.1: **eCLIP-seq and m^{6}A-seq identify peaks enriched for the DRACH RNA motif in 3'UTR and CDS regions.**

(A) Immunoprecipitation followed by western blot of YTHDF2 in eCLIP-seq samples.

(B) Stacked bar plot describing the region distribution for eCLIP or m^{6}A peaks as indicated. Total peak numbers per cell line are noted at the top of each bar. Each bar is representative of 2 biological replicates.

(C) Motif analysis of eCLIP-seq or m^{6}A-seq data, as indicated, with p-values generated by HOMER (Heinz et al., 2010) on filtered peaks. Representative of 2 biological replicates.

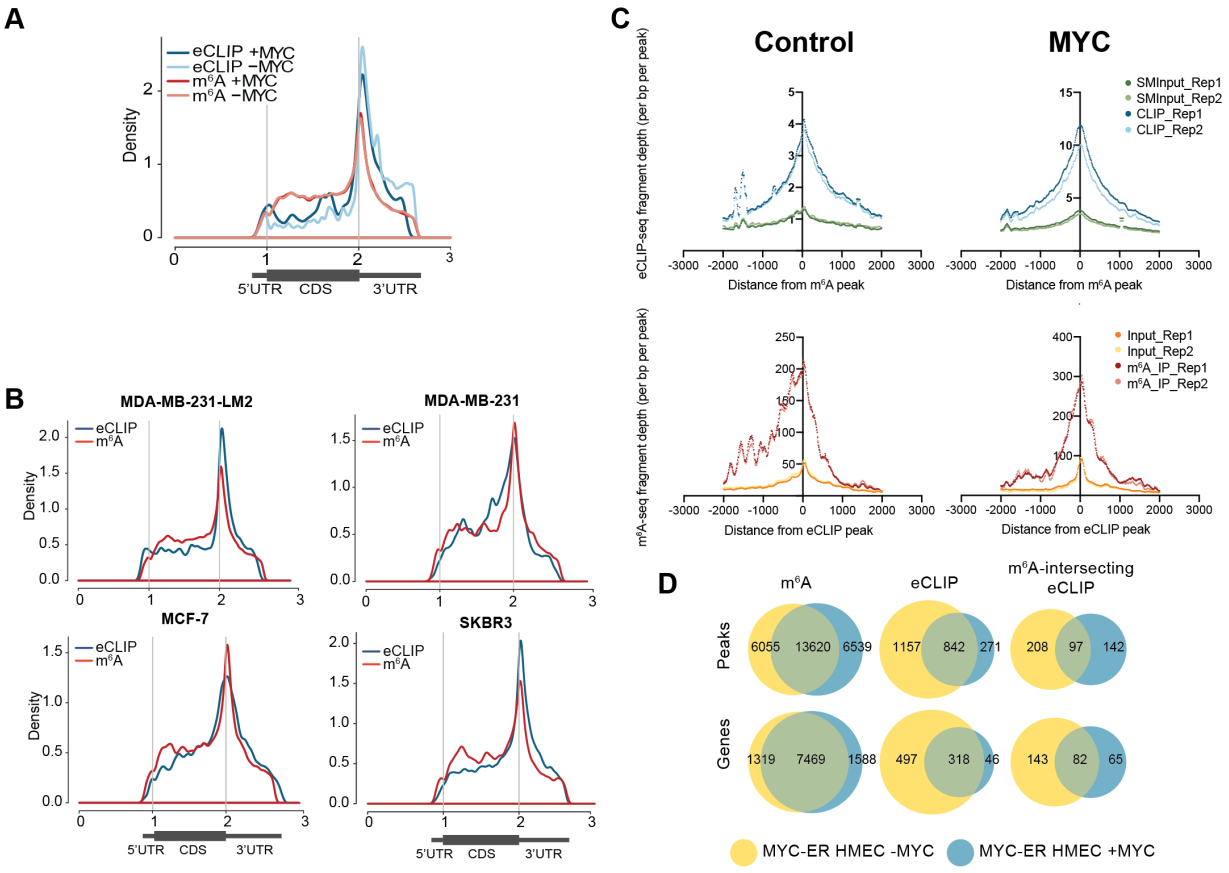

Figure 3.2: **YTHDF2 eCLIP-seq and m^{6}A-seq produce comparable binding profiles in all breast cancer cell lines.**

(A) Metagene profiles of eCLIP-seq and m^{6}A-seq peak enrichment depicting comparable YTHDF2 binding and m^{6}A methylation profiles in MYC-induced HMECs compared with control. Plotted using MetaPlotR (Olarerin-George & Jaffrey, 2017).

(B) Metagene profiles of eCLIP-seq and m^{6}A-seq data depicting comparable YTHDF2 binding and m^{6}A methylation profiles in MDA-MB-231-LM2, MDA-MB-231, MCF-7 and SKBR3 cells. Plotted using MetaPlotR (Olarerin-George & Jaffrey, 2017).

(C) Histograms displaying the eCLIP sequencing library densities relative to significant m^{6}A peaks identified by m^{6}A-seq and vice versa in the MYC-induced and uninduced HMECs. Library coverages were determined by HOMER (Heinz et al., 2010).

(D) Overlap of peak and gene enrichment between MYC-induced and control HMECs for m^{6}A-seq targets (left), eCLIP-seq targets (center), and m^{6}A-intersecting eCLIP-seq targets (right).

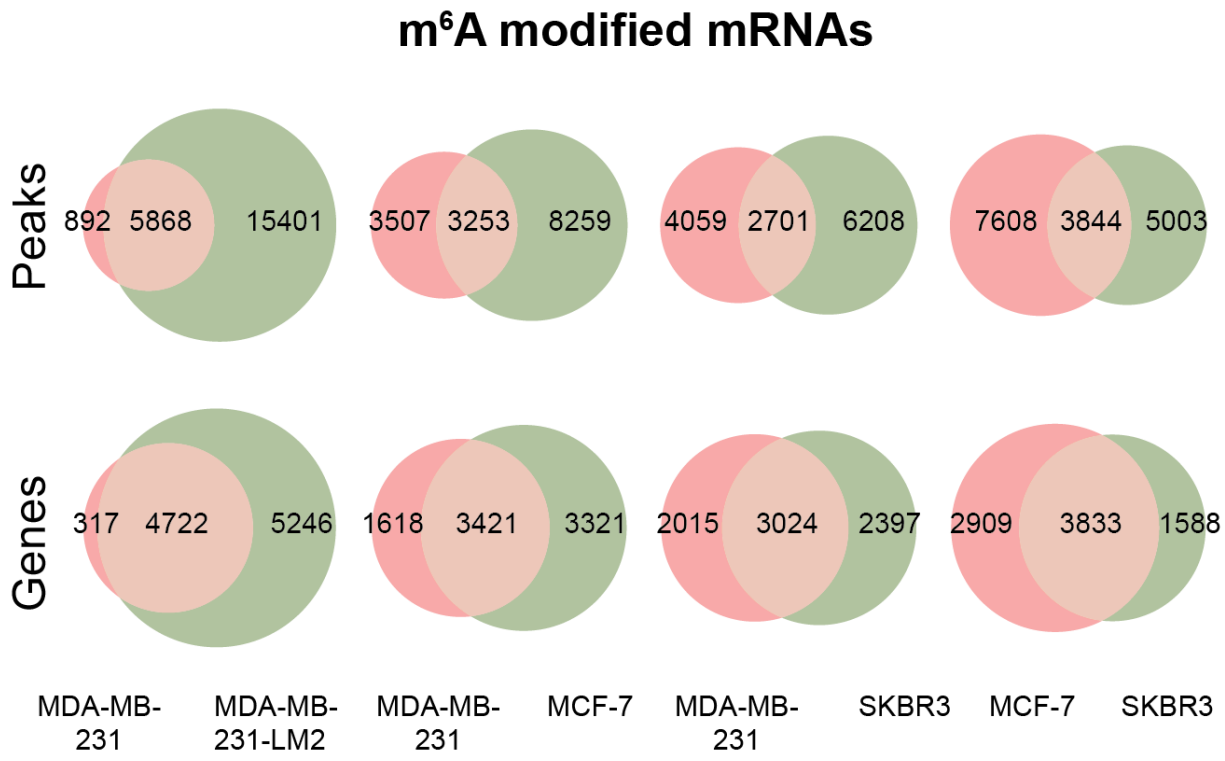

Figure 3.3: **Breast cancer cells gain m^{6}A modifications during cancer progression.** Venn diagram overlaps of m^{6}A-seq peak and gene enrichment among MYC-dependent and MYC-independent cell lines. MDA-MB-231 primary TNBC cells are compared to their secondary, metastatic LM2 cell line and to MYC-independent breast cancer cell lines.

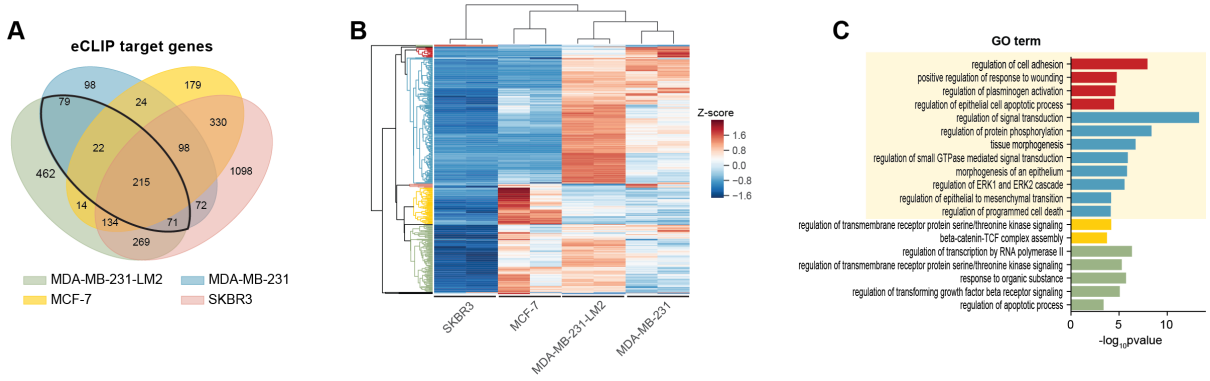

Figure 3.4: **eCLIP identifies YTHDF2 targets are enriched for MAPK/ERK pathway transcripts that are regulated exclusively in MYC-dependent cancer.**
(A) Four-way Venn diagram of overlapping YTHDF2 target genes among MYC-dependent and MYC-independent breast cancer cell lines. Genes overlapping in MDA-MB-231-LM2 cells and MDA-MB-231 cells are indicated by the black outline.
(B) Hierarchical cluster map illustrating expression levels of YTHDF2 target genes that are overlapping between MDA-MB-231-LM2 cells and MDA-MB-231 cells indicated in (A). Clusters are depicted in the dendrogram on the left.
(C) Gene ontology (GO) enrichment of genes in dendrogram clusters from (B).

Figure 3.5: **Gene expression analyses reveal stress and tissue morphogenic pathways are upregulated in response to YTHDF2 depletion in MYC-induced cells.**
(A) Cumulative distribution of the fold change in mRNA expression of shYTHDF2 cells over NTC in MYC-induced HMECs. P-values were calculated compared to non-targets using two-sided Kolmogorov-Smirnov test. n = 4 replicates (2 hairpins x 2 biological replicates)
(B) Volcano plot describing the upregulated (red) and downregulated (blue) genes in shYTHDF2 cells compared with NTC in MYC-induced HMECs. YTHDF2 targets are shown in green and labels are bolded. Log_2FoldChange and Bonferroni adjusted p-values (padj) were calculated using DESeq2 (Love et al., 2014). Direct YTHDF2 targets identified by eCLIP-seq are in green. Significance cutoffs are at log_2FoldChange = 1 and -log_{10}padj = 3.
(C) Gene ontology (GO) enrichment of upregulated genes (red) and downregulated genes (blue) in shYTHDF2 cells compared with NTC in MYC-induced HMECs.
(D) GO enrichment of upregulated genes (red) and downregulated genes (blue) in shYTHDF2 MYC-induced HMECs compared with shYTHDF2 uninduced HMECs.

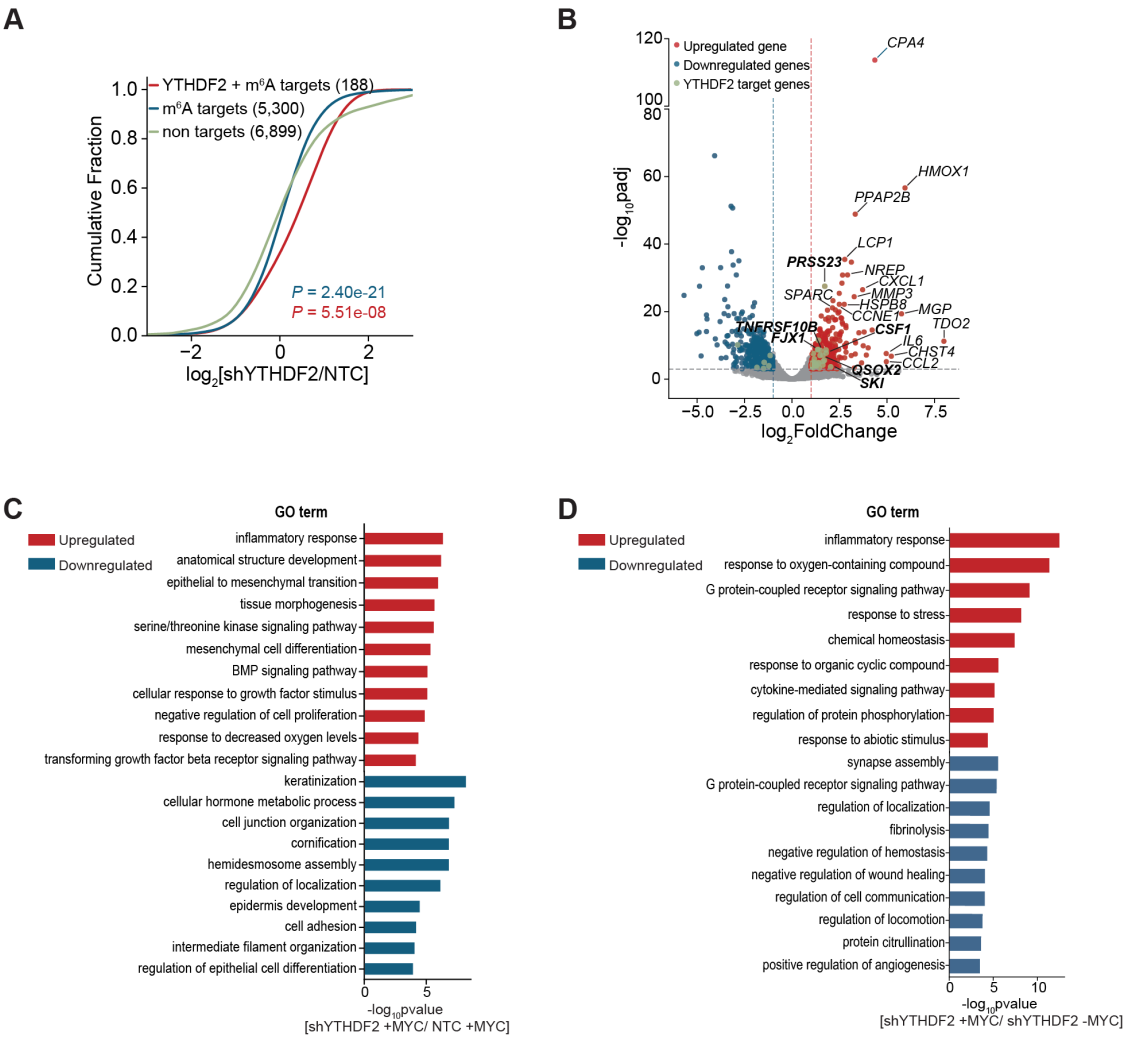
A
YTHDF2 + m6A targets (188)
m6A targets (5,300)
non targets (6,899)
Cumulative Fraction
P = 2.40e-21
P = 5.51e-08
log2[shYTHDF2/NTC]
B
Upregulated gene
Downregulated genes
YTHDF2 target genes
-log10padj
log2FoldChange
CPA4
HMOX1
PPAP2B
LCP1
PRSS23
NREP
CXCL1
SPARC
MMP3
HSPB8
MGP
CCNE1
TDO2
TNFRSF10B
CSF1
FJX1
IL6
CHST4
CCL2
QSOX2
SKI
C
GO term
Upregulated
Downregulated
inflammatory response
anatomical structure development
epithelial to mesenchymal transition
tissue morphogenesis
serine/threonine kinase signaling pathway
mesenchymal cell differentiation
BMP signaling pathway
cellular response to growth factor stimulus
negative regulation of cell proliferation
response to decreased oxygen levels
transforming growth factor beta receptor signaling pathway
keratinization
cellular hormone metabolic process
cell junction organization
cornification
hemidesmosome assembly
regulation of localization
epidermis development
cell adhesion
intermediate filament organization
regulation of epithelial cell differentiation
-log10pvalue
[shYTHDF2 +MYC/ NTC +MYC]
D
GO term
Upregulated
Downregulated
inflammatory response
response to oxygen-containing compound
G protein-coupled receptor signaling pathway
response to stress
chemical homeostasis
response to organic cyclic compound
cytokine-mediated signaling pathway
regulation of protein phosphorylation
response to abiotic stimulus
synapse assembly
G protein-coupled receptor signaling pathway
regulation of localization
fibrinolysis
negative regulation of hemostasis
negative regulation of wound healing
regulation of cell communication
regulation of locomotion
protein citrullination
positive regulation of angiogenesis
-log10pvalue
[shYTHDF2 +MYC/ shYTHDF2 -MYC]

Figure 3.6: **Depletion of YTHDF2 triggers activation of the EMT pathway in MYC-dependent breast cancer.**
(A) Cartoon schematic displaying upstream signaling pathways that induce ERK1/2 signaling and epithelial-to-mesenchymal transition (EMT) in breast cancer. YTHDF2 targets overlapping between MDA-MB-231-LM2 and MDA-MB-231 cells are listed in the grey box.
(B) Western blot analysis of cell lysates from NTC and shYTHDF2 MYC-dependent and MYC-independent breast cancer cell lines of SNAIL expression.
(C) Immunofluorescent staining at 20X magnification of Vimentin merged with DAPI in MYC-dependent cell lines. Arrow heads indicate cell projections. Scale bar = 50 μm.
(D) Cumulative distribution of the fold change in mRNA expression between shYTHDF2 compared with NTC in MYC-induced HMECs. Distributions describe transcripts that are direct targets of MYC (red) or non-MYC targets (blue). MYC targets were determined by MYC ChIP-seq data downloaded from the ENCODE Consortium (ENCSR000DOS).
(E) Venn diagram showing the overlap of MYC ChIP-seq targets from (D) with m^{6}A-intersecting YTHDF2 targets and upregulated transcripts during YTHDF2 depletion in MYC-induced HMECs.
(F) Western blot analysis of cell lysates from NTC and shYTHDF2 MYC-dependent and MYC-independent breast cancer cell lines for the ERK1/2 pathway and downstream effectors.

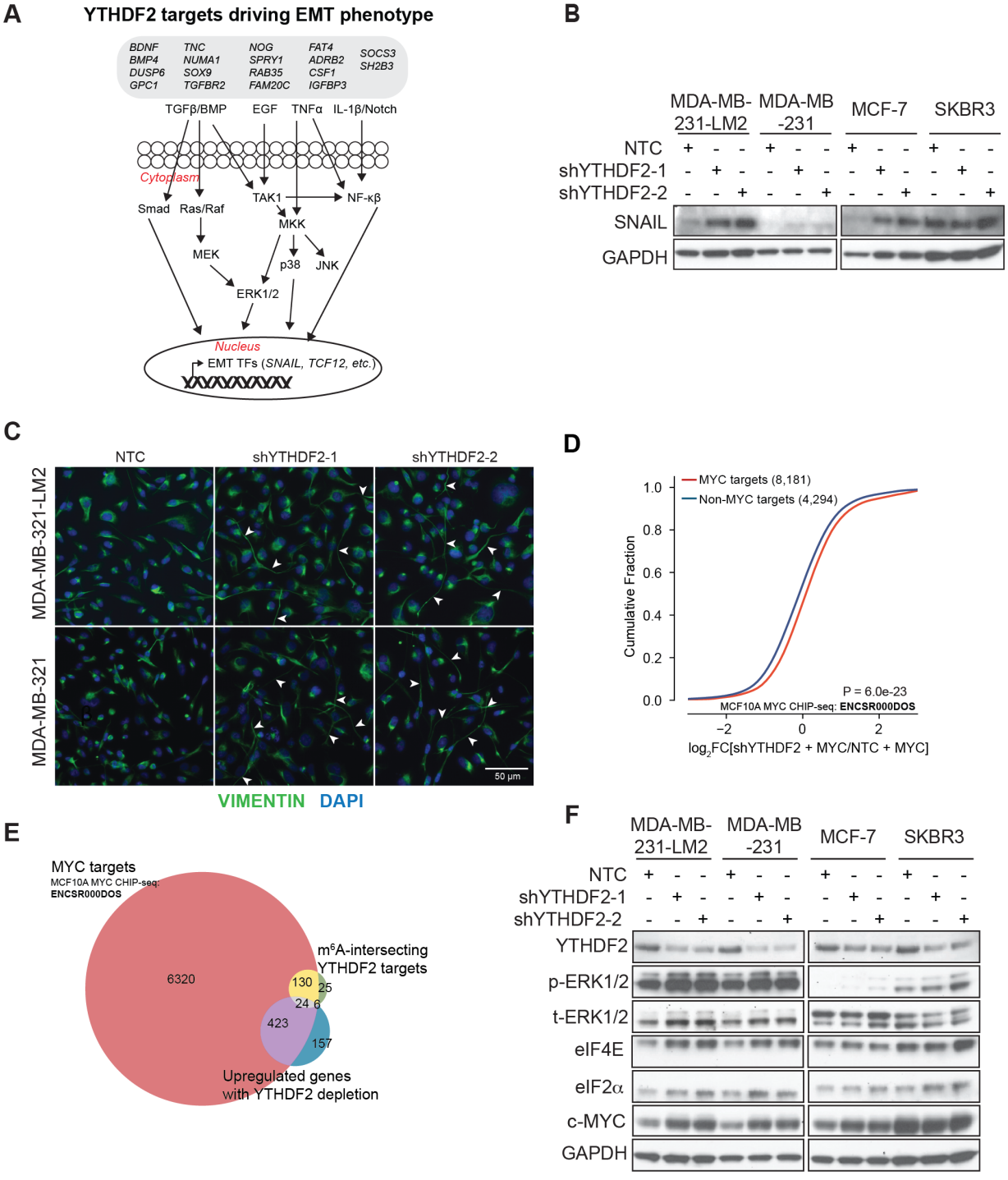
A
YTHDF2 targets driving EMT phenotype
BDNF BMP4 DUSP6 GPC1
TNC NUMA1 SOX9 TGFBR2
NOG SPRY1 RAB35 FAM20C
FAT4 ADRB2 CSF1 IGFBP3
SOCS3 SH2B3
TGFβ/BMP
EGF
TNFα
IL-1β/Notch
Cytoplasm
Smad
Ras/Raf
TAK1
NF-κβ
MKK
MEK
p38
JNK
ERK1/2
Nucleus
EMT TFs (SNAIL, TCF12, etc.)
B
MDA-MB-231-LM2
MDA-MB-231
MCF-7
SKBR3
NTC
shYTHDF2-1
shYTHDF2-2
SNAIL
GAPDH
C
NTC
shYTHDF2-1
shYTHDF2-2
MDA-MB-321-LM2
MDA-MB-321
50 μm
VIMENTIN DAPI
D
MYC targets (8,181)
Non-MYC targets (4,294)
Cumulative Fraction
P = 6.0e-23
MCF10A MYC CHIP-seq: ENCSR000DOS
log2FC[shYTHDF2 + MYC/NTC + MYC]
E
MYC targets
MCF10A MYC CHIP-seq: ENCSR000DOS
m6A-intersecting YTHDF2 targets
Upregulated genes with YTHDF2 depletion
6320
130
25
24
6
423
157
F
MDA-MB-231-LM2
MDA-MB-231
MCF-7
SKBR3
NTC
shYTHDF2-1
shYTHDF2-2
YTHDF2
p-ERK1/2
t-ERK1/2
eIF4E
eIF2α
c-MYC
GAPDH

Chapter 4

A role for PRSS23 in sensitizing MYC-dependent cancer cells to intrinsic apoptosis through the UPR

4.1 Introduction

Cells are equipped with several homeostatic control mechanisms to combat unexpected disturbances in normal cell function. The evolutionarily conserved unfolded protein response (UPR) responds to disturbances in cellular redox regulation that cause accumulation of unfolded proteins in the endoplasmic reticulum (ER) (C. Xu et al., 2005). The purpose of the UPR is to help the cell adapt to the changing environment and reestablish normal ER function, however, excessive prolonged ER stress can trigger apoptosis. Hence, during ER stress, there are three phases of cellular response through the UPR that can determine cell fate; adaptation, alarm and

apoptosis (C. Xu et al., 2005).

Initially when unfolded proteins accumulate in the ER, resident chaperone proteins and foldases activate adaptative responses through three ER transmembrane receptors, PERK, IRE1α and ATF6 (Rao & Bredesen, 2004). Activating the kinase domain of PERK globally down-regulates translation by phosphorylation and inactivation of translation initiation factor, eIF2α (Y. Shi et al., 1998). ATF6 actively increases transcription of XBP1 and IRE1α, when activated, initiates proper splicing of XBP1, increasing the transcription of genes that aid in the retrograde transport of misfolded proteins from ER to cytosol (Yoshida et al., 2001). Nevertheless, when excess protein production is pervasive, several immune responses are elicited during the "alarm" phase of the UPR including TNF signaling and activation of p38 MAPK and ASK1/JNK kinases by TRAF2, which triggers NFKβ signaling (Urano et al., 2000). ASK1/JNK activity plays an important role in apoptosis during chronic UPR signaling by promoting the translocation of pro-apoptotic factors to the mitochondria followed by caspase cleavage, thus, the IRE1α kinase is the only arm of the UPR that plays integrated roles in all three phases of response (Rao et al., 2001; C. Xu et al., 2005).

In cancer cells, there is a delicate balance between cell proliferation and cell death and this dual role is potentiated by several oncogenes and tumor suppressors. For example, *MYC* amplification has been reported to drive cancer cell transformation in part by activating cyto-protective autophagy via the UPR (Dey et al., 2013; Feng et al., 2014). The UPR alleviates metabolic and oxidative stress that accompanies cancer cell transformation and growth from increased growth factor signaling and protein synthesis and cells undergoing EMT are up to 25-fold more sensitive to ER stressors compared to cells that are not (Feng et al., 2014). MAPK signaling pathways are also known to be activated in response to ER stress and also form part

of the UPR (Darling & Cook, 2014).

While it is well-established that MYC can actuate both cell proliferation and apoptosis, evidence suggests that rather than inducing apoptosis directly, high levels of MYC expression may be responsible for sensitizing cells to apoptotic triggers (Hart et al., 2012). For example, expression of MYC can sensitize cells to extrinsic apoptosis by upregulating the cytokine receptor, TNFRSF10B (DR5) on cell surfaces and stimulating apoptosis by Caspase-8 cleavage (Klefstrom et al., 1994; Y. Wang et al., 2004). Similar to other tumor necrosis factor (TNF) receptors, DR5 was originally identified as a cell surface receptor that induces apoptosis after binding of TNF-related apoptosis-induced ligand (TRAIL) by sending death signals through adaptor molecule, FADD (Schneider et al., 1997; Wiley et al., 1995). However, it later became evident that in addition to TRAIL-dependent apoptosis, DR5 also regulates ligand-independent apoptosis through the UPR relative to levels of ER stress. Moreover, activation of Caspase-8 by DR5 during unresolved ER stress, which is signaled by persistent PERK-CHOP activity, allows engagement of the intrinsic apoptotic pathway via BID/BAX interaction and subsequent cytochrome c release (Lu et al., 2014). Additional studies suggest that MYC contributes to apoptosis downstream of the UPR. MYC does not affect BAX mRNA or protein expression nor does it affect the translocation of BAX to the mitochondria, however, it has been shown to activate BAX. Thus, MYC alone is insufficient to induce apoptosis but rather encourages apoptotic commitment in cells exhibiting weak apoptotic response to hypoxia, glucose deprivation, heat shock or DNA damage (Soucie et al., 2001).

Recently, depletion of YTHDF2 been shown to sensitize MYC-amplified acute myeloid leukemia (AML) cells to TNF-induced apoptosis (Paris et al., 2019). However, it is known that MYC expression can generally increase the sensitivity of cells to apoptosis, regardless of the

source. In this chapter, we aim to clarify the precise pathway triggering apoptosis in YTHDF2-depleted MYC-dependent cancer cells by probing the activity of both the extrinsic and intrinsic apoptotic pathways in response to changes in individual YTHDF2 mRNA target expression.

4.2 Results

4.2.1 Depletion of YTHDF2 sensitizes MYC-dependent cancer cells to proteotoxicity

First, we verified activation of apoptosis via the UPR by probing the IRE1α/JNK cascade known to respond to unfolded proteins in the ER. Following YTHDF2 depletion, we observed upregulated expression of ER chaperone and foldase proteins including GRP78 (BiP), which is indicative of unfolded protein accumulation (**Figure 4.1A-4.1B**). In addition, we detected phosphorylation of IRE1α and JNK, followed by Caspase-3 cleavage in MYC-dependent cell lines, but not in MYC-independent cell lines (**Figure 4.1A**), indicating chronic UPR signaling. By cross-referencing public mass spectrometry data for 83 tumor samples provided by the Clinical Proteomic Tumor Analysis Consortium (CPTAC) from TCGA's Cancer Proteome Study of Breast Tissue (Mertins et al., 2016) we found that YTHDF2 expression is negatively correlated with MAPK activity and that tumor samples with lower YTHDF2 expression have higher levels of ASK1 (MAP3K5), JNK1/2 (MAPK8/9), and p38 (MAPK14) phosphorylation (**Figure 4.1C**). Activation of this pathway confirms the presence of ER stress, however, ER stress response can result from several stressors including hypoxia, oxidative stress, inflammation, and proteotoxicity (Cubillos-Ruiz et al., 2017).

4.2.2 Analysis of intrinsic and extrinsic apoptotic signaling pathways that are altered by depletion of YTHDF2 in MYC-dependent cells

To further dissect the extrinsic and intrinsic apoptotic pathways driving the phenotype (**Figure 4.2A**) we examined the most significantly upregulated YTHDF2 target transcripts in YTHDF2-depleted MYC-induced HMECs, with strong YTHDF2 binding signal centered on m^6A sites that also had evidence for activity within these pathways (**Figure 4.2B-4.2C**).

We first focused on TNFRSF10B (**Figure 4.2B**) by probing DR5-induced apoptotic activity by depleting YTHDF2 and DR5 simultaneously. While we did observe a rescue of Caspase-8 cleavage in the double knockdown compared to YTHDF2-only depleted cells, we surprisingly did not observe a rescue of downstream apoptosis indicated by persistent cleaved Caspase-3 signal (**Figure 4.2D**). Therefore, we concluded that while it is possible that depletion of YTHDF2 in MYC-dependent cells may increase the sensitivity of cells to TNF-induced apoptosis due to apoptotic predisposition, activation of the extrinsic apoptotic pathway is not directly responsible for cell death caused by YTHDF2 depletion.

We next focused on Serine Protease 23 (PRSS23) since it was the most significantly upregulated target during YTHDF2 depletion (**Figure 3.5B**). In addition, evidence indicates that serine proteases play an important role in mediating intrinsic apoptosis during ER stress by facilitating outer mitochondrial membrane perforation and cytochrome c release (Egger et al., 2003) and in parallel, serine protease inhibitors can prevent the activation of ER stress pathways (Okada et al., 2003). PRSS23 is a relatively novel serine protease and limited studies have linked its potential function to translation regulation through modulation of the eIF2 signaling pathway (Han et al., 2019). Since chronic UPR signaling was activated in YTHDF2-depleted, MYC-dependent cells, we next we evaluated if destabilization of YTHDF2's functional target

PRSS23 is sufficient for capitulating YTHDF2's protective role on MYC-dependent cells by testing if inhibiting PRSS23 accumulation in , YTHDF2-depleted, MYC-dependent cells prevented increases in cap-dependent translation that we found were driving UPR activation. Indeed, depletion of YTHDF2 and PRSS23 together produced a substantial reduction in protein levels of translation initiation factors, eIF4E and eIF2α, MYC and Cl. Caspase-3 compared to silencing of YTHDF2 alone (**Figure 4.2E**). As a result, we also observed that PRSS23 depletion rescued cell proliferation rates in YTHDF2-depleted, MYC-dependent cell lines by time-lapse microscopy (**Figure 4.2F-4.2G**).

4.2.3 The effect of PRSS23 on the intrinsic apoptotic pathway

To verify that double knockdown of YTHDF2 and PRSS23 rescued UPR signaling, we assayed ROS levels and levels of spliced XBP1 (XBP1s), which were significantly upregulated with YTHDF2 silencing by $\sim$16% and $\sim$5 fold, respectively. Double knockdown reduced ROS levels by $\sim$50% and significantly reduced mRNA expression of spliced XBP1 (XBP1s) (**Figure 4.3A-4.3B**). This trend was mirrored by expression of downstream eIF2 stress induced signaling genes which are induced by PERK signaling, as expected (**Figure 4.3C**) and in agreement with previous reports (Han et al., 2019). Further probing of the intrinsic apoptotic pathway revealed increased levels of BAX, Cl. Caspase-9, and Cl. Caspase-3 in YTHDF2 depleted MDA-MB-231-LM2 cells while silencing both YTHDF2 and PRSS23 rescued protein expression levels within this pathway, indicating that stabilization of the *PRSS23* transcript promotes apoptosis from intrinsic mitochondrial stress (**Figure 4.3D**).

4.2.4 Regulation of the TCF12 transcription factor by YTHDF2 target, PRSS23

PRSS23 has been shown to localize in the nucleus and interact with TCF12, a TF that regulates transcription of *SNAIL*, *CXCL12*, *CXCR4* and other related genes that promote MYC expression and metastatic phenotypes (I. H. Chen et al., 2013; Yang et al., 2019). Since *SNAIL* is minimally expressed in MDA-MB-231 cells, we continued our analysis in MDA-MB-231-LM2 cells which were derived from secondary tumors and have clear and detectable upregulation of SNAIL expression with YTHDF2 depletion (**Figure 4.2E**). While PRSS23 has been shown to promote the expression of TCF12-regulated transcripts (I. H. Chen et al., 2013), the mechanism underlying their interaction is not clear. Protein-protein interaction between PRSS23 and TCF12 has been identified by mass spectrometry and co-immunoprecipitation studies (I. H. Chen et al., 2013; Stelzl et al., 2005), so we first confirmed co-localization in nuclei of MDA-MB-231-LM2 cells (**Figure 4.4A**). We next analyzed publicly available ChIP-seq data in MCF-7 cells to determine if TCF12's targets were generally upregulated in YTHDF2-depleted cells and we found by gene ontology that generally, many of the upregulated gene pathways in the YTHDF2 depleted cells could be explained by upregulated transcription of TCF12's targets (**Figure 4.4B**) (ENCODE; ENCSR000BUN). In addition, we observed an increase in smaller TCF12 protein products following YTHDF2 depletion that we speculated had been cleaved by PRSS23 to produce 50 and 35 kDa fragments whereas its predicted molecular weight is $\sim$72 kDa (**Figure 4.3D**). Since previous studies found that PRSS23 protects estrogen receptor α (ERα) from proteasome-mediated degradation (Chan et al., 2012), we hypothesized that PRSS23 may stabilize nuclear proteins that undergo rapid ubiquitin-dependent degradation from 20S proteasomes by cleaving polyubiquitin chains. To test this theory, we treated MDA-MB-231-LM2 cells with MG132 to inhibit proteasome activity and we observed increased polyubiquitin signal in

cells with PRSS23 depletion. In addition, BAX, which is known to undergo ubiquitin/proteasome-mediated degradation, especially in cancer cells (B. Li & Dou, 2000), along with TCF12 and PRSS23 was less degraded in cells with YTHDF2 depletion (**Figure 4.4C**). This suggests that both PRSS23 and TCF12 protein may be regulated by ubiquitin-mediated proteolysis, which adds another layer by which MYC-dependent cells are able to restrict expression of PRSS23. In conclusion, we identified a new facet of regulation by m^6A in MYC-dependent cancer where the m^6A reader YTHDF2 binds to and targets the *PRSS23* transcript for degradation, protecting cancer cells from proteotoxicity by limiting TCF12-regulated transcription.

4.2.5 PRSS23 activates non-canonical hypoxic cap-dependent translation

Lastly, we aimed to determine if stabilization of PRSS23 and transcription of TCF12's targets could explain the increases in cap-dependent translation we observed during YTHDF2 depletion of MYC-dependent cells. From the publicly available ChIP-seq data in MCF-7 cells (ENCODE; ENCSR000BUN), we found that TCF12 binds and regulates the transcription of several translation initiation factors including eIF4E2, eIF4E3, and eIF4A2 (**Figure 4.5A**). Under normal physiological conditions eIF4E2 and eIF4E3 act as inhibitors of translation initiation, however, there is evidence indicating eIF4E2 participates in active translation during hypoxic conditions and that eIF4E3 promotes tissue specific translation (Uniacke et al., 2012). This suggests that these homologues have specialized roles in regulating translation during tumor initiation and metastatic progression (Genuth & Barna, 2018). To confirm upregulation of these factors on the mRNA level, we performed RT-qPCR in MDA-MB-231-LM2 cells with various combinations of YTHDF2 and PRSS23 knockdown. We found that indeed, transcription of eIF4E2, eIF4E3, and eIF4A2 is upregulated in YTHDF2-depleted cells and regressed upon double knockdown of

YTHDF2 and PRSS23 (**Figure 4.5B**). Thus, we deduced that transcription regulated by TCF12 comprises one of the many pathways that become upregulated following YTHDF2 depletion in MYC-dependent cells. In combination with several other pathways that lead to EMT, transcription of TCF12 targets is necessary to produce sufficient ER stress to induce mitochondrial dysfunction.

4.3 Discussion

YTHDF2 maintains mRNA homeostasis by limiting the number of translating mRNAs in cancer cells. Without precise regulation of the cell's survival/apoptotic balance, excessive translation can relay an enormous amount of cellular stress, especially in cells with MYC amplifications, tipping the scale toward apoptotic commitment. We examined whether these newly translated proteins in YTHDF2 depleted cells were being folded and processed properly by probing the UPR pathway to determine if there was evidence of ER stress. Indeed, we detected significantly elevated ROS levels, upregulated transcription of chaperone genes regulating protein folding and assembly and phosphorylation of downstream effectors of ER lumen receptor, IRE1α. Ultimately, we found that in cells containing MYC amplifications, upregulation of EMT-related genes in YTHDF2 depleted cells lead to apoptosis due to the inability of the cells to attenuate translation to correspond with ER protein-folding capacity rather than driving tumor progression.

Previous reports have attributed the function of YTHDF2 in various cancers to the regulation of singular target mRNAs by RNA-pull-down approaches followed by RT-qPCR (M. Chen et al., 2018; Paris et al., 2019; Zhong et al., 2019). However, since our integrated epitranscriptomic analysis presented in Chapter 3 revealed many candidate YTHDF2 targets, we ex-

amined the individual targets of YTHDF2 more closely to determine how they might uniquely contribute to apoptosis. We performed rescue experiments by depleting two YTHDF2 mRNA targets, *TNFRSF10B* (DR5) and *PRSS23*, which are thought to promote extrinsic or intrinsic apoptosis when upregulated in cancer. Although agonists of DR5 have been shown to potently induce apoptosis in MYC-amplified cells (Y. Wang et al., 2004), simultaneous depletion of DR5 and YTHDF2 failed to prevent Caspase-3 cleavage, a hallmark of apoptosis. We therefore concluded that the extrinsic apoptotic pathway was not primarily responsible for provoking apoptosis as initially presumed. Instead, we observed that Caspase-3 cleavage was inhibited by reversing intrinsic, mitochondrial apoptosis that resulted from overactive protein translation and ER stress, mediated by the stabilization and expression of YTHDF2 target mRNA, *PRSS23*.

PRSS23 is a serine protease belonging to the trypsin class that has been described to be upregulated in cancer stem cells (Tanabe & List, 2017). While recent studies show that PRSS23 regulates translation through eIF2 signaling (Han et al., 2019) and also promotes the transcription of *SNAIL* and similar genes by interacting with the *TCF12* TF (I. H. Chen et al., 2013), the precise proteolytic substrates of PRSS23 mediating downstream gene regulation remain unclear. We observed that stabilizing PRSS23 protein levels resulted in an accumulation of proteolytic cleavage products of TCF12 which dissipated with PRSS23 depletion. Since PRSS23 can protect other nuclear substrates from proteasomal degradation (Chan et al., 2012), we hypothesized that PRSS23 likely cleaves polyubiquitin chains to prevent protein degradation by the 20S proteasome. Indeed, proteasome inhibition stabilized protein levels of both PRSS23 and TCF12 protein, providing an additional layer by which MYC-dependent cancer cells regulate expression of PRSS23 and activity of TCF12 post-translationally. Our data therefore suggests that PRSS23 stabilizes TCF12 and promotes the transcription of cancer lineage-specific translation

initiation factors and other transcripts that contribute to breast tumorigenesis. Altogether, we determined that increased TCF12-mediated transcription is necessary for prompting widespread changes in the translatome of YTHDF2-depleted cells, leading to ER overload.

4.4 Materials and Methods

4.4.1 Cell Culture

Immortalized human cell lines were used in this study. HEK293xT, MDA-MB-231, MDA-MB-231-LM2, and MCF-7 cells were cultured in DMEM supplemented with 10% fetal bovine serum. SKBR3 cells were cultured in McCoy's 5A Medium supplemented with 10% fetal bovine serum. Cells were passaged every 3 or 4 days with TrypLE EXPRESS (Life Technologies) using standard methods. Cells were maintained in a humidified incubator at 37°C with 5% CO_2.

4.4.2 Lentivirus production and purification

HEK293xT cells were seeded at 80% confluency the day before transfection. Transfections were performed using 25 μL Lipofectamine 3000 (Thermofisher), 30 μL p3000 reagent (Thermofisher), 3 μg shRNA vector, 300 ng of pMD.2g, and 3 μg psPAX2 according to manufacturer's instructions per 10 cm plate. Media was changed 6 hours after transfection to DMEM + 10% FBS. After 48 hours, the supernatant was filtered through a 0.45 μm low protein binding membrane. The virus was concentrated using Lenti-X Concentrator (Takara Bio) according to manufacturer's instructions and resuspended in PBS. Virus aliquots were stored at -80°C.

4.4.3 Knockdown experiments

Cells were transduced with TRC lentiviral shRNA vector non-targeting control (NTC; Millipore Sigma; SHC002), and TRC lentiviral shRNA vector YTHDF2 (shYTHDF2-1; Millipore Sigma; TRCN0000168751), (shYTHDF2-2; Millipore Sigma; TRCN0000167813), TRC lentiviral shRNA vector PRSS23 (shPRSS23; TRCN0000047042) or TRC lentiviral shRNA vector TN-

FRSF10B (shDR5; TRCN0000005929) for 24 hours before treatment with Puromycin (2 mg/mL). Cells were analyzed 6 days after the addition of lentivirus for all assays.

4.4.4 Immunofluorescence

Cells were seeded on poly-D-lysine hydrobromide (PDL) (Millipore Sigma; P6407) coated 8-well chamber slides (Millipore Sigma). Cells were fixed in 4% paraformaldehyde in PBS, permeabilized and blocked 5% normal goat serum, 0.1% Triton-X in PBS for 1 hour at RT. Primary antibody: Mouse mAb anti-HEB (TCF12) (Santa Cruz, sc-28364), Rabbit pAb anti-PRSS23 (Abcam; ab201182) was diluted in blocking buffer and incubated overnight at 4°C. Cells were washed 3 times in 0.1% Triton-X in PBS and incubated with secondary antibody: Goat anti-Rabbit IgG Alexa Fluor 555 (Invitrogen; A-21428), Goat anti-Mouse IgG Alexa Fluor 647 (Invitrogen; A-21052) for 1 hour at RT, followed by 3 washes and coverslip mounting with Prolong Diamond Antifade Mountant with DAPI (Thermofisher). Slides were imaged on a ZEISS Axio Vert.A1 inverted microscope.

4.4.5 Western Blot

Cells were lysed with cold RIPA buffer (Thermofisher) with 200X Protease inhibitor and 100X phosphatase inhibitor. Protein was quantified using Peirce BCA Protein Assay Kit. Total protein extracts were run on 4%-12% NuPAGE Bis-Tris gels in NuPAGE MOPs running buffer (Thermofisher) and transferred to PVDF membranes. Membranes were blocked in 5% nonfat milk in TBST for 1 hour, incubated overnight at 4°C with the following primary antibodies: Rabbit pAb anti-YTHDF2 (Proteintech; 24744-1-AP), Rabbit mAb anti-eif4e (Cell Signaling; 9742), Rabbit pAb anti-eif2α (Cell Signaling; 9722), Rabbit mAb anti-c-Myc (Cell Signaling; 13987),

Mouse mAb anti-GAPDH (Abcam; ab8245), Rabbit mAb anti-Cleaved Caspase-3 (Cell Signaling; 9664), Rabbit mAb anti-Snail (Cell Signaling; 3879), Rabbit pAb anti-PRSS23 (Abcam; ab201182), Rabbit pAb anti-DR5 (Cell Signaling; 3696), Rabbit mAb anti-Cleaved Caspase-8 (Cell Signaling; 9496), Mouse mAb anti-HEB (TCF12) (Santa Cruz, sc-28364), Rabbit mAb anti-Bax (Cell Signaling; 5023), Mouse mAb anti-Ubiquitinylated proteins (Milipore Sigma, 04-263), washed 3X for 5 minutes with TBST, incubated for 1 hour at RT in 5% nonfat milk in TBST with secondary HRP-conjugated antibody: Goat anti-Mouse IgG Secondary Antibody, HRP (Invitrogen; 31430), Goat anti-Rabbit IgG Secondary Antibody, HRP (Invitrogen; 31460) at 1:5000 dilution, and washed 3X for 5 minutes with TBST. Membranes were developed using Thermo Pierce ECL detection reagents.

4.4.6 Cellular ROS assay

MDA-MB-231-LM2 cells were transduced with NTC, shYTHDF2, or both shYTHDF2 and shPRSS23 virus at MOI $>$ 1 and selected for 2-3 days with 2 μg/mL puromycin (Thermofisher Scientific; A1113803). The cellular ROS assay was performed (Abcam; ab186029) according to manufacturer's instructions. Cells were analyzed by flow cytometry using the BDSLRFortessa under the APC-Cy7 (deep red) channel. Analysis and gating were performed in FlowJo.

4.4.7 RT-qPCR Analysis

RNA was extracted with Direct-zol RNA Miniprep kit by Zymo Research for three biological replicates and cDNA synthesized from 1 μg total RNA using High-Capacity cDNA Reverse Transcription kit (Applied Biosystems; 4368814) according to manufacturer's instructions. Real-time PCR was performed using Power SYBR Green PCR Master Mix (Applied Biosystems).

Values of gene expression were normalized to GAPDH expression and are shown as relative expression. Primers are as follows: Human (5'-3'):

GAPDH_F GAAGGTGAAGGTCGGAGTC;

GAPDH_R GAAGATGGTGATGGGATTTC;

YTHDF2_F GGAGCAGAGACCAAAAGGTCA;

YTHDF2_R GCATTATTGGGCCTTGCCTG;

PRSS23_F ACATCAGTGAAGTTATCCACGGGCT;

PRSS23_R CCTCGACCACCATCTTTAAACTTGG;

CHOP_F CCTTTCTCCTTCGGGACACT;

CHOP_R TTGATTCTTCCTCTTCATTTCCAGG;

ATF3_F AAGAACGAGAAGCAGCATTTGAT;

ATF3_R TTCTGAGCCCGGACAATACAC;

TRIB3_F GCCTTTTTCACTCGGACCCAT;

TRIB3_R CAGCGAAGACAAAGCGACAC;

GADD34_F TCCGAGTGGCCATCTATGTA;

GADD34_R AGGGTCCGGATCATGAGTAG;

uXBP1_F CAGACTACGTGCACCTCTGC;

uXBP1_R CTGGGTCCAAGTTGTCCAGAAT;

sXBP1_F GCTGAGTCCGCAGCAGGT;

sXBP1_R CTGGGTCCAAGTTGTCCAGAAT;

tXBP1_F TGAAAAACAGAGTAGCAGCTCAGA;

tXBP1_R CCCAAGCGCTGTCTTAACTC;

eIF4E2_F CAGCACACAGAAAGATGGTGA;

eIF4E2_R CTCCAGAACTGCTCCACAGAG;

eIF4E3_F ACCACTTTGGGAAGAGGAGAG;

eIF4E3_R GGTCCCGAACACTGACACTAA;

eIf4A2_F AATTCCGGTCAGGGTCAAGTC;

eIf4A2_R GCCACACCTTTCCTCCCAAA;

PPP1R15B_F TCGGTACAGCGTGACGTTC;

PPP1R15B_R GCGATCCTCATCACCACTTAT;

4.4.8 Gene Ontology (GO) Analysis

GO multiple list analysis were conducted using the Metascape resource (Y. Zhou et al., 2019). GO terms were ranked by Bonferroni-corrected hypergeometric p-values.

4.4.9 Time Lapse Microscopy

Cells were seeded at 5K cells in IncuCyte ImageLock plates (Essen BioSciences; 4379). The next day, plates were loaded into the IncuCyte and imaged at 10X magnification for 84 hours every 12 hours. Phase images were analyzed using the IncuCyte ZOOM Basic Analyzer to measure confluence.

4.4.10 TCGA data description

We obtained proteomics and phosphoproteomics profiling data from the CPTAC at `https://cptac-data-portal.georgetown.edu/cptac/s/S029`. For detailed information, refer to Mertins et al., 2016. After removing the missing values, Pearson's correlation tests were performed to analyze the correlation between each of the known players in the IRE1α branch of the

UPR pathway and YTHDF2 expression for targets found in $>$50% of samples.

4.4.11 Statistical Analysis

For hypothesis testing, variance was assumed normal for Student's t-test.

4.5 Acknowledgements

We would like to thank the Sanford Consortium Human Embryonic Stem Cell Core for allowing use of their instruments (BD Influx Cell Sorter, X-20 Fortessa, BioRad CFX 384, IncuCyte (1S10OD025060), and Zeiss AxioImager). J.M.E is supported by the Ruth. L. Kirschstein F31 National Research Service Award (F31 CA217173) and Cancer Systems Biology Training Program (P50 GM085764 and U54 CA209891). Data used in this publication were generated by the Clinical Proteomic Tumor Analysis Consortium (NCI/NIH). We downloaded the ChIP-seq datasets from the ENCODE portal (Sloan et al., 2016) with the following identifier: ENCSR000BUN (Richard Meyers).

Chapter 4, in full, is a reprint of material as it will appear in: **Einstein JM**, Perelis M, Chaim IA, Meena JK, Nussbacher JK, Tankka AT, Yee BA, Li H, Madrigal AA, Neill NJ, Shankar A, Tyagi S, Westbrook TF, Yeo GW. Inhibition of YTHDF2 triggers proteotoxic cell death in MYC-dependent cancer. *In preparation*. The dissertation author is the primary author of this paper.

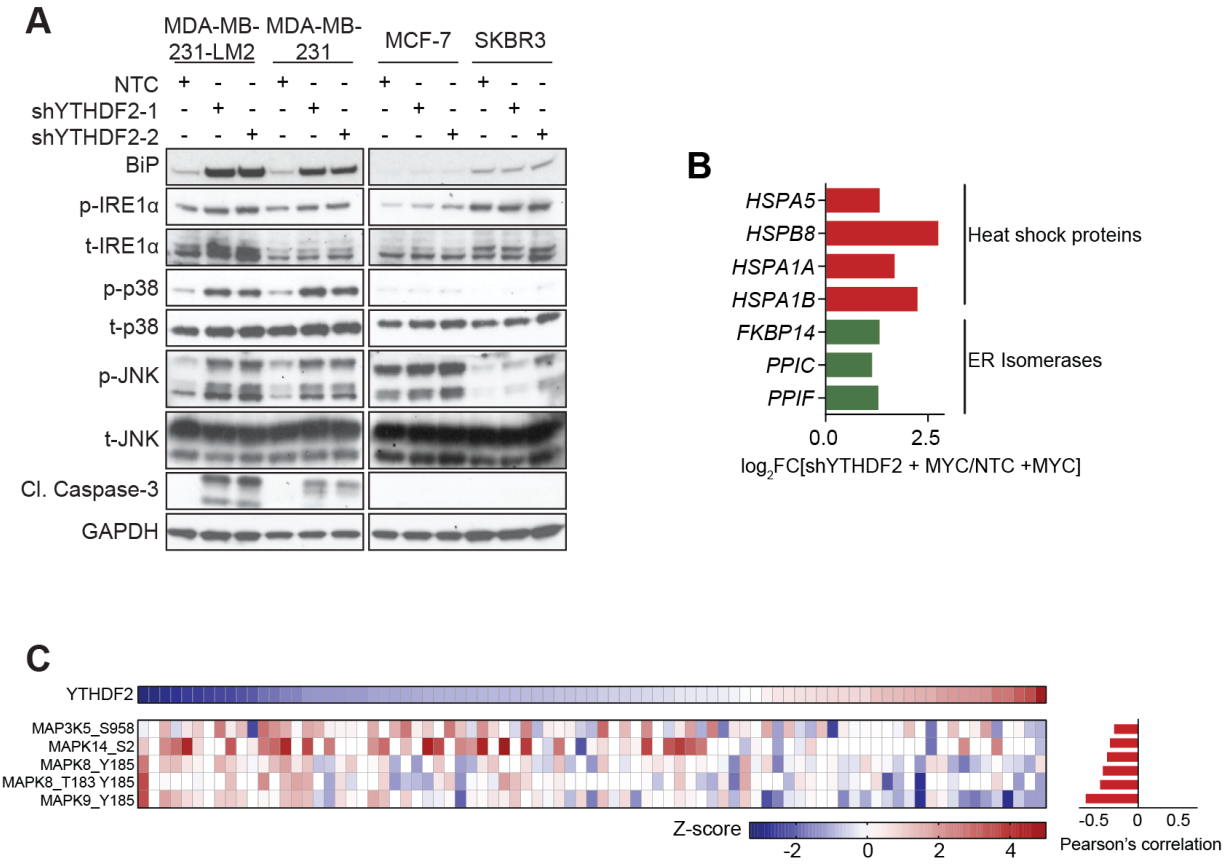

Figure 4.1: **Activation of the UPR in YTHDF2-depleted MYC-dependent cells.**
(A) Western blot analysis of cell lysates from NTC and shYTHDF2 MYC-dependent and MYC-independent breast cancer cell lines showing the expression of the IRE1α/JNK arm of the UPR pathway.
(B) Bar chart describing the fold change in mRNA expression of significant protein folding chaperone genes in shYTHDF2 compared with NTC in MYC-induced HMECs. Fold change was calculated by DESeq2 (Love et al., 2014).
(C) Heatmap showing the correlation of YTHDF2 and the IRE1α branch of UPR protein levels in human breast cancer phospho-proteomics data downloaded from the CPTAC Data Portal (left) (Mertins et al., 2016). Each column is an individual tumor. Bar plot shows Pearson's correlation scores of YTHDF2 to each phosphorylated protein (right). n=83 breast cancer tumors. Only significant correlations are shown ($p<0.05$).

Figure 4.2: **Depletion of YTHDF2 causes cell death via the mitochondrial intrinsic apoptotic pathway in MYC-dependent cells.**
(A) Cartoon schematic displaying the pathways that control extrinsic vs. intrinsic apoptosis and how they are induced.
(B-C) Genome browser tracks (human genome build hg19) depicting the YTHDF2 eCLIP peaks (light blue) over size-matched input (dark blue) and m^6A methylation peaks (light red) over input (dark red) on the (B) *TNFRSF10B* and (C) *PRSS23* transcript.
(D) Western blot analysis of cell lysates from YTHDF2 single knockdowns and double knockdowns with TNFRSF10B (DR5) in MYC-dependent breast cancer cell lines to probe the extrinsic apoptotic pathway.
(E) Western blot analysis of cell lysates from YTHDF2 single knockdowns and double knockdowns with PRSS23 in MYC-dependent breast cancer cell to probe the cap-dependent translation pathway.
(F-G) Confluency of time-lapse microscopy phase images acquired and analyzed by IncuCyte at 10X in single YTHDF2 and double YTHDF2/PRSS23 knockdown in (F) MDA-MB-231-LM2 cells and (G) MDA-MB-231 cells. *$p<0.05$, **$p<0.01$, ***$p<0.001$, ****$p<0.0001$, two-way ANOVA test with Dunnett's post-hoc test for multiple comparisons. Values normalized to initial average confluence compared to NTC. Bars are mean $\pm$ SD, n = 6 independent replicates.

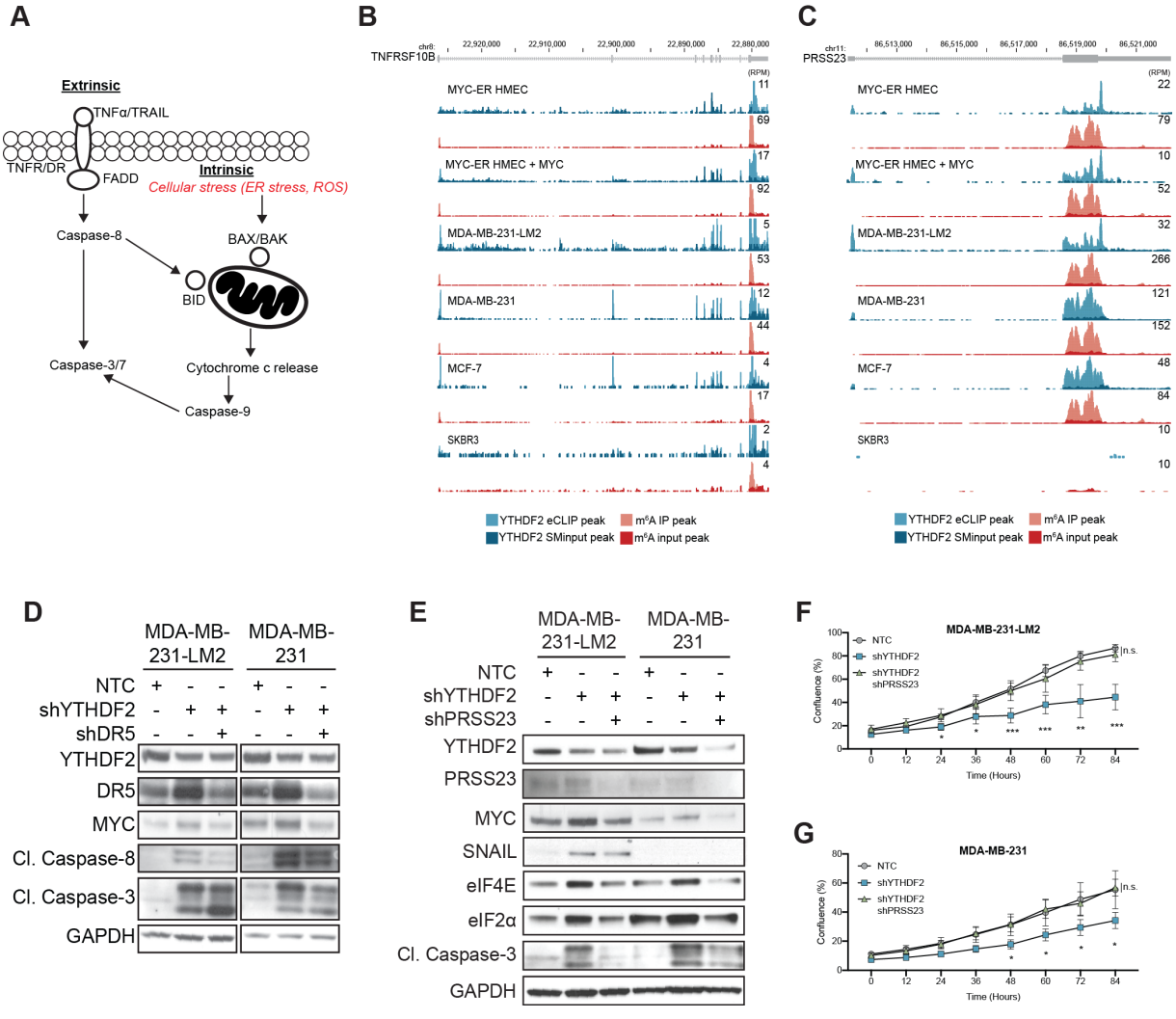
A
Extrinsic
TNFα/TRAIL
TNFR/DR
FADD
Intrinsic
Cellular stress (ER stress, ROS)
Caspase-8
BAX/BAK
BID
Caspase-3/7
Cytochrome c release
Caspase-9
B
TNFRSF10B
MYC-ER HMEC
MYC-ER HMEC + MYC
MDA-MB-231-LM2
MDA-MB-231
MCF-7
SKBR3
YTHDF2 eCLIP peak
m6A IP peak
YTHDF2 SMinput peak
m6A input peak
C
PRSS23
MYC-ER HMEC
MYC-ER HMEC + MYC
MDA-MB-231-LM2
MDA-MB-231
MCF-7
SKBR3
YTHDF2 eCLIP peak
m6A IP peak
YTHDF2 SMinput peak
m6A input peak
D
MDA-MB-231-LM2
MDA-MB-231
NTC
shYTHDF2
shDR5
YTHDF2
DR5
MYC
Cl. Caspase-8
Cl. Caspase-3
GAPDH
E
MDA-MB-231-LM2
MDA-MB-231
NTC
shYTHDF2
shPRSS23
YTHDF2
PRSS23
MYC
SNAIL
eIF4E
eIF2α
Cl. Caspase-3
GAPDH
F
MDA-MB-231-LM2
NTC
shYTHDF2
shYTHDF2 shPRSS23
Confluence (%)
Time (Hours)
n.s.
G
MDA-MB-231
NTC
shYTHDF2
shYTHDF2 shPRSS23
Confluence (%)
Time (Hours)
n.s.

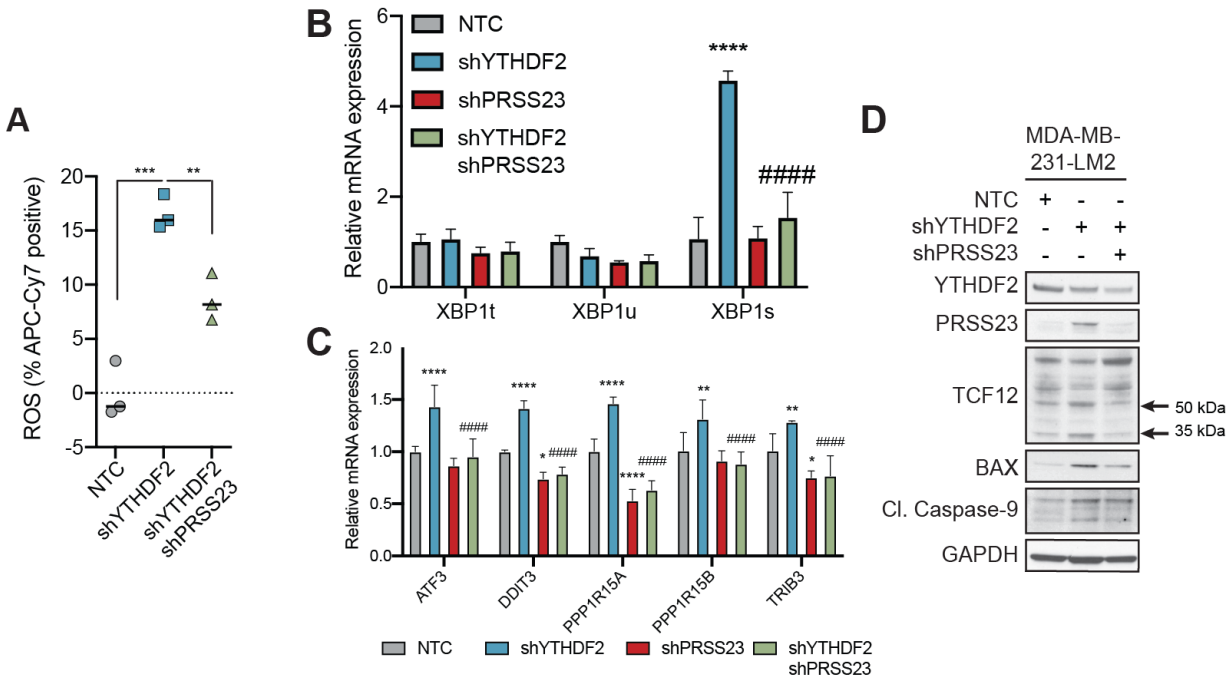

Figure 4.3: **Stabilization of the *PRSS23* transcript is necessary for inducing chronic UPR response and intrinsic apoptosis.**

(A) Quantification of reactive oxygen species (ROS) measured by FACS in the APC-Cy7 channel of single YTHDF2 and double YTHDF2, PRSS23 knockdowns compared to NTC. **$p<0.01$, ***$p<0.001$, two-way ANOVA test with Dunnett's post-hoc test for multiple comparisons. Bars = median, n = 3 indepedent replicates.

(B-C) RT-qPCR analysis of mRNA extracted from YTHDF2 and PRSS23 single and double knockdown cells compared to NTC in MDA-MB-231-LM2 cells. Data describes mRNA expression level for (B) XBP1 slice isoforms (XBP1t: total, XBP1u: unspliced, XBP1s: spliced) and (C) eIF2 signaling pathway genes relative to GAPDH. ****$p<0.0001$, n.s. = not significant, two-way ANOVA test with Dunnett's post-hoc test for multiple comparisons to NTC. ####$p<0.0001$, two-way ANOVA test with Dunnett's post-hoc test for multiple comparisons to shYTHDF2. Bars are mean $\pm$ SD, n = 3 independent replicates.

(D) Western blot analysis of cell lysates from MDA-MB-231-LM2 cells with YTHDF2 single and YTHDF2, PRSS23 double knockdowns compared to NTC of intrinsic mitochondrial apoptotic pathway, activated by TCF12 transcriptional activity. Arrows on TCF12 indicate cleaved and active TCF12 protein.

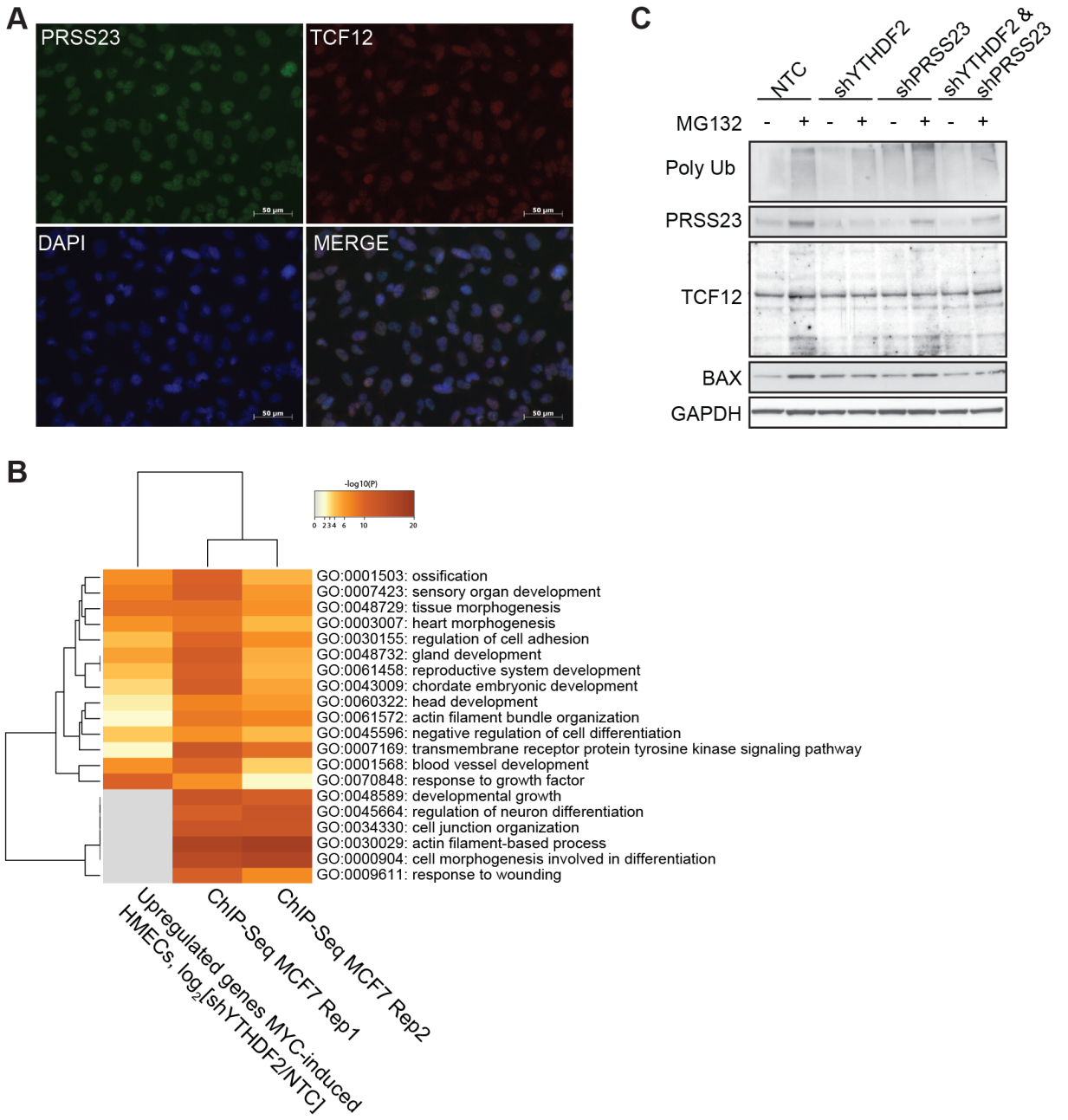

Figure 4.4: **PRSS23 stabilizes TCF12 by deubiquitylation.**
(A) Immunofluorescent staining at 40X magnification of PRSS23 in the green channel and TCF12 in the red channel merged with DAPI in MDA-MB-231-LM2 cells. Scale bar = 50 μm.
(B) Metascape multiple list analysis of the top 20 significantly enriched GO terms for TCF12 ChIP-seq targets compared to upregulated transcripts in MYC-induced, shYTHDF2 HMECs compared to NTC. TCF12 targets were determined by TCF12 ChIP-seq data downloaded from the ENCODE Consortium (ENCSR000BUN).
(C) Ubiquitination western blot analysis of MDA-MB-231-LM2 cell lysates with and without MG132 treatment. Cells were treated with 20 μM MG132 for 4 hours.

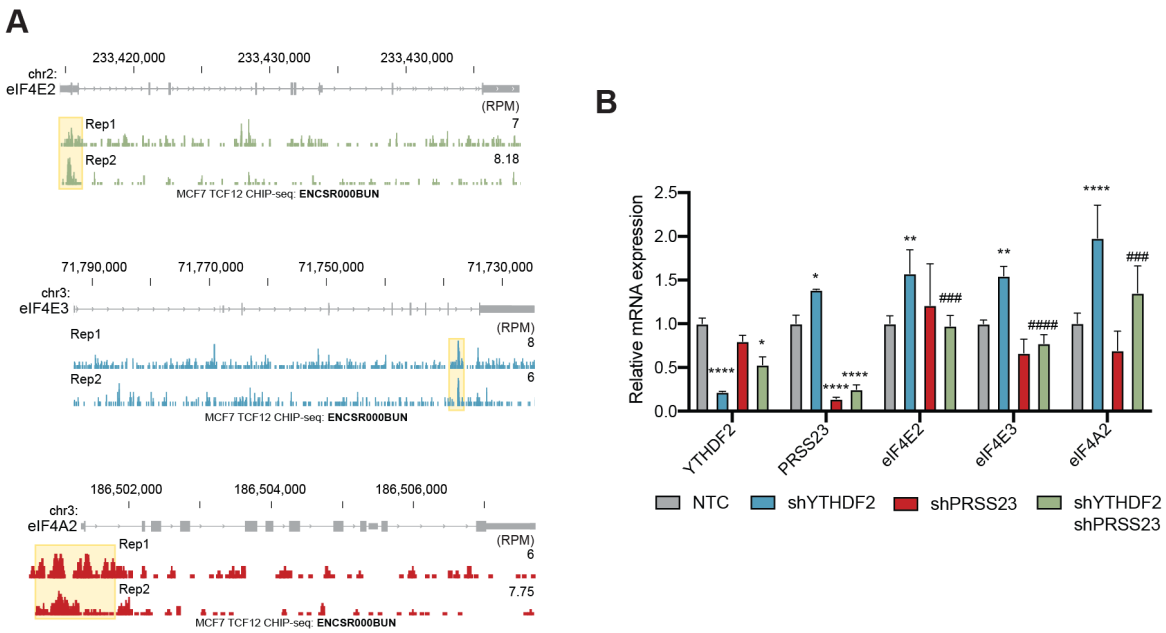

Figure 4.5: **PRSS23 activates TCF12-mediated transcription of cancer lineage-specific transcripts and translation factors.**
(A) Genome browser tracks (human genome build hg19) depicting TCF12 ChIP peaks in MCF-7 cells of translation initiation factors eIF4E2, eIF4E3, and eIF4A2. TCF12 targets were determined by TCF12 CHIP-seq data downloaded from the ENCODE Consortium (ENCSR000BUN). (B) RT-qPCR analysis of mRNA extracted from YTHDF2 and PRSS23 single and double knockdown cells compared to NTC in MDA-MB-231-LM2 cells. Data describes mRNA expression for identified TCF12 direct target genes relative to GAPDH. *$p<0.05$, **$p<0.01$, ****$p<0.0001$, two-way ANOVA test with Dunnett's post-hoc test for multiple comparisons to NTC. ###$p<0.001$, ####$p<0.0001$, two-way ANOVA test with Dunnett's post-hoc test for multiple comparisons to shYTHDF2. Bars are mean $\pm$ SD, n = 3 independent replicates.

Concluding Remarks

Here, I have presented our method for the unbiased identification of YTHDF2 as a therapeutic target for TNBC. Over the past few years, genome-wide CRISPR screens have shown enormous potential for uncovering novel interactions in cancer cells and have lead to the identification of new gene functions including essential growth mediators (T. Hart et al., 2015; J. Shi et al., 2015; Yau et al., 2017) and drug resistance genes (K. Han et al., 2017), and have also enabled study of cancer evolution and the efficacy of immunotherapy through *in vivo* applications (S. Chen et al., 2015; Manguso et al., 2017). The findings from these studies will greatly impact the future of cancer therapy through personalized medicine, however, given the large-scale nature of these studies, many potential candidate genes remain unvalidated and unexplored. While several RBPs have been identified as candidates through these types of screens, functional studies of RBPs in cancer are lacking. Using our RBP-specific CRISPR screen, we have compellingly demonstrated the importance of RBPs regulating all stages of the mRNA life cycle from transcription, capping and polyadenylation, mRNA stability to translation in cancer cells. From our functional studies of YTHDF2 in cancer, we have also shown that drugging RBPs may have reduced side effects on patients compared to currently available options. Our RBP CRISPR screen provides a platform for studying RBPs in cancer with high confidence. I envision that future *in vitro* and *in vivo* studies using this tool will identify new roles for RBPs as essential

growth mediators of cancer cells, RBPs knockouts that enable drug resistance in cancer cells and RBPs that drive metastasis and invasion of cancer cells.

The proto-oncogene, MYC has been studied for decades, and has generally been a difficult drug target due to its role as a transcription factor that regulates normal cell proliferation, metabolism and growth (**Figure 5.1A**), in addition to fueling the increased growth rates of cancer cells (**Figure 5.1B**). Through functional studies, we identified that one of MYC's safeguard mechanisms to limit apoptosis involves upregulating the expression of YTHDF2 to limit the levels of growth promoting mRNAs in the cell, preventing high levels of metabolic stress (**Figure 5.1B**). Since the mechanism by which YTHDF2 depletion triggers apoptosis in MYC-dependent cancer cells involves upregulation of tumorigenic gene expression pathways to overload the cell with oxidative stress (**Figure 5.1C**), further translational studies are essential to assess the ability of YTHDF2-depleted cells to escape the primary tumor and to measure the proportion of cells that undergo cellular senescence rather than apoptosis. Additionally, since we observed increased MYC protein expression in YTHDF2-depleted, MYC-dependent cells, future studies analyzing the required ratio of MYC to YTHDF2 protein expression for induction of apoptosis would inform the expression criteria and appropriateness of targeting YTHDF2 as personalized therapy in individual patients. Such studies would open doors for combinatorial treatment strategies that co-target endoplasmic reticulum stress pathways in cases where cells are MYC-dependent but the ratio of MYC to YTHDF2 protein expression is suboptimal.

Antisense oligonucleotides (ASOs) offer an approach to cancer therapy for targeting genes that are unable to be targeted with small molecules. While ASOs have shown promise in certain localized diseases with the most recent chemistry generation improving upon potency and nucleic acid stability, there have been challenges regarding their use in cancer due to tox-

icity and poor tissue distribution (Gleave & Monia, 2005). As a result, ASOs may not be the best option for treating metastatic cancer where tissue distribution is exceedingly important. Small molecules have been more successful for metastatic cancer therapy, however, there are currently only $\sim$700 approved small molecules, accounting for $<$0.05% of the genome, very few of which target RBPs (Wu, 2020). Recently, fragment-based lead discovery (FBLD) has made it possible to screen low molecular weight compounds or fragments that bind RBPs with known crystal structures (Lamoree & Hubbard, 2017). Fragment hits can be optimized through structure-based design into high affinity compounds that are highly specific to the protein of interest (Lamoree & Hubbard, 2017). The crystal structure of YTHDF2 has been defined for several years now and therefore, YTHDF2 may be a robust candidate for fragment-based screening (T. Zhu et al., 2014). The structure of YTH-domain containing proteins is characterized by a conserved m^6A-binding pocket consisting of several residues that are important for m^6A-RNA recognition (T. Zhu et al., 2014). FBLD was performed recently on YTHDC1, which contains a very similar structure to YTHDF2, and 30 fragments were identified to interact with the -$NHCH_3$ group of m^6A (Bedi et al., 2020). While some fragments showed selectivity to YTHDC1 over other YTH-proteins (Bedi et al., 2020), this study provides motivation for performing structure-based drug design of m^6A-RNA fragments applied to YTHDF2. Additionally, drug screens with Food and Drug Administration (FDA)-approved drug libraries may also provide leads on existing agents that may block m^6A binding and/or identify drugs for combination therapy that sensitize MYC-dependent cells to oxidative stress. In conclusion, while the field of RBP therapeutics is still in its infancy, our work demonstrates the need for widespread discovery of RBP function in disease and motivates translational studies and accelerated drug discovery to target these new prognostic biomarkers for human cancers.

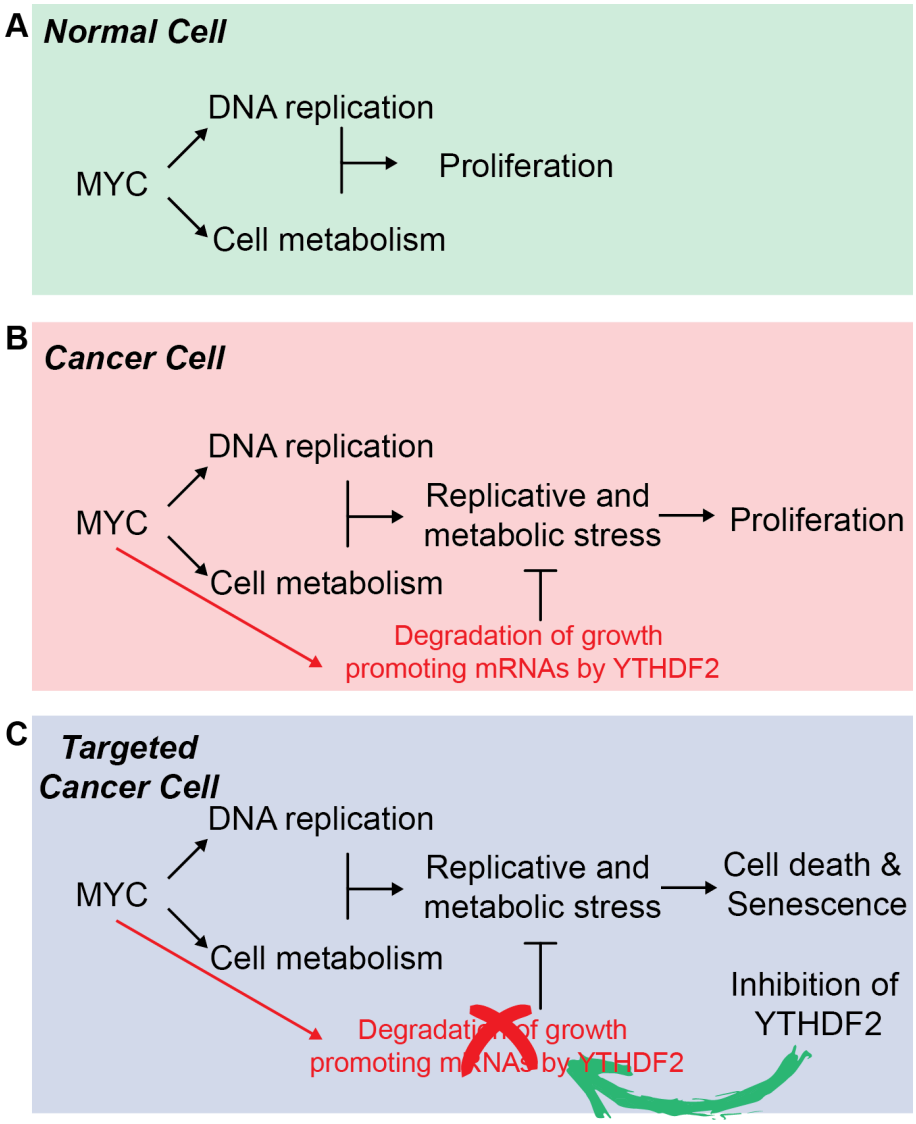

Figure 5.1: **Therapeutic targeting of YTHDF2 in MYC-dependent cancer.**
Schematic describing the functional role of MYC in maintaining (A) normal and (B) cancer cell growth and proliferation and (C) suggestive therapy for MYC-depedent cancers that rely on mRNA turnover to balance increases in cellular stress as a result of increased MYC expression.

Appendix A

Quality Control Metrics

Table A.1: Quality control metrics for eCLIP-seq experiments.

	Initial reads num	**Reads after cutadapt 2**	**Repetitive Reads**	**STAR genome input reads**	**STAR genome uniquely mapped**
LM2_INPUT_1	25892352	23396529	11485334	11911195	7346416
LM2_INPUT_2	21938259	20883650	11262077	9621573	6115466
LM2_IP_1	28224381	27590614	15739260	11851354	3895392
LM2_IP_2	23784145	23595895	13637956	9957939	4785661
MCF7_INPUT_1	23313477	22665388	14998007	7667381	5697141
MCF7_INPUT_2	16241852	15928024	10346146	5581878	4253330
MCF7_IP_1	17163655	15850636	12007630	3843006	3154475
MCF7_IP_2	15364364	14877673	10626692	4250981	3323192
MDA_INPUT_1	23066214	22601002	14759203	7841799	5514689
MDA_INPUT_2	20308334	19520805	12848206	6672599	4603696
MDA_IP_1	16028555	14556023	10770457	3785566	2684143
MDA_IP_2	15864248	15147840	10312034	4835806	3580430
MERA9_INPUT_1	23670932	21897996	13561326	8336670	4918285
MERA9_INPUT_2	27380660	25678791	14245036	11433755	6221864
MERA9_IP_1	20633338	20175415	13177151	6998264	3757730
MERA9_IP_2	25677537	24949939	14908714	10041225	3854438
MERA9_TAM_INPUT_1	27894793	27140394	18146247	8994147	5904148
MERA9_TAM_INPUT_2	28385662	27428845	17197356	10231489	6648376
MERA9_TAM_IP_1	27155644	26600708	18051949	8548759	4586751
MERA9_TAM_IP_2	15892229	14872077	10211869	4660208	1973482
SKBR3_INPUT_1	16250733	16014263	8780310	7233953	5773854
SKBR3_INPUT_2	24662011	24349198	13666086	10683112	8602544
SKBR3_IP_1	25611149	25556984	16843831	8713153	5256512

Continued on next page

Table A.1 - continued from previous page

	STAR genome uniquely mapped %	Number of reads mapped to too many loci	% of reads unmapped: too short	% of reads mapped to too many loci
LM2_INPUT_1	61.68%	764153	22.53%	6.42%
LM2_INPUT_2	63.56%	639149	20.67%	6.64%
LM2_IP_1	32.87%	431125	55.17%	3.64%
LM2_IP_2	48.06%	462757	41.41%	4.65%
MCF7_INPUT_1	74.30%	855552	12.06%	11.16%
MCF7_INPUT_2	76.20%	610652	10.87%	10.94%
MCF7_IP_1	82.08%	317981	8.58%	8.27%
MCF7_IP_2	78.17%	344494	11.67%	8.10%
MDA_INPUT_1	70.32%	848998	15.07%	10.83%
MDA_INPUT_2	68.99%	846848	14.46%	12.69%
MDA_IP_1	70.90%	345147	17.06%	9.12%
MDA_IP_2	74.04%	415159	14.54%	8.59%
MERA9_INPUT_1	59.00%	803728	22.32%	9.64%
MERA9_INPUT_2	54.42%	739990	26.95%	6.47%
MERA9_IP_1	53.70%	366453	35.94%	5.24%
MERA9_IP_2	38.39%	447327	52.37%	4.45%
MERA9_TAM_INPUT_1	65.64%	701317	19.16%	7.80%
MERA9_TAM_INPUT_2	64.98%	817351	19.47%	7.99%
MERA9_TAM_IP_1	53.65%	449184	37.61%	5.25%
MERA9_TAM_IP_2	42.35%	234481	47.30%	5.03%
SKBR3_INPUT_1	79.82%	681555	8.16%	9.42%
SKBR3_INPUT_2	80.52%	1044507	7.52%	9.78%
SKBR3_IP_1	60.33%	518656	30.94%	5.95%
SKBR3_IP_2	60.07%	547685	30.23%	7.03%

Continued on next page

Table A.1 - continued from previous page

	Percent usable / mapped	Percent Usable / Input	Clipper peaks num
LM2_INPUT_1	0.964824889	0.273748982	
LM2_INPUT_2	0.959022256	0.267335161	
LM2_IP_1	0.637603096	0.087998883	62629
LM2_IP_2	0.869588966	0.17497194	107414
MCF7_INPUT_1	0.969017091	0.236799813	
MCF7_INPUT_2	0.973842613	0.255024735	
MCF7_IP_1	0.964933943	0.177343346	86574
MCF7_IP_2	0.947907915	0.205025083	90088
MDA_INPUT_1	0.972876077	0.232595995	
MDA_INPUT_2	0.966858802	0.219177211	
MDA_IP_1	0.910959289	0.15254931	84044
MDA_IP_2	0.943766252	0.213000263	99174
MERA9_INPUT_1	0.930436727	0.193323736	
MERA9_INPUT_2	0.919994073	0.209055516	
MERA9_IP_1	0.704913605	0.128378404	71402
MERA9_IP_2	0.581741359	0.087324808	52770
MERA9_TAM_INPUT_1	0.950073406	0.201090361	
MERA9_TAM_INPUT_2	0.95331311	0.223281176	
MERA9_TAM_IP_1	0.736572576	0.124411522	95872
MERA9_TAM_IP_2	0.430554218	0.053465817	22506
SKBR3_INPUT_1	0.967889039	0.343889103	
SKBR3_INPUT_2	0.97041259	0.338497011	
SKBR3_IP_1	0.868242667	0.17820083	110042
SKBR3_IP_2	0.940828847	0.195927623	108249

Continued on next page

Table A.1 - continued from previous page

	% of reads mapped to multiple loci	% of reads mapped to too many loci	% of reads unmapped: other	% of reads unmapped: too many mismatches	% of reads unmapped: too short
IP_LM2_1	7.03%	0.07%	0.03%	0.00%	2.53%
IP_LM2_2	6.80%	0.06%	0.03%	0.00%	2.55%
IP_MCF7_1	8.35%	0.11%	0.03%	0.00%	0.94%
IP_MCF7_2	9.00%	0.10%	0.03%	0.00%	0.90%
IP_MDA_1	6.43%	0.07%	0.03%	0.00%	5.95%
IP_MDA_2	8.14%	0.06%	0.02%	0.00%	1.02%
IP_Mera9_1	9.07%	0.05%	0.02%	0.00%	0.79%
IP_Mera9_2	9.43%	0.06%	0.02%	0.00%	0.91%
IP_Mera9_Tam_1	9.72%	0.07%	0.02%	0.00%	1.15%
IP_Mera9_Tam_2	9.60%	0.06%	0.02%	0.00%	0.92%
IP_SKBR3_1	10.77%	0.11%	0.01%	0.00%	0.79%
IP_SKBR3_2	12.37%	0.12%	0.02%	0.00%	0.90%
Input_LM2_1	7.64%	0.07%	0.02%	0.00%	1.47%
Input_LM2_2	7.55%	0.07%	0.02%	0.00%	1.58%
Input_MCF7_1	8.83%	0.09%	0.03%	0.00%	2.56%
Input_MCF7_2	8.92%	0.09%	0.03%	0.00%	1.04%
Input_MDA_1	7.49%	0.06%	0.02%	0.00%	3.93%
Input_MDA_2	8.18%	0.07%	0.02%	0.00%	0.81%
Input_Mera9_1	10.08%	0.06%	0.02%	0.00%	0.83%
Input_Mera9_2	9.98%	0.06%	0.02%	0.00%	0.97%
Input_Mera9_Tam_1	10.68%	0.07%	0.02%	0.00%	1.38%
Input_Mera9_Tam_2	10.57%	0.06%	0.02%	0.00%	1.09%
Input_SKBR3_1	11.38%	0.09%	0.02%	0.00%	0.95%
Input_SKBR3_2	13.37%	0.08%	0.01%	0.00%	1.00%

Table A.2: Quality control metrics for m^6A-seq experiments.

	Average input read length	Average mapped length	Deletion average length	Deletion rate per base	Insertion average length	Insertion rate per base
IP_LM2_1	74	74.55	1.66	0.01%	1.38	0.00%
IP_LM2_2	74	74.61	1.65	0.01%	1.37	0.00%
IP_MCF7_1	74	74.59	1.69	0.01%	1.37	0.00%
IP_MCF7_2	74	74.58	1.67	0.01%	1.35	0.00%
IP_MDA_1	74	74.38	1.68	0.00%	1.36	0.00%
IP_MDA_2	74	74.6	1.65	0.01%	1.34	0.00%
IP_Mera9_1	74	74.56	1.65	0.01%	1.35	0.00%
IP_Mera9_2	74	74.54	1.66	0.01%	1.34	0.00%
IP_Mera9_Tam_1	74	74.46	1.69	0.01%	1.3	0.00%
IP_Mera9_Tam_2	74	74.46	1.65	0.00%	1.33	0.00%
IP_SKBR3_1	74	74.63	1.64	0.01%	1.31	0.00%
IP_SKBR3_2	74	74.55	1.71	0.01%	1.3	0.00%
Input_LM2_1	74	74.23	1.67	0.01%	1.32	0.01%
Input_LM2_2	74	74.32	1.66	0.01%	1.29	0.01%
Input_MCF7_1	74	74.39	1.64	0.01%	1.35	0.01%
Input_MCF7_2	74	74.43	1.65	0.01%	1.36	0.01%
Input_MDA_1	74	74.01	1.66	0.01%	1.35	0.00%
Input_MDA_2	74	74.43	1.65	0.01%	1.38	0.00%
Input_Mera9_1	74	74.35	1.65	0.01%	1.34	0.01%
Input_Mera9_2	74	74.27	1.65	0.01%	1.35	0.01%
Input_Mera9_Tam_1	74	74.09	1.64	0.01%	1.25	0.01%
Input_Mera9_Tam_2	74	74.2	1.65	0.01%	1.27	0.01%
Input_SKBR3_1	74	74.48	1.65	0.01%	1.31	0.01%
Input_SKBR3_2	74	74.4	1.67	0.01%	1.32	0.00%

Continued on next page

Table A.2 - continued from previous page

	Mismatch rate per base %	Reads Passing Quality Filter	Number of reads mapped to multiple loci	Number of read mapped to too many loci	Number of splices: AT/AC
IP_LM2_1	0.40%	30948116	2176840	20370	1939
IP_LM2_2	0.40%	40619026	2763182	25693	2495
IP_MCF7_1	0.45%	31466759	2627344	34418	1641
IP_MCF7_2	0.46%	38131397	3431334	39415	1687
IP_MDA_1	1.11%	3395273	218443	2262	192
IP_MDA_2	0.45%	35679943	2905881	22634	1693
IP_Mera9_1	0.41%	29508964	2677377	16130	948
IP_Mera9_2	0.42%	25245357	2379953	14391	760
IP_Mera9_Tam_1	0.42%	33453224	3251034	23053	1147
IP_Mera9_Tam_2	0.41%	17100464	1641285	9432	557
IP_SKBR3_1	0.50%	53797354	5794815	57204	1098
IP_SKBR3_2	0.47%	33785975	4179093	39125	863
Input_LM2_1	0.39%	22097706	1688940	15197	1831
Input_LM2_2	0.39%	28344159	2140269	19328	2469
Input_MCF7_1	0.45%	9946870	878016	8696	510
Input_MCF7_2	0.43%	27089858	2415646	23461	1385
Input_MDA_1	0.81%	2662254	199463	1631	181
Input_MDA_2	0.43%	23072710	1886767	15198	1512
Input_Mera9_1	0.40%	16250973	1637454	10052	708
Input_Mera9_2	0.40%	18028698	1798824	11515	796
Input_Mera9_Tam_1	0.43%	29194402	3117825	20642	1180
Input_Mera9_Tam_2	0.40%	13509876	1428171	8361	602
Input_SKBR3_1	0.46%	14948643	1701121	12741	440
Input_SKBR3_2	0.46%	17030797	2276792	13363	421

Continued on next page

Table A.2 - continued from previous page

	Number of splices: Annotated (sjdb)	Number of splices: GC/AG	Number of splices: GT/AG	Number of splices: Non-canonical	Number of splices: Total
IP_LM2_1	2055699	17448	2065471	1456	2086314
IP_LM2_2	2685578	23118	2699149	1992	2726754
IP_MCF7_1	1849960	19071	1854221	3168	1878101
IP_MCF7_2	1922267	20342	1927498	3310	1952837
IP_MDA_1	198856	1767	199570	190	201719
IP_MDA_2	1970229	16806	1978870	1520	1998889
IP_Mera9_1	1339448	9715	1344758	943	1356364
IP_Mera9_2	1197006	8535	1201954	877	1212126
IP_Mera9_Tam_1	1610444	12692	1616674	1525	1632038
IP_Mera9_Tam_2	740104	5905	743711	522	750695
IP_SKBR3_1	1304254	13097	1317642	1459	1333296
IP_SKBR3_2	961277	9685	969387	1341	981276
Input_LM2_1	1929907	16086	1930144	1221	1949282
Input_LM2_2	2553900	21478	2553640	1703	2579290
Input_MCF7_1	683191	6244	682996	913	690663
Input_MCF7_2	1761691	16410	1760600	2376	1780771
Input_MDA_1	193893	1483	194153	565	196382
Input_MDA_2	1655542	13256	1656166	927	1671861
Input_Mera9_1	929560	6433	929659	528	937328
Input_Mera9_2	1170051	8051	1169757	678	1179282
Input_Mera9_Tam_1	1708425	12111	1709222	1266	1723779
Input_Mera9_Tam_2	745776	5266	746429	468	752765
Input_SKBR3_1	487351	4799	488108	432	493779
Input_SKBR3_2	489681	4657	491313	452	496843

Continued on next page

Table A.2 - continued from previous page

	Uniquely mapped reads %	Uniquely Mapped Reads	repetitive_count
IP_LM2_1	90.34%	27,958,574	5,434,664
IP_LM2_2	90.55%	36,781,298	6,656,749
IP_MCF7_1	90.57%	28,497,910	8,487,654
IP_MCF7_2	89.96%	34,304,481	6,996,054
IP_MDA_1	87.53%	2,971,716	36,275,740
IP_MDA_2	90.75%	32,379,206	4,055,464
IP_Mera9_1	90.06%	26,575,928	2,836,740
IP_Mera9_2	89.59%	22,616,415	2,573,141
IP_Mera9_Tam_1	89.04%	29,786,584	8,403,351
IP_Mera9_Tam_2	89.41%	15,290,043	2,770,400
IP_SKBR3_1	88.32%	47,514,422	6,004,791
IP_SKBR3_2	86.60%	29,257,896	6,516,524
Input_LM2_1	90.80%	20,063,751	12,851,345
Input_LM2_2	90.77%	25,729,304	23,863,095
Input_MCF7_1	88.50%	8,803,316	3,573,861
Input_MCF7_2	89.93%	24,362,601	6,805,874
Input_MDA_1	88.50%	2,356,099	18,083,990
Input_MDA_2	90.93%	20,979,646	3,425,167
Input_Mera9_1	89.01%	14,465,731	2,013,564
Input_Mera9_2	88.97%	16,040,745	2,827,701
Input_Mera9_Tam_1	87.85%	25,646,536	12,124,618
Input_Mera9_Tam_2	88.26%	11,924,213	6,754,794
Input_SKBR3_1	87.57%	13,090,370	5,265,472
Input_SKBR3_2	85.54%	14,567,607	2,744,305

Bibliography

1. M. E., Caflisch, A., & Sledz, P. (2020). Selectively disrupting m(6)A-dependent protein-RNA interactions with fragments. *ACS Chem Biol*.

2. Beroukhim, R., Mermel, C. H., Porter, D., Wei, G., Raychaudhuri, S., Donovan, J., Barretina, J., Boehm, J. S., Dobson, J., Urashima, M., Mc Henry, K. T., Pinchback, R. M., Ligon, A. H., Cho, Y. J., Haery, L., Greulich, H., Reich, M., Winckler, W., Lawrence, M. S., Weir, B. A., Tanaka, K. E., Chiang, D. Y., Bass, A. J., Loo, A., Hoffman, C., Prensner, J., Liefeld, T., Gao, Q., Yecies, D., Signoretti, S., Maher, E., Kaye, F. J., Sasaki, H., Tepper, J. E., Fletcher, J. A., Tabernero, J., Baselga, J., Tsao, M. S., Demichelis, F., Rubin, M. A., Janne, P. A., Daly, M. J., Nucera, C., Levine, R. L., Ebert, B. L., Gabriel, S., Rustgi, A. K., Antonescu, C. R., Ladanyi, M., Letai, A., Garraway, L. A., Loda, M., Beer, D. G., True, L. D., Okamoto, A., Pomeroy, S. L., Singer, S., Golub, T. R., Lander, E. S., Getz, G., Sellers, W. R., & Meyerson, M. (2010). The landscape of somatic copy-number alteration across human cancers. *Nature, 463*(7283), 899-905.

3. Brown, R. V., Danford, F. L., Gokhale, V., Hurley, L. H., & Brooks, T. A. (2011). Demonstration that drug-targeted down-regulation of MYC in non-Hodgkins lymphoma is directly mediated through the promoter G-quadruplex. *J Biol Chem, 286*(47), 41018-41027.

4. Cao, Q., Ma, J., Chen, C. H., Xu, H., Chen, Z., Li, W., & Liu, X. S. (2017). CRISPR-FOCUS: A web server for designing focused CRISPR screening experiments. *PLoS One, 12*(9), e0184281.

5. Chan, H. S., Chang, S. J., Wang, T. Y., Ko, H. J., Lin, Y. C., Lin, K. T., Chang, K. M., & Chuang, Y. J. (2012). Serine protease PRSS23 is upregulated by estrogen receptor alpha and associated with proliferation of breast cancer cells. *PLoS One, 7*(1), e30397.

6. Chen, I. H., Wang, H. H., Hsieh, Y. S., Huang, W. C., Yeh, H. I., & Chuang, Y. J. (2013). PRSS23 is essential for the Snail-dependent endothelial-to-mesenchymal transition during valvulogenesis in zebrafish. *Cardiovasc Res, 97*(3), 443-453.

7. Chen, J., Sun, Y., Xu, X., Wang, D., He, J., Zhou, H., Lu, Y., Zeng, J., Du, F., Gong, A., & Xu, M. (2017). YTH domain family 2 orchestrates epithelial-mesenchymal

transition/proliferation dichotomy in pancreatic cancer cells. *Cell Cycle, 16*(23), 2259-2271.

8. Chen, M., Wei, L., Law, C. T., Tsang, F. H., Shen, J., Cheng, C. L., Tsang, L. H., Ho, D. W., Chiu, D. K., Lee, J. M., Wong, C. C., Ng, I. O., & Wong, C. M. (2018). RNA N6-methyladenosine methyltransferase-like 3 promotes liver cancer progression through YTHDF2-dependent posttranscriptional silencing of SOCS2. *Hepatology, 67*(6), 2254-2270.

9. Chen, S., Sanjana, N. E., Zheng, K., Shalem, O., Lee, K., Shi, X., Scott, D. A., Song, J., Pan, J. Q., Weissleder, R., Lee, H., Zhang, F., & Sharp, P. A. (2015). Genome-wide CRISPR screen in a mouse model of tumor growth and metastasis. *Cell, 160*(6), 1246-1260.

10. Cho, S. W., Kim, S., Kim, J. M., & Kim, J. S. (2013). Targeted genome engineering in human cells with the Cas9 RNA-guided endonuclease. *Nat Biotechnol, 31*(3), 230-232.

11. Cobbold, L. C., Wilson, L. A., Sawicka, K., King, H. A., Kondrashov, A. V., Spriggs, K. A., Bushell, M., & Willis, A. E. (2010). Upregulated c-myc expression in multiple myeloma by internal ribosome entry results from increased interactions with and expression of PTB-1 and YB-1. *Oncogene, 29*(19), 2884-2891.

12. Cole, M. D., & Cowling, V. H. (2008). Transcription-independent functions of MYC: regulation of translation and DNA replication. *Nat Rev Mol Cell Biol, 9*(10), 810-815.

13. Cole, M. P., Jones, C. T., & Todd, I. D. (1971). A new anti-oestrogenic agent in late breast cancer. An early clinical appraisal of ICI46474. *Br J Cancer, 25*(2), 270-275.

14. Cubillos-Ruiz, J. R., Bettigole, S. E., & Glimcher, L. H. (2017). Tumorigenic and Immunosuppressive Effects of Endoplasmic Reticulum Stress in Cancer. *Cell, 168*(4), 692-706.

15. Dang, C. V. (2012). MYC on the path to cancer. *Cell, 149*(1), 22-35.

16. Darling, N. J., & Cook, S. J. (2014). The role of MAPK signalling pathways in the response to endoplasmic reticulum stress. *Biochim Biophys Acta, 1843*(10), 2150-2163.

17. Deng, X., Su, R., Feng, X., Wei, M., & Chen, J. (2018). Role of N(6)-methyladenosine modification in cancer. *Curr Opin Genet Dev, 48*, 1-7.

18. Dent, R., Trudeau, M., Pritchard, K. I., Hanna, W. M., Kahn, H. K., Sawka, C. A., Lickley, L. A., Rawlinson, E., Sun, P., & Narod, S. A. (2007). Triple-negative breast cancer: clinical features and patterns of recurrence. *Clin Cancer Res, 13*(15 Pt 1), 4429-4434.

19. Dey, S., Tameire, F., & Koumenis, C. (2013). PERK-ing up autophagy during MYC-induced tumorigenesis. *Autophagy, 9*(4), 612-614.

20. Dobin, A., Davis, C. A., Schlesinger, F., Drenkow, J., Zaleski, C., Jha, S., Batut, P., Chaisson, M., & Gingeras, T. R. (2013). STAR: ultrafast universal RNA-seq aligner. *Bioinformatics, 29*(1), 15-21.

21. Doench, J. G., Hartenian, E., Graham, D. B., Tothova, Z., Hegde, M., Smith, I., Sullender, M., Ebert, B. L., Xavier, R. J., & Root, D. E. (2014). Rational design of highly active sgRNAs for CRISPR-Cas9-mediated gene inactivation. *Nat Biotechnol, 32*(12), 1262-1267.

22. Dominissini, D., Moshitch-Moshkovitz, S., Salmon-Divon, M., Amariglio, N., & Rechavi, G. (2013). Transcriptome-wide mapping of N(6)-methyladenosine by m(6)A-seq based on immunocapturing and massively parallel sequencing. *Nat Protoc, 8*(1), 176-189.

23. Du, H., Zhao, Y., He, J., Zhang, Y., Xi, H., Liu, M., Ma, J., & Wu, L. (2016). YTHDF2 destabilizes m(6)A-containing RNA through direct recruitment of the CCR4-NOT deadenylase complex. *Nat Commun, 7*, 12626.

24. Eden, E., Navon, R., Steinfeld, I., Lipson, D., & Yakhini, Z. (2009). GOrilla: a tool for discovery and visualization of enriched GO terms in ranked gene lists. *BMC Bioinformatics, 10*, 48.

25. Fang, M. Y., Markmiller, S., Vu, A. Q., Javaherian, A., Dowdle, W. E., Jolivet, P., Bushway, P. J., Castello, N. A., Baral, A., Chan, M. Y., Linsley, J. W., Linsley, D., Mercola, M., Finkbeiner, S., Lecuyer, E., Lewcock, J. W., & Yeo, G. W. (2019). Small-Molecule Modulation of TDP-43 Recruitment to Stress Granules Prevents Persistent TDP-43 Accumulation in ALS/FTD. *Neuron, 103*(5), 802-819 e811.

26. Feng, Y. X., Sokol, E. S., Del Vecchio, C. A., Sanduja, S., Claessen, J. H., Proia, T. A., Jin, D. X., Reinhardt, F., Ploegh, H. L., Wang, Q., & Gupta, P. B. (2014). Epithelial-to-mesenchymal transition activates PERK-eIF2alpha and sensitizes cells to endoplasmic reticulum stress. *Cancer Discov, 4*(6), 702-715.

27. Genuth, N. R., & Barna, M. (2018). Heterogeneity and specialized functions of translation machinery: from genes to organisms. *Nat Rev Genet, 19*(7), 431-452.

28. Gerstberger, S., Hafner, M., & Tuschl, T. (2014). A census of human RNA-binding proteins. *Nat Rev Genet, 15*(12), 829-845.

29. Geula, S., Moshitch-Moshkovitz, S., Dominissini, D., Mansour, A. A., Kol, N., Salmon-Divon, M., Hershkovitz, V., Peer, E., Mor, N., Manor, Y. S., Ben-Haim, M. S., Eyal, E., Yunger, S., Pinto, Y., Jaitin, D. A., Viukov, S., Rais, Y., Krupalnik, V., Chomsky, E., Zerbib, M., Maza, I., Rechavi, Y., Massarwa, R., Hanna, S., Amit, I., Levanon, E. Y., Amariglio, N., Stern-Ginossar, N., Novershtern, N., Rechavi, G., & Hanna, J. H. (2015). m6A mRNA methylation facilitates resolution of naive pluripotency toward differentiation. *Science, 347*(6225), 1002-1006.

30. Giese, A., Loo, M. A., Tran, N., Haskett, D., Coons, S. W., & Berens, M. E. (1996). Dichotomy of astrocytoma migration and proliferation. *International Journal of Cancer, 67*(2), 275-282.

31. Gleave, M. E., & Monia, B. P. (2005). Antisense therapy for cancer. *Nat Rev Cancer, 5*(6), 468-479.

32. Green, A. R., Aleskandarany, M. A., Agarwal, D., Elsheikh, S., Nolan, C. C., Diez-Rodriguez, M., Macmillan, R. D., Ball, G. R., Caldas, C., Madhusudan, S., Ellis, I. O., & Rakha, E. A. (2016). MYC functions are specific in biological subtypes of breast cancer and confers resistance to endocrine therapy in luminal tumours. *Br J Cancer, 114*(8), 917-928.

33. Han, B., Yang, Y., Chen, J., He, X., Lv, N., & Yan, R. (2019). PRSS23 knockdown inhibits gastric tumorigenesis through EIF2 signaling. *Pharmacol Res, 142*, 50-57.

34. Han, K., Jeng, E. E., Hess, G. T., Morgens, D. W., Li, A., & Bassik, M. C. (2017). Synergistic drug combinations for cancer identified in a CRISPR screen for pairwise genetic interactions. *Nat Biotechnol, 35*(5), 463-474.

35. Handa, T., Katayama, A., Yokobori, T., Yamane, A., Fujii, T., Obayashi, S., Kurozumi, S., Kawabata-Iwakawa, R., Gombodorj, N., Nishiyama, M., Asao, T., Shirabe, K., Kuwano, H., & Oyama, T. (2019). Carboxypeptidase A4 accumulation is associated with an aggressive phenotype and poor prognosis in triple-negative breast cancer. *Int J Oncol, 54*(3), 833-844.

36. Hart, L. S., Cunningham, J. T., Datta, T., Dey, S., Tameire, F., Lehman, S. L., Qiu, B., Zhang, H., Cerniglia, G., Bi, M., Li, Y., Gao, Y., Liu, H., Li, C., Maity, A., Thomas-Tikhonenko, A., Perl, A. E., Koong, A., Fuchs, S. Y., Diehl, J. A., Mills, I. G., Ruggero, D., & Koumenis, C. (2012). ER stress-mediated autophagy promotes Myc-dependent transformation and tumor growth. *J Clin Invest, 122*(12), 4621-4634.

37. Hart, T., Chandrashekhar, M., Aregger, M., Steinhart, Z., Brown, K. R., MacLeod, G., Mis, M., Zimmermann, M., Fradet-Turcotte, A., Sun, S., Mero, P., Dirks, P., Sidhu, S., Roth, F. P., Rissland, O. S., Durocher, D., Angers, S., & Moffat, J. (2015). High-Resolution CRISPR Screens Reveal Fitness Genes and Genotype-Specific Cancer Liabilities. *Cell, 163*(6), 1515-1526.

38. He, X., Arslan, A. D., Ho, T. T., Yuan, C., Stampfer, M. R., & Beck, W. T. (2014). Involvement of polypyrimidine tract-binding protein (PTBP1) in maintaining breast cancer cell growth and malignant properties. *Oncogenesis, 3*, e84.

39. Heinz, S., Benner, C., Spann, N., Bertolino, E., Lin, Y. C., Laslo, P., Cheng, J. X., Murre, C., Singh, H., & Glass, C. K. (2010). Simple combinations of lineage-determining transcription factors prime cis-regulatory elements required for macrophage and B cell identities. *Mol Cell, 38*(4), 576-589.

40. Hentze, M. W., Castello, A., Schwarzl, T., & Preiss, T. (2018). A brave new world of RNA-binding proteins. *Nat Rev Mol Cell Biol, 19*(5), 327-341.

41. Horiuchi, D., Kusdra, L., Huskey, N. E., Chandriani, S., Lenburg, M. E., Gonzalez-Angulo, A. M., Creasman, K. J., Bazarov, A. V., Smyth, J. W., Davis, S. E., Yaswen, P., Mills, G.

B., Esserman, L. J., & Goga, A. (2012). MYC pathway activation in triple-negative breast cancer is synthetic lethal with CDK inhibition. *J Exp Med, 209*(4), 679-696.

42. Hsu, T. Y., Simon, L. M., Neill, N. J., Marcotte, R., Sayad, A., Bland, C. S., Echeverria, G. V., Sun, T., Kurley, S. J., Tyagi, S., Karlin, K. L., Dominguez-Vidana, R., Hartman, J. D., Renwick, A., Scorsone, K., Bernardi, R. J., Skinner, S. O., Jain, A., Orellana, M., Lagisetti, C., Golding, I., Jung, S. Y., Neilson, J. R., Zhang, X. H., Cooper, T. A., Webb, T. R., Neel, B. G., Shaw, C. A., & Westbrook, T. F. (2015). The spliceosome is a therapeutic vulnerability in MYC-driven cancer. *Nature, 525*(7569), 384-388.

43. Huang, H., Weng, H., Sun, W., Qin, X., Shi, H., Wu, H., Zhao, B. S., Mesquita, A., Liu, C., Yuan, C. L., Hu, Y. C., Huttelmaier, S., Skibbe, J. R., Su, R., Deng, X., Dong, L., Sun, M., Li, C., Nachtergaele, S., Wang, Y., Hu, C., Ferchen, K., Greis, K. D., Jiang, X., Wei, M., Qu, L., Guan, J. L., He, C., Yang, J., & Chen, J. (2018). Recognition of RNA N(6)-methyladenosine by IGF2BP proteins enhances mRNA stability and translation. *Nat Cell Biol, 20*(3), 285-295.

44. Ivanova, I., Much, C., Di Giacomo, M., Azzi, C., Morgan, M., Moreira, P. N., Monahan, J., Carrieri, C., Enright, A. J., & O'Carroll, D. (2017). The RNA m(6)A Reader YTHDF2 Is Essential for the Post-transcriptional Regulation of the Maternal Transcriptome and Oocyte Competence. *Mol Cell, 67*(6), 1059-1067 e1054.

45. Jackson, A. L., Bartz, S. R., Schelter, J., Kobayashi, S. V., Burchard, J., Mao, M., Li, B., Cavet, G., & Linsley, P. S. (2003). Expression profiling reveals off-target gene regulation by RNAi. *Nat Biotechnol, 21*(6), 635-637.

46. Jia, G., Fu, Y., Zhao, X., Dai, Q., Zheng, G., Yang, Y., Yi, C., Lindahl, T., Pan, T., Yang, Y. G., & He, C. (2011). N6-methyladenosine in nuclear RNA is a major substrate of the obesity-associated FTO. *Nat Chem Biol, 7*(12), 885-887.

47. Kessler, J. D., Kahle, K. T., Sun, T., Meerbrey, K. L., Schlabach, M. R., Schmitt, E. M., Skinner, S. O., Xu, Q., Li, M. Z., Hartman, Z. C., Rao, M., Yu, P., Dominguez-Vidana, R., Liang, A. C., Solimini, N. L., Bernardi, R. J., Yu, B., Hsu, T., Golding, I., Luo, J., Osborne, C. K., Creighton, C. J., Hilsenbeck, S. G., Schiff, R., Shaw, C. A., Elledge, S. J., & Westbrook, T. F. (2012). A SUMOylation-dependent transcriptional subprogram is required for Myc-driven tumorigenesis. *Science, 335*(6066), 348-353.

48. Klefstrom, J., Västrik, I., Saksela, E., Valle, J., Eilers, M., & Alitalo, K. (1994). c-Myc induces cellular susceptibility to the cytotoxic action of TNF-alpha. *The EMBO Journal, 13*(22), 5442-5450.

49. Kress, T. R., Sabo, A., & Amati, B. (2015). MYC: connecting selective transcriptional control to global RNA production. *Nat Rev Cancer, 15*(10), 593-607.

50. Lafon, I., Carballes, F., Brewer, G., Poiret, M., & Morello, D. (1998). Developmental expression of AUF1 and HuR, two c-myc mRNA binding proteins. *Oncogene, 16*(26), 3413-3421.

51. Lambert, N., Robertson, A., Jangi, M., McGeary, S., Sharp, P. A., & Burge, C. B. (2014). RNA Bind-n-Seq: quantitative assessment of the sequence and structural binding specificity of RNA binding proteins. *Mol Cell, 54*(5), 887-900.

52. Lamoree, B., & Hubbard, R. E. (2017). Current perspectives in fragment-based lead discovery (FBLD). *Essays Biochem, 61*(5), 453-464.

53. Lan, Q., Liu, P. Y., Haase, J., Bell, J. L., Huttelmaier, S., & Liu, T. (2019). The Critical Role of RNA m(6)A Methylation in Cancer. *Cancer Res, 79*(7), 1285-1292.

54. Langmead, B., & Salzberg, S. L. (2012). Fast gapped-read alignment with Bowtie 2. *Nat Methods, 9*(4), 357-359.

55. Li, B., & Dou, Q. P. (2000). Bax degradation by the ubiquitin/proteasome-dependent pathway: involvement in tumor survival and progression. *Proc Natl Acad Sci U S A, 97*(8), 3850-3855.

56. Li, M., Zhao, X., Wang, W., Shi, H., Pan, Q., Lu, Z., Perez, S. P., Suganthan, R., He, C., Bjoras, M., & Klungland, A. (2018). Ythdf2-mediated m(6)A mRNA clearance modulates neural development in mice. *Genome Biol, 19*(1), 69.

57. Li, W., Koster, J., Xu, H., Chen, C. H., Xiao, T., Liu, J. S., Brown, M., & Liu, X. S. (2015). Quality control, modeling, and visualization of CRISPR screens with MAGeCK-VISPR. *Genome Biol, 16*, 281.

58. Li, Z., Qian, P., Shao, W., Shi, H., He, X. C., Gogol, M., Yu, Z., Wang, Y., Qi, M., Zhu, Y., Perry, J. M., Zhang, K., Tao, F., Zhou, K., Hu, D., Han, Y., Zhao, C., Alexander, R., Xu, H., Chen, S., Peak, A., Hall, K., Peterson, M., Perera, A., Haug, J. S., Parmely, T., Li, H., Shen, B., Zeitlinger, J., He, C., & Li, L. (2018). Suppression of m(6)A reader Ythdf2 promotes hematopoietic stem cell expansion. *Cell Res, 28*(9), 904-917.

59. Liao, B., Hu, Y., & Brewer, G. (2007). Competitive binding of AUF1 and TIAR to MYC mRNA controls its translation. *Nat Struct Mol Biol, 14*(6), 511-518.

60. Lin, S., Choe, J., Du, P., Triboulet, R., & Gregory, R. I. (2016). The m(6)A Methyltransferase METTL3 Promotes Translation in Human Cancer Cells. *Mol Cell, 62*(3), 335-345.

61. Linder, B., Grozhik, A. V., Olarerin-George, A. O., Meydan, C., Mason, C. E., & Jaffrey, S. R. (2015). Single-nucleotide-resolution mapping of m6A and m6Am throughout the transcriptome. *Nat Methods, 12*(8), 767-772.

62. Liu, J., Lichtenberg, T., Hoadley, K. A., Poisson, L. M., Lazar, A. J., Cherniack, A. D., Kovatich, A. J., Benz, C. C., Levine, D. A., Lee, A. V., Omberg, L., Wolf, D. M., Shriver, C. D., Thorsson, V., Cancer Genome Atlas Research, N., & Hu, H. (2018). An Integrated TCGA Pan-Cancer Clinical Data Resource to Drive High-Quality Survival Outcome Analytics. *Cell, 173*(2), 400-416 e411.

63. Love, M. I., Huber, W., & Anders, S. (2014). Moderated estimation of fold change and dispersion for RNA-seq data with DESeq2. *Genome Biol, 15*(12), 550.

64. Lu, M., Lawrence, D. A., Marsters, S., Acosta-Alvear, D., Kimmig, P., Mendez, A. S., Paton, A. W., Paton, J. C., Walter, P., & Ashkenazi, A. (2014). Opposing unfolded-protein-response signals converge on death receptor 5 to control apoptosis. *Science, 345*(6192), 98-101.

65. Mali, P., Yang, L., Esvelt, K. M., Aach, J., Guell, M., DiCarlo, J. E., Norville, J. E., & Church, G. M. (2013). RNA-guided human genome engineering via Cas9. *Science, 339*(6121), 823-826.

66. Manguso, R. T., Pope, H. W., Zimmer, M. D., Brown, F. D., Yates, K. B., Miller, B. C., Collins, N. B., Bi, K., LaFleur, M. W., Juneja, V. R., Weiss, S. A., Lo, J., Fisher, D. E., Miao, D., Van Allen, E., Root, D. E., Sharpe, A. H., Doench, J. G., & Haining, W. N. (2017). In vivo CRISPR screening identifies Ptpn2 as a cancer immunotherapy target. *Nature, 547*(7664), 413-418.

67. Marderosian, M., Sharma, A., Funk, A. P., Vartanian, R., Masri, J., Jo, O. D., & Gera, J. F. (2006). Tristetraprolin regulates Cyclin D1 and c-Myc mRNA stability in response to rapamycin in an Akt-dependent manner via p38 MAPK signaling. *Oncogene, 25*(47), 6277-6290.

68. Martin, M. (2011). Cutadapt removes adapter sequences from high-throughput sequencing reads. *EMBnet.journal, 17*(1).

69. Marvel, C. C., Del Rowe, J., Bremer, E. G., & Moskal, J. R. (1994). Altered RNA turnover in carcinogenesis. The diagnostic potential of modified base excretion. *Mol Chem Neuropathol, 21*(2-3), 353-368.

70. Masciadri, B., Areces, L. B., Carpinelli, P., Foiani, M., Draetta, G., & Fiore, F. (2004). Characterization of the BUD31 gene of Saccharomyces cerevisiae. *Biochem Biophys Res Commun, 320*(4), 1342-1350.

71. Mayr, C., & Bartel, D. P. (2009). Widespread shortening of 3'UTRs by alternative cleavage and polyadenylation activates oncogenes in cancer cells. *Cell, 138*(4), 673-684.

72. Mertins, P., Mani, D. R., Ruggles, K. V., Gillette, M. A., Clauser, K. R., Wang, P., Wang, X., Qiao, J. W., Cao, S., Petralia, F., Kawaler, E., Mundt, F., Krug, K., Tu, Z., Lei, J. T., Gatza, M. L., Wilkerson, M., Perou, C. M., Yellapantula, V., Huang, K. L., Lin, C., McLellan, M. D., Yan, P., Davies, S. R., Townsend, R. R., Skates, S. J., Wang, J., Zhang, B., Kinsinger, C. R., Mesri, M., Rodriguez, H., Ding, L., Paulovich, A. G., Fenyo, D., Ellis, M. J., Carr, S. A., & Nci, C. (2016). Proteogenomics connects somatic mutations to signalling in breast cancer. *Nature, 534*(7605), 55-62.

73. Meyer, K. D., Saletore, Y., Zumbo, P., Elemento, O., Mason, C. E., & Jaffrey, S. R. (2012). Comprehensive analysis of mRNA methylation reveals enrichment in 3' UTRs and near stop codons. *Cell, 149*(7), 1635-1646.

74. Morgens, D. W., Deans, R. M., Li, A., & Bassik, M. C. (2016). Systematic comparison of CRISPR/Cas9 and RNAi screens for essential genes. *Nat Biotechnol, 34*(6), 634-636.

75. Nilsson, J. A., & Cleveland, J. L. (2003). Myc pathways provoking cell suicide and cancer. *Oncogene, 22*(56), 9007-9021.

76. Okada, T., Haze, K., Nadanaka, S., Yoshida, H., Seidah, N. G., Hirano, Y., Sato, R., Negishi, M., & Mori, K. (2003). A serine protease inhibitor prevents endoplasmic reticulum stress-induced cleavage but not transport of the membrane-bound transcription factor ATF6. *J Biol Chem, 278*(33), 31024-31032.

77. Olarerin-George, A. O., & Jaffrey, S. R. (2017). MetaPlotR: a Perl/R pipeline for plotting metagenes of nucleotide modifications and other transcriptomic sites. *Bioinformatics, 33*(10), 1563-1564.

78. Ou, T. M., Lu, Y. J., Zhang, C., Huang, Z. S., Wang, X. D., Tan, J. H., Chen, Y., Ma, D. L., Wong, K. Y., Tang, J. C., Chan, A. S., & Gu, L. Q. (2007). Stabilization of G-quadruplex DNA and down-regulation of oncogene c-myc by quindoline derivatives. *J Med Chem, 50*(7), 1465-1474.

79. Paris, J., Morgan, M., Campos, J., Spencer, G. J., Shmakova, A., Ivanova, I., Mapperley, C., Lawson, H., Wotherspoon, D. A., Sepulveda, C., Vukovic, M., Allen, L., Sarapuu, A., Tavosanis, A., Guitart, A. V., Villacreces, A., Much, C., Choe, J., Azar, A., van de Lagemaat, L. N., Vernimmen, D., Nehme, A., Mazurier, F., Somervaille, T. C. P., Gregory, R. I., O'Carroll, D., & Kranc, K. R. (2019). Targeting the RNA m(6)A Reader YTHDF2 Selectively Compromises Cancer Stem Cells in Acute Myeloid Leukemia. *Cell Stem Cell, 25*(1), 137-148 e136.

80. Park, S., Brugiolo, M., Akerman, M., Das, S., Urbanski, L., Geier, A., Kesarwani, A. K., Fan, M., Leclair, N., Lin, K. T., Hu, L., Hua, I., George, J., Muthuswamy, S. K., Krainer, A. R., & Anczukow, O. (2019). Differential Functions of Splicing Factors in Mammary Transformation and Breast Cancer Metastasis. *Cell Rep, 29*(9), 2672-2688 e2677.

81. Peng, J., Zhou, Y., Zhu, S., & Wei, W. (2015). High-throughput screens in mammalian cells using the CRISPR-Cas9 system. *FEBS J, 282*(11), 2089-2096.

82. Pereira, B., Billaud, M., & Almeida, R. (2017). RNA-Binding Proteins in Cancer: Old Players and New Actors. *Trends Cancer, 3*(7), 506-528.

83. Perry, R. P., & Kelley, D. E. (1974). Existence of methylated messenger RNA in mouse L cells. *Cell, 1*(1), 37-42.

84. Rakha, E. A., Reis-Filho, J. S., & Ellis, I. O. (2008). Basal-like breast cancer: a critical review. *J Clin Oncol, 26*(15), 2568-2581.

85. Rao, R. V., & Bredesen, D. E. (2004). Misfolded proteins, endoplasmic reticulum stress and neurodegeneration. *Curr Opin Cell Biol, 16*(6), 653-662.

86. Rao, R. V., Hermel, E., Castro-Obregon, S., del Rio, G., Ellerby, L. M., Ellerby, H. M., & Bredesen, D. E. (2001). Coupling endoplasmic reticulum stress to the cell death program. Mechanism of caspase activation. *J Biol Chem, 276*(36), 33869-33874.

87. Ries, R. J., Zaccara, S., Klein, P., Olarerin-George, A., Namkoong, S., Pickering, B. F., Patil, D. P., Kwak, H., Lee, J. H., & Jaffrey, S. R. (2019). m6A enhances the phase separation potential of mRNA. *Nature*.

88. Schneider, P., Thome, M., Burns, K., Bodmer, J.-L., Hofmann, K., Kataoka, T., Holler, N., & Tschopp, J. (1997). TRAIL Receptors 1 (DR4) and 2 (DR5) Signal FADD-Dependent Apoptosis and Activate NF-κB. *Immunity, 7*(6), 831-836.

89. Sebestyen, E., Singh, B., Minana, B., Pages, A., Mateo, F., Pujana, M. A., Valcarcel, J., & Eyras, E. (2016). Large-scale analysis of genome and transcriptome alterations in multiple tumors unveils novel cancer-relevant splicing networks. *Genome Res, 26*(6), 732-744.

90. Seibler, J., Kuter-Luks, B., Kern, H., Streu, S., Plum, L., Mauer, J., Kuhn, R., Bruning, J. C., & Schwenk, F. (2005). Single copy shRNA configuration for ubiquitous gene knockdown in mice. *Nucleic Acids Res, 33*(7), e67.

91. Shalem, O., Sanjana, N. E., Hartenian, E., Shi, X., Scott, D. A., Mikkelson, T., Heckl, D., Ebert, B. L., Root, D. E., Doench, J. G., & Zhang, F. (2014). Genome-scale CRISPR-Cas9 knockout screening in human cells. *Science, 343*(6166), 84-87.

92. Shi, H., Wang, X., Lu, Z., Zhao, B. S., Ma, H., Hsu, P. J., Liu, C., & He, C. (2017). YTHDF3 facilitates translation and decay of N(6)-methyladenosine-modified RNA. *Cell Res, 27*(3), 315-328.

93. Shi, J., Wang, E., Milazzo, J. P., Wang, Z., Kinney, J. B., & Vakoc, C. R. (2015). Discovery of cancer drug targets by CRISPR-Cas9 screening of protein domains. *Nat Biotechnol, 33*(6), 661-667.

94. Shi, Y., Vattem, K. M., Sood, R., An, J., Liang, J., Stramm, L., & Wek, R. C. (1998). Identification and characterization of pancreatic eukaryotic initiation factor 2 alpha-subunit kinase, PEK, involved in translational control. *Mol Cell Biol, 18*(12), 7499-7509.

95. Smith, R. A., Miller, T. M., Yamanaka, K., Monia, B. P., Condon, T. P., Hung, G., Lobsiger, C. S., Ward, C. M., McAlonis-Downes, M., Wei, H., Wancewicz, E. V., Bennett, C. F., & Cleveland, D. W. (2006). Antisense oligonucleotide therapy for neurodegenerative disease. *J Clin Invest, 116*(8), 2290-2296.

96. Soucie, E. L., Annis, M. G., Sedivy, J., Filmus, J., Leber, B., Andrews, D. W., & Penn, L. Z. (2001). Myc potentiates apoptosis by stimulating Bax activity at the mitochondria. *Mol Cell Biol, 21*(14), 4725-4736.

97. Stelzl, U., Worm, U., Lalowski, M., Haenig, C., Brembeck, F. H., Goehler, H., Stroedicke, M., Zenkner, M., Schoenherr, A., Koeppen, S., Timm, J., Mintzlaff, S., Abraham, C., Bock, N., Kietzmann, S., Goedde, A., Toksoz, E., Droege, A., Krobitsch, S., Korn, B., Birchmeier,

W., Lehrach, H., & Wanker, E. E. (2005). A human protein-protein interaction network: a resource for annotating the proteome. *Cell, 122*(6), 957-968.

98. Sternberg, S. H., Redding, S., Jinek, M., Greene, E. C., & Doudna, J. A. (2014). DNA interrogation by the CRISPR RNA-guided endonuclease Cas9. *Nature, 507*(7490), 62-67.

99. Su, R., Dong, L., Li, C., Nachtergaele, S., Wunderlich, M., Qing, Y., Deng, X., Wang, Y., Weng, X., Hu, C., Yu, M., Skibbe, J., Dai, Q., Zou, D., Wu, T., Yu, K., Weng, H., Huang, H., Ferchen, K., Qin, X., Zhang, B., Qi, J., Sasaki, A. T., Plas, D. R., Bradner, J. E., Wei, M., Marcucci, G., Jiang, X., Mulloy, J. C., Jin, J., He, C., & Chen, J. (2018). R-2HG Exhibits Anti-tumor Activity by Targeting FTO/m(6)A/MYC/CEBPA Signaling. *Cell, 172*(1-2), 90-105 e123.

100. Tanabe, L. M., & List, K. (2017). The role of type II transmembrane serine protease-mediated signaling in cancer. *FEBS J, 284*(10), 1421-1436.

101. Tu, W. B., Helander, S., Pilstal, R., Hickman, K. A., Lourenco, C., Jurisica, I., Raught, B., Wallner, B., Sunnerhagen, M., & Penn, L. Z. (2015). Myc and its interactors take shape. *Biochim Biophys Acta, 1849*(5), 469-483.

102. Tuck, M. T., James, C. B. L., Kelder, B., & Kopchick, J. J. (1996). Elevation of internal 6-methyladenine mRNA methyltransferase activity after cellular transformation. *Cancer Letters, 103*(1), 107-113.

103. Uniacke, J., Holterman, C. E., Lachance, G., Franovic, A., Jacob, M. D., Fabian, M. R., Payette, J., Holcik, M., Pause, A., & Lee, S. (2012). An oxygen-regulated switch in the protein synthesis machinery. *Nature, 486*(7401), 126-129.

104. Urano, F., Wang, X., Bertolotti, A., Zhang, Y., Chung, P., Harding, H. P., & Ron, D. (2000). Coupling of stress in the ER to activation of JNK protein kinases by transmembrane protein kinase IRE1. *Science, 287*(5453), 664-666.

105. Van Nostrand, E. L., Nguyen, T. B., Gelboin-Burkhart, C., Wang, R., Blue, S. M., Pratt, G. A., Louie, A. L., & Yeo, G. W. (2017). *Robust, Cost-Effective Profiling of RNA Binding Protein Targets with Single-end Enhanced Crosslinking and Immunoprecipitation (seCLIP). In: Shi Y. (eds) mRNA Processing. Methods in Molecular Biology* (Vol. 1648). New York, NY: Humana Press.

106. Van Nostrand, E. L., Pratt, G. A., Shishkin, A. A., Gelboin-Burkhart, C., Fang, M. Y., Sundararaman, B., Blue, S. M., Nguyen, T. B., Surka, C., Elkins, K., Stanton, R., Rigo, F., Guttman, M., & Yeo, G. W. (2016). Robust transcriptome-wide discovery of RNA-binding protein binding sites with enhanced CLIP (eCLIP). *Nat Methods, 13*(6), 508-514.

107. van Riggelen, J., Yetil, A., & Felsher, D. W. (2010). MYC as a regulator of ribosome biogenesis and protein synthesis. *Nat Rev Cancer, 10*(4), 301-309.

108. Vincent, T., Neve, E. P., Johnson, J. R., Kukalev, A., Rojo, F., Albanell, J., Pietras, K., Virtanen, I., Philipson, L., Leopold, P. L., Crystal, R. G., de Herreros, A. G., Moustakas, A., Pettersson, R. F., & Fuxe, J. (2009). A SNAIL1-SMAD3/4 transcriptional repressor

complex promotes TGF-beta mediated epithelial-mesenchymal transition. *Nat Cell Biol, 11*(8), 943-950.

109. Vogelstein, B., Papadopoulos, N., Velculescu, V. E., Zhou, S., Diaz, L. A., Jr., & Kinzler, K. W. (2013). Cancer genome landscapes. *Science, 339*(6127), 1546-1558.

110. Vu, L. P., Pickering, B. F., Cheng, Y., Zaccara, S., Nguyen, D., Minuesa, G., Chou, T., Chow, A., Saletore, Y., MacKay, M., Schulman, J., Famulare, C., Patel, M., Klimek, V. M., Garrett-Bakelman, F. E., Melnick, A., Carroll, M., Mason, C. E., Jaffrey, S. R., & Kharas, M. G. (2017). The N(6)-methyladenosine (m(6)A)-forming enzyme METTL3 controls myeloid differentiation of normal hematopoietic and leukemia cells. *Nat Med, 23*(11), 1369-1376.

111. Wan, C., Gong, C., Zhang, H., Hua, L., Li, X., Chen, X., Chen, Y., Ding, X., He, S., Cao, W., Wang, Y., Fan, S., Xiao, Y., Zhou, G., & Shen, A. (2016). beta2-adrenergic receptor signaling promotes pancreatic ductal adenocarcinoma (PDAC) progression through facilitating PCBP2-dependent c-myc expression. *Cancer Lett, 373*(1), 67-76.

112. Wang, T., Wei, J. J., Sabatini, D. M., & Lander, E. S. (2014). Genetic screens in human cells using the CRISPR-Cas9 system. *Science, 343*(6166), 80-84.

113. Wang, X., Lu, Z., Gomez, A., Hon, G. C., Yue, Y., Han, D., Fu, Y., Parisien, M., Dai, Q., Jia, G., Ren, B., Pan, T., & He, C. (2014). N6-methyladenosine-dependent regulation of messenger RNA stability. *Nature, 505*(7481), 117-120.

114. Wang, X., Zhao, B. S., Roundtree, I. A., Lu, Z., Han, D., Ma, H., Weng, X., Chen, K., Shi, H., & He, C. (2015). N(6)-methyladenosine Modulates Messenger RNA Translation Efficiency. *Cell, 161*(6), 1388-1399.

115. Wang, Y., Engels, I. H., Knee, D. A., Nasoff, M., Deveraux, Q. L., & Quon, K. C. (2004). Synthetic lethal targeting of MYC by activation of the DR5 death receptor pathway. *Cancer Cell, 5*(5), 501-512.

116. Weng, H., Huang, H., Wu, H., Qin, X., Zhao, B. S., Dong, L., Shi, H., Skibbe, J., Shen, C., Hu, C., Sheng, Y., Wang, Y., Wunderlich, M., Zhang, B., Dore, L. C., Su, R., Deng, X., Ferchen, K., Li, C., Sun, M., Lu, Z., Jiang, X., Marcucci, G., Mulloy, J. C., Yang, J., Qian, Z., Wei, M., He, C., & Chen, J. (2018). METTL14 Inhibits Hematopoietic Stem/Progenitor Differentiation and Promotes Leukemogenesis via mRNA m(6)A Modification. *Cell Stem Cell, 22*(2), 191-205 e199.

117. Wheeler, E. C., Vu, A. Q., Einstein, J. M., DiSalvo, M., Ahmed, N., Van Nostrand, E. L., Shishkin, A. A., Jin, W., Allbritton, N. L., & Yeo, G. W. (2020). Pooled CRISPR screens with imaging on microraft arrays reveals stress granule-regulatory factors. *Nature Methods*.

118. Wiley, S. R., Schooley, K., Smolak, P. J., Din, W. S., Huang, C.-P., Nicholl, J. K., Sutherland, G. R., Smith, T. D., Rauch, C., Smith, C. A., & Goodwin, R. G. (1995). Identification and characterization of a new member of the TNF family that induces apoptosis. *Immunity, 3*(6), 673-682.

119. Wu, P. (2020). Inhibition of RNA-binding proteins with small molecules. *Nature Reviews Chemistry*.

120. Xie, L., Law, B. K., Chytil, A. M., Brown, K. A., Aakre, M. E., & Moses, H. L. (2004). Activation of the Erk pathway is required for TGF-beta1-induced EMT in vitro. *Neoplasia, 6*(5), 603-610.

121. Xu, C., Bailly-Maitre, B., & Reed, J. C. (2005). Endoplasmic reticulum stress: cell life and death decisions. *J Clin Invest, 115*(10), 2656-2664.

122. Xu, H., Xiao, T., Chen, C. H., Li, W., Meyer, C. A., Wu, Q., Wu, D., Cong, L., Zhang, F., Liu, J. S., Brown, M., & Liu, X. S. (2015). Sequence determinants of improved CRISPR sgRNA design. *Genome Res, 25*(8), 1147-1157.

123. Yang, J., Zhang, L., Jiang, Z., Ge, C., Zhao, F., Jiang, J., Tian, H., Chen, T., Xie, H., Cui, Y., Yao, M., Li, H., & Li, J. (2019). TCF12 promotes the tumorigenesis and metastasis of hepatocellular carcinoma via upregulation of CXCR4 expression. *Theranostics, 9*(20), 5810-5827.

124. Yau, E. H., Kummetha, I. R., Lichinchi, G., Tang, R., Zhang, Y., & Rana, T. M. (2017). Genome-Wide CRISPR Screen for Essential Cell Growth Mediators in Mutant KRAS Colorectal Cancers. *Cancer Res, 77*(22), 6330-6339.

125. Yin, S., Cheryan, V. T., Xu, L., Rishi, A. K., & Reddy, K. B. (2017). Myc mediates cancer stem-like cells and EMT changes in triple negative breast cancers cells. *PLoS One, 12*(8), e0183578.

126. Yoshida, H., Matsui, T., Yamamoto, A., Okada, T., & Mori, K. (2001). XBP1 mRNA Is Induced by ATF6 and Spliced by IRE1 in Response to ER Stress to Produce a Highly Active Transcription Factor. *Cell, 107*(7), 881-891.

127. Zaccara, S., & Jaffrey, S. R. (2020). A Unified Model for the Function of YTHDF Proteins in Regulating m(6)A-Modified mRNA. *Cell*.

128. Zhang, Y., Liu, T., Meyer, C. A., Eeckhoute, J., Johnson, D. S., Bernstein, B. E., Nusbaum, C., Myers, R. M., Brown, M., Li, W., & Liu, X. S. (2008). Model-based analysis of ChIP-Seq (MACS). *Genome Biol, 9*(9), R137.

129. Zhang, Z., Theler, D., Kaminska, K. H., Hiller, M., de la Grange, P., Pudimat, R., Rafalska, I., Heinrich, B., Bujnicki, J. M., Allain, F. H., & Stamm, S. (2010). The YTH domain is a novel RNA binding domain. *J Biol Chem, 285*(19), 14701-14710.

130. Zhong, L., Liao, D., Zhang, M., Zeng, C., Li, X., Zhang, R., Ma, H., & Kang, T. (2019). YTHDF2 suppresses cell proliferation and growth via destabilizing the EGFR mRNA in hepatocellular carcinoma. *Cancer Lett, 442*, 252-261.

131. Zhou, J., Wan, J., Gao, X., Zhang, X., Jaffrey, S. R., & Qian, S. B. (2015). Dynamic m(6)A mRNA methylation directs translational control of heat shock response. *Nature, 526*(7574), 591-594.

132. Zhou, Y., Zhou, B., Pache, L., Chang, M., Khodabakhshi, A. H., Tanaseichuk, O., Benner, C., & Chanda, S. K. (2019). Metascape provides a biologist-oriented resource for the analysis of systems-level datasets. *Nat Commun, 10*(1), 1523.

133. Zhu, T., Roundtree, I. A., Wang, P., Wang, X., Wang, L., Sun, C., Tian, Y., Li, J., He, C., & Xu, Y. (2014). Crystal structure of the YTH domain of YTHDF2 reveals mechanism for recognition of N6-methyladenosine. *Cell Res, 24*(12), 1493-1496.

134. Zhu, X., Huang, S., Zeng, L., Ma, J., Sun, S., Zeng, F., Kong, F., & Cheng, X. (2017). HMOX-1 inhibits TGF-beta-induced epithelial-mesenchymal transition in the MCF-7 breast cancer cell line. *Int J Mol Med, 40*(2), 411-417.

135. Zhu, Y., Yan, L., Zhu, W., Song, X., Yang, G., & Wang, S. (2019). MMP2/3 promote the growth and migration of laryngeal squamous cell carcinoma via PI3K/Akt-NF-kappaB-mediated epithelial-mesenchymal transformation. *J Cell Physiol*.

136. Zuber, J., Shi, J., Wang, E., Rappaport, A. R., Herrmann, H., Sison, E. A., Magoon, D., Qi, J., Blatt, K., Wunderlich, M., Taylor, M. J., Johns, C., Chicas, A., Mulloy, J. C., Kogan, S. C., Brown, P., Valent, P., Bradner, J. E., Lowe, S. W., & Vakoc, C. R. (2011). RNAi screen identifies Brd4 as a therapeutic target in acute myeloid leukaemia. *Nature, 478*(7370), 524-528.